

REPORT DOCUMENTATION PAGE			Form Approved OMB No. 0704-0188	
Public reporting burden for this collection of information is estimated to average 1 hour per response, including the time for reviewing instructions, searching existing data sources, gathering and maintaining the data needed, and completing and reviewing the collection of information. Send comments regarding this burden estimate or any other aspect of this collection of information, including suggestions for reducing this burden, to Washington Headquarters Services, Directorate for Information Operations and Reports, 1215 Jefferson Davis Highway, Suite 1204, Arlington, VA 22202-4302, and to the Office of Management and Budget, Paperwork Reduction Project (0704-0188), Washington, DC 20503.				
1. AGENCY USE ONLY (Leave blank)		2. REPORT DATE 29 Jun 98		3. REPORT TYPE AND DATES COVERED
4. TITLE AND SUBTITLE Synchronously Pumped Optical Parametric Oscillator with Intracavity Difference Frequency Mixing			5. FUNDING NUMBERS	
6. AUTHOR(S) Michael Edward Dearborn				
7. PERFORMING ORGANIZATION NAME(S) AND ADDRESS(ES) University of New Mexico			8. PERFORMING ORGANIZATION REPORT NUMBER 98-012D	
9. SPONSORING/MONITORING AGENCY NAME(S) AND ADDRESS(ES) THE DEPARTMENT OF THE AIR FORCE AFIT/CIA, BLDG 125 2950 P STREET WPAFB OH 45433			10. SPONSORING/MONITORING AGENCY REPORT NUMBER	
11. SUPPLEMENTARY NOTES				
12a. DISTRIBUTION AVAILABILITY STATEMENT Unlimited distribution In Accordance With AFI 35-205/AFIT Sup 1			12b. DISTRIBUTION CODE	
13. ABSTRACT (Maximum 200 words)				
<div style="position: absolute; top: 10px; left: 10px; font-size: 2em; font-weight: bold; transform: rotate(-10deg);"> 19980708 011 </div>				
14. SUBJECT TERMS			15. NUMBER OF PAGES 145	
			16. PRICE CODE	
17. SECURITY CLASSIFICATION OF REPORT	18. SECURITY CLASSIFICATION OF THIS PAGE	19. SECURITY CLASSIFICATION OF ABSTRACT	20. LIMITATION OF ABSTRACT	

PII Redacted

**Synchronously Pumped Optical Parametric
Oscillator with Intracavity Difference Frequency
Mixing**

by

Michael Edward Dearborn

Abstract of Dissertation

Submitted in Partial Fulfillment of the
Requirements for the Degree of

**Doctor of Philosophy
Optical Sciences**

**The University of New Mexico
Albuquerque, New Mexico**

Aug 1998

In this work we experimentally investigate a singly resonant optical parametric oscillator (OPO) with an intracavity crystal that mixes the signal and idler waves, enhancing the power conversion efficiency of the idler radiation.

Optical parametric oscillators provide a method for producing coherent tunable radiation from a coherent fixed-frequency pump source. The pump frequency ω_p is converted to the signal and idler frequencies ω_s and ω_i , respectively, in the OPO interaction, $\omega_p = \omega_s + \omega_i$, $\omega_s \geq \omega_i$. Since the signal and idler frequencies sum to the incident pump frequency, they are always lower than the pump frequency.

Extra-cavity difference-frequency mixing (DFM) of the signal and idler from an OPO was demonstrated in some early experiments [1–3] and recently a number of investigators have examined mixing the signal and idler waves generated from a synchronously pumped OPO to produce long-wavelength difference-frequency radiation [4–6]. Here the difference-frequency ω_d is produced in the DFM interaction, $\omega_d = \omega_s - \omega_i$. The DFM process not only produces long-wavelength radiation at the difference frequency, but for each difference-frequency photon produced, another idler photon is produced. Thus, this technique also increases the idler-frequency conversion efficiency. Production of the long-wavelength difference-frequency photons may not be possible in a single-step OPO process, due to transmission bands and phase-matching limitations of available crystals and available pump wavelengths.

Recently the advantages of carrying out a DFM process inside an OPO cavity resonant at the signal frequency were reported. [7] This was called an OPO-DFM device. Using a plane-wave model, it was found that operation at high conversion efficiency occurs over a large dynamic range of incident pump intensity for proper choices of the ratio of the coupling parameters of the OPO and DFM processes. This large dynamic range is expected to improve the conversion efficiency when the pump beam is not a cw plane wave, but has transverse or temporal intensity variations. The pump radiation is converted into signal and idler radiation in the OPO interaction, and signal radiation is converted into idler and difference-frequency radiation in the

DFM interaction. A high-Q cavity is used, since no out-coupling at ω_s is necessary. Except near threshold, most of the signal radiation generated in the OPO process is down-converted by the DFM process. In the ideal case where the OPO process heavily depletes the pump radiation, photon-conversion efficiencies—defined as the number of generated photons per incident pump photon—for generation of idler and difference-frequency radiation can be close to $\eta_i = 2$ and $\eta_d = 1$ respectively.

Experimental work has produced a maximum idler photon-conversion efficiency of 1.15. An idler photon-conversion efficiency over one is not possible for a simple OPO. Furthermore, the idler photon-conversion efficiency of the OPO with intracavity DFM is an 80% increase as compared to the simple OPO without the intracavity DFM interaction. It is demonstrated that the additional idler power comes at the expense of resonated signal radiation and increased pump depletion. The pump depletion increases since some of the resonated signal radiation is outcoupled in the DFM interaction, preventing back-conversion in the OPO interaction. The maximum idler photon-conversion efficiency corresponds to the generation of 6.3 W of idler power for 18.0 W of pump power. This gives an idler power conversion efficiency of 35% which is greater than the theoretical limit of 31% for the simple OPO.

References

- [1] D. Andreou, "16 μm tunable source using parametric processes in nonlinear crystals," *Opt. Commun.*, vol. 1, no. 23, pp. 37-43, 1977.
- [2] P. Kupecek, H. Le Person, and M. Comte, "A multipurpose efficient tunable infrared coherent source with tuning range from 0.8 to 25 μm and peak powers in the range 50-200 kW," *Infrared Phys.*, vol. 19, no. 3/4, pp. 263-271, 1979.
- [3] P. Kupecek, J. M. Weulersse, P. Isnard, M. Alexandre, and M. Clerc, "An optimized device for UF_6 laser isotopic photochemistry using an optical parametric oscillator and a down converter," *J. Opt. (Paris)*, , no. 14, pp. 43-48, 1983.
- [4] J. D. Kafka, M. L. Watts, and J. W. Pieterse, "Subpicosecond infrared pulse generation using a synchronously pumped optical parametric oscillator," in *Conference on Lasers and Electro-Optics, Vol. 8, OSA Technical Digest Series*, Washington, D.C., 1994, p. 237, Optical Society of America.
- [5] J. D. Kafka, M. L. Watts, and J. W. Pieterse, "Infrared pulse generation using a subpicosecond optical oscillator," in *Ultrafast Phenomena, Vol. 7, OSA Technical Digest Series*, Washington, D.C., 1994, pp. 258-260, Optical Society of America.
- [6] A. Lohner, P. Kruck, and W. W. Rühle, "Generation of 200 femtosecond pulses tunable between 2.5 and 5.5 μm ," *Appl. Phys. B*, vol. 59, no. 2, pp. 211-213, 1994.

- [7] K. Koch, G. T. Moore, and E. C. Cheung, "Optical parametric oscillation with intracavity difference-frequency mixing," *J. Opt. Soc. Am. B*, vol. 12, no. 11, pp. 2268–2273, 1995.

**Synchronously Pumped Optical Parametric
Oscillator with Intracavity Difference Frequency
Mixing**

by

Michael Edward Dearborn

Abstract of Dissertation

Submitted in Partial Fulfillment of the
Requirements for the Degree of

Doctor of Philosophy

Optical Sciences

**The University of New Mexico
Albuquerque, New Mexico**

Aug 1998

In this work we experimentally investigate a singly resonant optical parametric oscillator (OPO) with an intracavity crystal that mixes the signal and idler waves, enhancing the power conversion efficiency of the idler radiation.

Optical parametric oscillators provide a method for producing coherent tunable radiation from a coherent fixed-frequency pump source. The pump frequency ω_p is converted to the signal and idler frequencies ω_s and ω_i , respectively, in the OPO interaction, $\omega_p = \omega_s + \omega_i$, $\omega_s \geq \omega_i$. Since the signal and idler frequencies sum to the incident pump frequency, they are always lower than the pump frequency.

Extra-cavity difference-frequency mixing (DFM) of the signal and idler from an OPO was demonstrated in some early experiments [1–3] and recently a number of investigators have examined mixing the signal and idler waves generated from a synchronously pumped OPO to produce long-wavelength difference-frequency radiation [4–6]. Here the difference-frequency ω_d is produced in the DFM interaction, $\omega_d = \omega_s - \omega_i$. The DFM process not only produces long-wavelength radiation at the difference frequency, but for each difference-frequency photon produced, another idler photon is produced. Thus, this technique also increases the idler-frequency conversion efficiency. Production of the long-wavelength difference-frequency photons may not be possible in a single-step OPO process, due to transmission bands and phase-matching limitations of available crystals and available pump wavelengths.

Recently the advantages of carrying out a DFM process inside an OPO cavity resonant at the signal frequency were reported. [7] This was called an OPO-DFM device. Using a plane-wave model, it was found that operation at high conversion efficiency occurs over a large dynamic range of incident pump intensity for proper choices of the ratio of the coupling parameters of the OPO and DFM processes. This large dynamic range is expected to improve the conversion efficiency when the pump beam is not a cw plane wave, but has transverse or temporal intensity variations. The pump radiation is converted into signal and idler radiation in the OPO interaction, and signal radiation is converted into idler and difference-frequency radiation in the

DFM interaction. A high-Q cavity is used, since no out-coupling at ω_s is necessary. Except near threshold, most of the signal radiation generated in the OPO process is down-converted by the DFM process. In the ideal case where the OPO process heavily depletes the pump radiation, photon-conversion efficiencies—defined as the number of generated photons per incident pump photon—for generation of idler and difference-frequency radiation can be close to $\eta_i = 2$ and $\eta_d = 1$ respectively.

Experimental work has produced a maximum idler photon-conversion efficiency of 1.15. An idler photon-conversion efficiency over one is not possible for a simple OPO. Furthermore, the idler photon-conversion efficiency of the OPO with intracavity DFM is an 80% increase as compared to the simple OPO without the intracavity DFM interaction. It is demonstrated that the additional idler power comes at the expense of resonated signal radiation and increased pump depletion. The pump depletion increases since some of the resonated signal radiation is outcoupled in the DFM interaction, preventing back-conversion in the OPO interaction. The maximum idler photon-conversion efficiency corresponds to the generation of 6.3 W of idler power for 18.0 W of pump power. This gives an idler power conversion efficiency of 35% which is greater than the theoretical limit of 31% for the simple OPO.

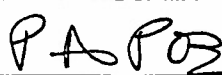

References

- [1] D. Andreou, "16 μm tunable source using parametric processes in nonlinear crystals," *Opt. Commun.*, vol. 1, no. 23, pp. 37-43, 1977.
- [2] P. Kupecek, H. Le Person, and M. Comte, "A multipurpose efficient tunable infrared coherent source with tuning range from 0.8 to 25 μm and peak powers in the range 50-200 kW," *Infrared Phys.*, vol. 19, no. 3/4, pp. 263-271, 1979.
- [3] P. Kupecek, J. M. Weulersse, P. Isnard, M. Alexandre, and M. Clerc, "An optimized device for UF_6 laser isotopic photochemistry using an optical parametric oscillator and a down converter," *J. Opt. (Paris)*, , no. 14, pp. 43-48, 1983.
- [4] J. D. Kafka, M. L. Watts, and J. W. Pieterse, "Subpicosecond infrared pulse generation using a synchronously pumped optical parametric oscillator," in *Conference on Lasers and Electro-Optics, Vol. 8, OSA Technical Digest Series*, Washington, D.C., 1994, p. 237, Optical Society of America.
- [5] J. D. Kafka, M. L. Watts, and J. W. Pieterse, "Infrared pulse generation using a subpicosecond optical oscillator," in *Ultrafast Phenomena, Vol. 7, OSA Technical Digest Series*, Washington, D.C., 1994, pp. 258-260, Optical Society of America.
- [6] A. Lohner, P. Kruck, and W. W. Rühle, "Generation of 200 femtosecond pulses tunable between 2.5 and 5.5 μm ," *Appl. Phys. B*, vol. 59, no. 2, pp. 211-213, 1994.

- [7] K. Koch, G. T. Moore, and E. C. Cheung, "Optical parametric oscillation with intracavity difference-frequency mixing," *J. Opt. Soc. Am. B*, vol. 12, no. 11, pp. 2268–2273, 1995.

REQUEST AND AUTHORIZATION FOR PERMANENT CHANGE OF STATION - MILITARY

(This Form is Subject to the Privacy Act of 1974 - Use Blanket PAS - AF Form 11)

The following individual will proceed on permanent change of station.		PCS Without PCA	X	PCS With PCA	TED <div style="text-align: right;">JUL 98</div>
1. GRADE, NAME <i>(Last, First, Middle Initial)</i> CPT DEARBORN MICHAEL E PII Redacted		3. SDAFSC/CAFSC <div style="text-align: right;">T061S3D</div>			
4. SECURITY CLEARANCE <i>(Include date of last investigation)</i> TOP SEC BI 900522		5. REPORT TO COMDR. NEW ASSIGNMENT NLT 980715		6. TRAVEL DAYS AUTHORIZED IF TRAVELING BY PRIVATELY OWNED CONVEYANCE 001	
7. TDY ENROUTE					
8. UNIT, MAJOR COMMAND, AND ADDRESS OF UNIT TO WHICH ASSIGNED DEAN OF FACULTY (USAF) USAF ACADEMY ACD CO 80840-0000			9. UNIT, MAJOR COMMAND, AND ADDRESS OF UNIT FROM WHICH RELIEVED AF INST OF TECH IN (AFIT) ALBUQUERQUE IT 01 SCH NM 87131-5000		
10. TYPE OF TOUR <i>(Check One)</i>		11. TOUR LENGTH/Total No. of Months		12. EXTENDED LONG TOUR VOL ➔	
<input type="checkbox"/> ACCOMPANIED <input type="checkbox"/> UNACCOMPANIED, DEPENDENTS RESTRICTED					
13. DEPENDENT TRAVEL		14. THIS IS A JOIN-SPOUSE ASSIGNMENT <i>(Include spouse's grade, name and SSN)</i> ➔			
<input type="checkbox"/> A. CONCURRENT TRAVEL IS AUTOMATIC <input type="checkbox"/> B. CONCURRENT TRAVEL IS APPROVED <input type="checkbox"/> C. NONCONCURRENT TRAVEL IS AUTHORIZED IN LESS THAN 20 WEEKS <input type="checkbox"/> D. NONCONCURRENT TRAVEL IS AUTHORIZED IN MORE THAN 20 WEEKS <input type="checkbox"/> E. TRAVEL IS AUTHORIZED TO A DESIGNATED PLACE					
15. AUTHORITY FOR CCTVL		16. HOMEBASING/FOLLOW-ON ASSIGNMENT <i>(Include AAN, GPAS, and RNLT)</i>			
17. DEPENDENT(s): <i>(List names, DOB of Children, relationship to member and current address)</i> KARIN/ SPOUSE / JOSHUA/ SON / [REDACTED] CHANGE/ SON / [REDACTED] PII Redacted			18. DEPARTURE CERTIFICATION: I certify that to the best of my knowledge I will depart PCS at _____(hrs) _____(date) _____ <div style="text-align: right;"><i>(Signature)</i></div>		
19. OVERSEAS TRANSPORTATION DATA					
A. Comply with MTA (DD Form 1482)		C. TDY station will obtain flight reservations. Member is not authorized to depart TDY station before receipt of validated MTA or GTR (SF1169) from the TMO			
B. Member will comply with reporting time and flight reservations in the MTA or as arranged by the TMO per AFI 24-10, and is not authorized to depart this station before receipt of validated MTA or GTR (SF1169) from the TMO.		D. Dependent(s) will comply with reporting data and flight reservations in the MTA.			
20. PCS EXPENSE CHARGEABLE TO 5783500 328 5752.0*875825 CIC: TAC: ATAC: F87B20* NONTEMPORARY STORAGE CHARGEABLE TO: 5783500 328 5758.ON 875825			21. AUTHORITY AND PCS CODE PCS ID: AFI 36-2110, PCS ID C AAN: 0780NB4828		
22. TDY EXPENSE CHARGEABLE TO			23. Excess Baggage Authorized PIECES LBS		
Pursuant to AFR 32-6001, you will report to the base housing referral office servicing your new duty station before entering into any rental, lease, or purchase agreement for off-base housing.					
24. REMARKS <i>(Submit travel voucher within 5 workdays after completion of travel. If TDY en route is authorized, attach receipts showing cost of all lodgings used. All promotional items incurred with PCS/TDY must be turned in to AFO upon arrival at gaining base.)</i> ITEMS 1 AND 2 ON REVERSE APPLY.					
25. DATE 7 MAY 98		26. MPF OFFICIAL <i>(Typed Name, and Grade)</i> P. A. POSEY, MSGT, USAF SUPT, PERSONNEL EMPLOYMT/RELOCATNS		27. SIGNATURE OF MPF OFFICIAL 	
28. DESIGNATION AND LOCATION OF HEADQUARTERS DEPARTMENT OF THE AIR FORCE 377 MISSION SUPPORT SQUADRON (MTC) KIRTLAND AFB, NM 87117-5608		29. SPECIAL ORDER NO. HA-782		30. DATE 7 May 98	
32. DISTRIBUTION A		31. TDN FOR THE COMMANDER			
34. ADDRESS OF GAINING MPF 10 MSS/DPMAE USAF ACADEMY CO 80840-2608		33. SIGNATURE ELEMENT OF ORDERS AUTHENTICATING OFFICIAL  JAIMIE L. PEASE, CAPT, USAF MILITARY PERSONNEL FLIGHT COMMANDER			

ONLY ITEMS INDICATED ON THE REVERSE ARE APPLICABLE

1. Member will contact Outbound Assignments two weeks prior to final departure from base to schedule an outprocessing appointment. Final outprocessing will not be earlier than one duty day prior to departure from base. Members must meet dress and appearance standards if outprocessing out of uniform.

2. Member will report to Accounting and Finance for an initial outprocessing NLT 30 days prior to departure date. Questions concerning Military Pay should be directed to 846-7309 and Travel Pay to 846-7269.

3. (a) Assignment is to a remote station in Alaska. Dependents are not authorized. Two pieces of checked baggage (not to exceed 140 lbs) and one piece of carry-on baggage is authorized enroute to Elmendorf AFB, AK. On arrival at Elmendorf AFB, an additional piece of baggage will be authorized for issuance of military issue gear. Total checked baggage from Elmendorf AFB, AK to remote site will not exceed 210 lbs.

(b) Report to J MSSQ (remote duty processing office), Elmendorf AFB, AK, on TDY enroute, for approximately _____ days for processing and transportation to final destination. POV may not be shipped.

4. Member is authorized POV travel via the Alaska Highway to include the Alaskan Marine Highway System. Authority is AFR 75-8, Vol. II, para 2-10.

5. _____ was requested by Chief Security Police, Kirtland AFB, NM on _____.

6. Authority for item 23, AFI 24-101, Chap 6.

7. Four days proceed time is authorized.

8. (a) Since all TDY per diem payments are based on the availability of government quarters and mess, contact the Billing Office at the TDY station to see if they are available.

(b) All government meals are available and directed.

(c) Partial government meals are available and directed.

(d) Government meals are not available nor directed.

9. This is a joint-spouse assignment and household goods weight allowance is based on the highest ranking member's entitlement per JFTR, Vol. I, para U5315-B.

10. (a) Member has an approved follow-on (FO) assignment and has agreed not to relocate dependents, ship POV, or move, or store household goods (HHCs) at government expense. Member may relocate dependents, ship POV, or move, or store HHCs to a location other than FO location at their own expense.

(b) Member has an approved homebased (HB) assignment and has agreed not to relocate dependents, ship POV, or move, or store HHCs at government expense. Member may relocate dependents, ship POV, or move, or store HHCs to a location other than HB location at their own expense.

(c) Single members, single parents, and military couples who will serve concurrent, unaccompanied short tours are authorized to store HHCs by the most cost effective means as determined by the local TMO. Members may relocate their dependents to a designated location at their own expense and retain FO or HB assignment. A waiver is not required.

(d) Members may ship their POV to the overseas location at government expense, if authorized for the particular location and their grade, and retain their FO or HB assignment.

11. Member is authorized up to 8 days PTDY as indicated on the reverse, for househunting purposes in conjunction with PCS. Authority AFI 36-3003.

12. Member is authorized full JFTR. Authorization is AFR 75-25, Atch 2, Tbl 2 and current CBPOL Add'l Wt Allowance for Personnel Being Assigned to Administrative Wt Restricted Areas.

13. "In accordance with para 3(a) of Article XVII of the Agreement of Implementation of Article IV of the Panama Canal Treaty of 1977, the above named individual(s), members of the Force, is exempt from Customs Inspections upon entering or departing from the Republic of Panama when traveling on official orders."

"De conformidad con el Párrafo 3(a) del Artículo XVII del Acuerdo para la Ejecución del Artículo IV del tratado del Canal de Panamá de 1977, el individuo(s) cuyo nombre(s) aparece arriba miembro(s) de las Fuerzas, esta exento de la inspección de aduana al entrar o salir de la Republica de Panama cuando viaje bajo ordenes oficiales."

14. IAW AFI 36-2102, Atch 4, para 2A.25, report to the gaining local OSI to receive the Personal Protection Briefing on Anti-Terrorism.

15. (a) The identified member(s) (has)(have been) initially screened and meet(s) the reliability criteria as stated in AFI 36-2104 to perform nuclear weapons associated duties or other designated high-risk duties.

(b) Member meets the reliability criteria as stated in AFI 36-2104 to perform nuclear weapons associated duties or other designated high-risk duties.

DEPARTMENT OF THE AIR FORCE
377TH MISSION SUPPORT SQUADRON (AFMC)
KIRTLAND AFB, NEW MEXICO 87117-3688

NATO TRAVEL ORDER
ORDRE DE MISSION OTAN

Country of origin: THE UNITED STATES OF AMERICA
Pays de Provenance: LES ETATS UNIS

Order Number
Numero de serie: ITEM 29

1. The bearer
Le Porteur: ITEMS 1 & 2
(Grade, Name, SSN)

and group as shown hereon or on attached list
et personnel porte ci-dessous sur la liste jointe

2. will travel from
fera mouvement de ITEM 9 to ITEM 8

via
via DIRECT FLIGHT

Date of departure (on or about)
Date du depart (ou vers la) N/A

Expected date of return
Date probable du retour N/A

3. Authority is not granted to possess and carry arms.
Autorisation de port d'armes (non accordee).

4. The person listed in paragraph 1 is authorized to carry
La personne indique au paragraphe 1 est autorisee a porte

sealed dispatches, containing only official documents, numbered
plus scelles, ne contenant que des documents officiels, numerotes

5. I hereby certify that this individual/group "is/are" member(s) of a Force as defined in the NATO Status of Forces Agreement and that this is an authorized move under the term of this agreement.

Je soussigne certifie que la personnel vise appartient a une armee telle que definie dans l'Accord OTAN sur le statut des Forces armees et que ce deplacement est officiel selon les termes de cet Accord.

6. This travel order is to be provided to civil and military authorities on request.

Cet ordre de mission devra etre presente sur demande des autorites civiles et militaires.

FOR THE COMMANDER
(OFFICER AUTHORIZING MOVEMENT)
(OFFICIER AUTORISANT LE MOUVEMENT)

Date of issue
Date de l'autorisation: ITEM 30

*Delete items not applicable/Rayer la mention inutile.

Michael Edward Dearborn

Candidate

Physics & Astronomy

Department

This dissertation is approved, and it is acceptable in quality and form for publication on microfilm:

Approved by the Dissertation Committee:

, Chairperson

Karl W. Kael

Gerald T. Moore

Vaclav Kubeck

Accepted:

Robin Metzger

Dean, Graduate School

6/12/98

Date

**Synchronously Pumped Optical Parametric
Oscillator with Intracavity Difference Frequency
Mixing**

by

Michael Edward Dearborn

B.S., Physics, United States Air Force Academy, 1988

M.A., Physics, University of Texas, 1989

Dissertation

Submitted in Partial Fulfillment of the
Requirements for the Degree of

**Doctor of Philosophy
Optical Sciences**

**The University of New Mexico
Albuquerque, New Mexico**

Aug 1998

©1998, Michael Edward Dearborn

To my wife Karin
and my children Josh and Chance

Acknowledgments

Completion of the Ph.D. has been a dream of mine for many years. I could not have achieved this goal without the help and support of so many people. Above all, I thank my wife Karin and children, Josh and Chance. Special thanks goes to Jean-Claude for serving as my committee chairman and providing me with the opportunity to interface with the Air Force Research Laboratory where I performed my research. Thanks also goes to Karl and Gerry for their role as mentors while I performed my work at the Air Force Research Laboratory. My daily conversations with them and the advice they provided me with has been invaluable. My summers in the lab were productive and fun in part thanks to Graham Allan. Thanks to Don with whom I had many stimulating conversations in fields other than optics, to my good friend Jerry, and to Roger, who provided me with general administrative support which helped immeasurably. Last but not least, I owe many thanks to my good friends and fellow graduate students Doug Nelson, Tom Alley and Matt Bohn.

MICHAEL EDWARD DEARBORN

The University of New Mexico

Aug 1998

**Synchronously Pumped Optical Parametric
Oscillator with Intracavity Difference Frequency
Mixing**

by

Michael Edward Dearborn

Abstract of Dissertation

Submitted in Partial Fulfillment of the
Requirements for the Degree of

Doctor of Philosophy

Optical Sciences

**The University of New Mexico
Albuquerque, New Mexico**

Aug 1998

Synchronously Pumped Optical Parametric Oscillator with Intracavity Difference Frequency Mixing

by

Michael Edward Dearborn

B.S., Physics, United States Air Force Academy, 1988

M.A., Physics, University of Texas, 1989

Ph.D., Optical Sciences, University of New Mexico, 1998

Abstract

In this work we experimentally investigate a singly resonant optical parametric oscillator (OPO) with an intracavity crystal that mixes the signal and idler waves, enhancing the power conversion efficiency of the idler radiation.

Optical parametric oscillators provide a method for producing coherent tunable radiation from a coherent fixed-frequency pump source. The pump frequency ω_p is converted to the signal and idler frequencies ω_s and ω_i , respectively, in the OPO interaction, $\omega_p = \omega_s + \omega_i$, $\omega_s \geq \omega_i$. Since the signal and idler frequencies sum to the incident pump frequency, they are always lower than the pump frequency.

Extra-cavity difference-frequency mixing (DFM) of the signal and idler from an OPO was demonstrated in some early experiments [1–3] and recently a number of investigators have examined mixing the signal and idler waves generated from a synchronously pumped OPO to produce long-wavelength difference-frequency radiation [4–6]. Here the difference-frequency ω_d is produced in the DFM interaction, $\omega_d = \omega_s - \omega_i$. The DFM process not only produces long-wavelength radiation at the difference frequency, but for each difference-frequency photon produced, another

idler photon is produced. Thus, this technique also increases the idler-frequency conversion efficiency. Production of the long-wavelength difference-frequency photons may not be possible in a single-step OPO process, due to transmission bands and phase-matching limitations of available crystals and available pump wavelengths.

Recently the advantages of carrying out a DFM process inside an OPO cavity resonant at the signal frequency were reported. [7] This was called an OPO-DFM device. Using a plane-wave model, it was found that operation at high conversion efficiency occurs over a large dynamic range of incident pump intensity for proper choices of the ratio of the coupling parameters of the OPO and DFM processes. This large dynamic range is expected to improve the conversion efficiency when the pump beam is not a cw plane wave, but has transverse or temporal intensity variations. The pump radiation is converted into signal and idler radiation in the OPO interaction, and signal radiation is converted into idler and difference-frequency radiation in the DFM interaction. A high-Q cavity is used, since no out-coupling at ω_s is necessary. Except near threshold, most of the signal radiation generated in the OPO process is down-converted by the DFM process. In the ideal case where the OPO process heavily depletes the pump radiation, photon-conversion efficiencies—defined as the number of generated photons per incident pump photon—for generation of idler and difference-frequency radiation can be close to $\eta_i = 2$ and $\eta_d = 1$ respectively.

Experimental work has produced a maximum idler photon-conversion efficiency of 1.15. An idler photon-conversion efficiency over one is not possible for a simple OPO. Furthermore, the idler photon-conversion efficiency of the OPO with intracavity DFM is an 80% increase as compared to the simple OPO without the intracavity DFM interaction. It is demonstrated that the additional idler power comes at the expense of resonated signal radiation and increased pump depletion. The pump depletion increases since some of the resonated signal radiation is outcoupled in the DFM interaction, preventing back-conversion in the OPO interaction. The maximum idler photon-conversion efficiency corresponds to the generation of 6.3 W of idler power for

18.0 W of pump power. This gives an idler power conversion efficiency of 35% which is greater than the theoretical limit of 31% for the simple OPO.

Contents

List of Tables	xiii
List of Figures	xiv
1 Introduction	1
1.1 Introduction	1
1.2 Tunable mid-infrared sources & the OPO-DFM device	2
1.3 Periodically poled lithium niobate and quasi-phasematching	5
1.4 Historical development	8
1.5 Report organization	11
2 Quasi-phasematching & periodically poled LiNbO₃	13
2.1 Introduction	13
2.1.1 Periodically poled lithium niobate	15
2.1.2 Production of periodically poled lithium niobate	19
2.1.3 Photorefractive effect	21
2.2 Quasi-phasematching theory	24
2.2.1 Analytical approach	25
2.2.2 Tuning characteristics of quasi-phasematched devices	29
2.2.3 Bandwidth characteristics of quasi-phasematched devices	32
2.3 Photorefractive effect in material with periodic $\chi^{(2)}$ structure	38
2.3.1 Alternative QPM materials	44

3	Synchronously pumped optical parametric oscillator using periodically poled LiNbO₃	45
3.1	Introduction	45
3.2	Coupled wave equations	46
3.2.1	Nonlinear polarization	46
3.2.2	Derivation of coupled-wave equations	48
3.2.3	OPO solutions to simplified coupled-wave equations	50
3.2.4	Self consistent OPO solutions to complete coupled plane Wave Equations	53
3.3	Amplitude fluctuations of singly and doubly resonant OPO's	56
3.4	OPO cavity design and OPO characterization	58
3.5	Experimental description	63
3.6	Computational and experimental results	68
3.6.1	Cavity detuning and lethargy	68
3.6.2	Temperature effects	73
3.6.3	Output coupling studies	75
3.6.4	Temporal and spatial studies	78
4	Optical parametric oscillator with intracavity difference-frequency mixing	89
4.1	Introduction	89
4.2	Theory and modeling	91
4.2.1	OPO-DFM modeling for simplified coupled wave equations .	91
4.2.2	OPO-DFM modeling of complete coupled wave equations .	97
4.3	Experimental design	99
4.4	Experimental setup	107
4.5	Results	109
4.5.1	General OPO-DFM characterization	109
4.5.2	Power studies	112

4.5.3	Temperature tuning and phasematching considerations . . .	117
5	Conclusion and future work	122
5.1	Conclusion	122
5.2	OPO-DFM modifications	123
5.3	Future work	125
	 Appendix	 127
	A Self-consistent OPO-DFM model	128
	 References	 130

List of Tables

1.1	Historical milestones leading to development of OPO-DFM device .	11
2.1	Type I and Type II phasematching.	14
2.2	Acceptance bandwidths for 13 mm PPLN OPO	38
3.1	Condensed notation for nonlinear coefficient	47
3.2	Waist sizes of interacting beams for various focusing parameters. . .	60
3.3	Walk-off times and GVD constants for OPO.	61
3.4	Parameter values used in generating theoretical detuning curves. . .	72
4.1	Acceptance bandwidths for OPO and DFM interactions.	105

List of Figures

1.1	Schematic diagrams of singly and doubly resonant optical parametric oscillators.	3
1.2	Schematic diagram of an OPO-DFM device	5
1.3	Second harmonic output vs. distance for a quasi-phasematched non-linear process	7
2.1	Room temperature grating contour diagram for lithium niobate . . .	16
2.2	Orientations of lithium niobate with respect to crystallographic axes (a, b, c).	18
2.3	Theoretical temperature tuning plots for $29.75 \mu\text{m}$ PPLN crystal. . .	19
2.4	Schematic diagram of PPLN production process	20
2.5	Effect of photorefractive damage on OPO output as function of time.	23
2.6	Second harmonic power as function of propagation distance.	26
2.7	Wave vector diagrams for three wave mixing interaction.	30
2.8	Angle tuning plots of signal and idler.	31
2.9	Wave vector diagram for QPM angle acceptance bandwidth analysis.	36
2.10	Space charges in a) unpoled and b) poled lithium niobate. c) 3-d schematic view of a poled crystal.	40
2.11	Theoretical refractive index changes due to photorefractive effect in lithium niobate for homogeneous a crystal.	43

3.1	Plane-wave theoretical results for transmitted pump power and pump depletion and signal power as a function of incident pump power. . .	52
3.2	Amplitude stability of an OPO due to doubly resonant effects. . . .	56
3.3	Signal wavelength versus noncollinear angle.	63
3.4	Schematic of experimental set-up for OPO.	64
3.5	Signal output of the chopped OPO.	66
3.6	Inferred power signal efficiency as function of cavity detuning. . . .	69
3.7	Transmitted pump power as a function of cavity detuning.	70
3.8	Theoretical curve of pump and signal power as a function of cavity detuning.	73
3.9	Transmitted pump and signal power as a function of incident pump power for on synchronism.	74
3.10	OPO signal wavelength as a function of crystal temperature.	75
3.11	Convective effects on operation of OPO.	76
3.12	Signal power as a function of outcoupling loss.	77
3.13	Spatially resolved peak transmitted pump power as a function of cavity detuning.	79
3.14	Spatially and temporally resolved peak transmitted pump power as a function of incident pump power.	80
3.15	Imaging plane magnification.	81
3.16	Transmitted pump contour plots for various incident pump powers. .	83
3.17	Experimental temporal characterization of pump and signal pulses in OPO during turn-on.	86
3.18	Experimental transmitted pump and signal pulse temporal profiles for several cavity detunings.	87
3.19	Theoretical transmitted pump and signal pulse temporal profiles for several cavity detunings.	88
4.1	Plane wave numerical results of OPO-DFM device.	93

4.2	Complete pump depletion states for OPO-DFM device.	95
4.3	Plane wave numerical results for OPO and OPO-DFM devices. . . .	95
4.4	Idler and difference-frequency photon-conversion efficiencies for an OPO-DFM device.	97
4.5	Theoretical results for transmitted pump power and pump depletion for OPO and OPO-DFM.	99
4.6	Theoretical temporal profiles of transmitted pump for OPO and OPO- DFM devices.	100
4.7	Room temperature grating contour diagram for OPO and DFM in- teractions for an OPO-DFM device.	102
4.8	DFM room temperature grating contours.	104
4.9	Signal wavelength versus noncollinear angle for OPO and DFM inter- actions.	106
4.10	Schematic diagram of OPO-DFM experimental setup.	107
4.11	Transmitted pump power versus cavity detuning for OPO and OPO- DFM.	110
4.12	Experimental cavity detuning results for the simple OPO and OPO- DFM devices.	111
4.13	Experimental results for OPO and OPO-DFM devices.	112
4.14	Experimental results for OPO and OPO-DFM devices.	113
4.15	Percent pump depletion and idler power as a function of incident pump power for the simple OPO and OPO-DFM devices.	114
4.16	Idler and difference-frequency photon conversion efficiencies.	116
4.17	Signal, idler and difference wavelengths versus OPO crystal temper- ature.	118
4.18	Difference-frequency and idler power versus DFM crystal temperature.	119
4.19	OPO-DFM device grating contour diagram.	120
4.20	Experimental DFM grating contour plots.	121

5.1	Fan-out grating OPO-DFM QPM crystal.	124
5.2	Simultaneous OPO-DFM phasematching points.	126

Chapter 1

Introduction

1.1 Introduction

In this work we experimentally and theoretically investigate a singly resonant optical parametric oscillator (OPO) with an intracavity crystal that mixes the signal and idler waves, enhancing the power conversion efficiency of the idler.

Optical parametric oscillators provide a method for producing coherent tunable radiation from a coherent fixed-frequency pump source. The pump frequency ω_p is converted to the signal and idler frequencies ω_s and ω_i , respectively, in the OPO interaction, $\omega_p = \omega_s + \omega_i$, $\omega_s \geq \omega_i$. Since the signal and idler frequencies sum to the incident pump frequency, they are always lower than the pump frequency.

Extra-cavity difference-frequency mixing (DFM) of the signal and idler from an OPO was demonstrated in some early experiments [1–3] and recently a number of investigators [4–6] have examined mixing the signal and idler waves generated from a synchronously pumped OPO to produce long-wavelength difference-frequency radiation. Here the difference frequency ω_d is produced in the DFM interaction, $\omega_d = \omega_s - \omega_i$. The DFM process not only produces long-wavelength radiation at the difference frequency, but for each difference-frequency photon produced, another idler photon is produced. Thus, this technique also increases the idler-frequency conversion

efficiency. Production of the long-wavelength difference-frequency photons may not be possible in a single-step OPO process, due to transmission bands and phase-matching limitations of available crystals and available pump wavelengths.

The advantages of carrying out a DFM process inside the OPO cavity have recently been reported [7]. Using a plane-wave model, it was found that operation of the OPO-DFM device can occur at high conversion efficiency for proper choice of the ratio of the coupling parameters of the OPO (nonlinear gain) and DFM (nonlinear loss) processes. In fact, plane-wave theory shows that complete pump depletion states are possible over a large dynamic range of incident pump intensities. In effect the combined nonlinear loss and gain balance in such a way that the pump is completely depleted in the OPO crystal and no back-conversion from signal to pump takes place. Experimental results do indeed demonstrate that a singly resonant OPO cavity with an intracavity crystal that mixes the signal and idler waves does enhance the power conversion efficiency of the idler radiation.

1.2 Tunable mid-infrared sources & the OPO-DFM device

There is a need in many scientific, environmental, and military applications for efficient sources of tunable mid-infrared radiation. Source requirements for scientific applications sometimes call for short pulse lengths. For example, laser spectroscopy of the vibrational energy relaxation rates in molecules in the condensed phase or semiconductor relaxation rates require femtosecond (fsec) pulses [8, 9]. Small-scale environmental systems such as chemical sensing and combustion diagnostics require low power devices (less than a watt) that are tunable over a wide spectral range [10–12]. Remote optical-sensing techniques such as lidar require sources that operate at ~ 20 Hz, have pulsewidths from 0.01–10 μs and pulse energies from 0.01–1.0 J depending on the specific application [13]. Military applications such as electro-optic counter

measures require high average power devices in the range of 10-100 W [14,15]. Always, there is the desire to make commercial devices smaller, cheaper, simpler and more efficient.

One way in which source needs are currently being met is with nonlinear frequency conversion devices. Optical parametric oscillators and amplifiers (OPOs and OPAs) [16] and difference-frequency mixing (DFM), [17] as well as combinations of nonlinear processes [6,18] have been explored. Also see the November 95 issue of *Journal of Optical Society of America B* which covers OPO devices. Experiments have produced output from continuous wave (cw) radiation [16] to femtosecond duration pulses [18–20]. Of particular interest here is the OPO. As mentioned earlier, an OPO

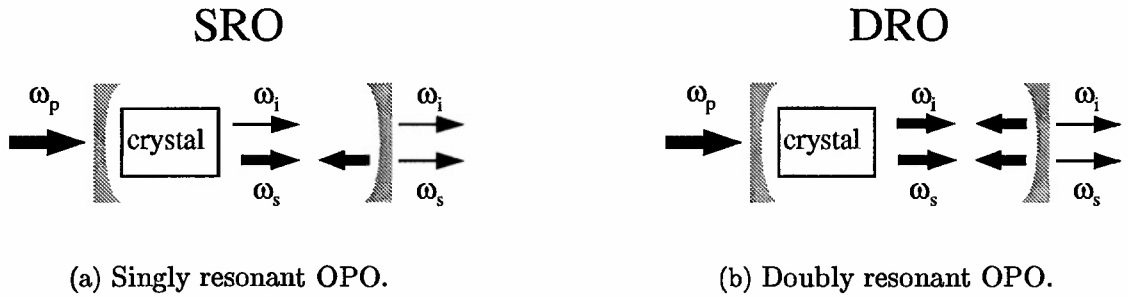


Figure 1.1: Schematic diagrams of singly and doubly resonant optical parametric oscillators.

is a tunable device that converts pump laser radiation into two new, longer wavelengths called the idler and signal. An OPO resonating only one wavelength, usually the signal, is called a singly resonant OPO (SRO). If both the idler and signal are resonated it is called a doubly resonant OPO (DRO). OPOs can be continuous-wave (cw), synchronously pumped, or pulsed (pumped by Q-switched laser). Schematic diagrams of singly and doubly resonant OPO's are shown in Fig. 1.1.

The main advantage of a DRO is that the threshold pump irradiance needed for oscillation can be much lower than that of a SRO. Simple theoretical analysis indicates [21], and experimental results confirm [22], that a DRO's can have thresh-

olds hundreds of times less than a SRO. Thus, it is not surprising that the first OPO was doubly resonant [23]. The main disadvantage of the DRO is that it experiences amplitude and spectral instabilities. Instabilities are due to the fact that the cavity, in general, cannot be simultaneously resonant for both the idler and signal radiation. The frequencies ω_s and ω_i at which the resonator operates are not resonant frequencies and the resonator's Q decreases (greater losses). On the other hand, the signal and idler frequencies are dictated by a phasematching condition (Eq. (2.2) or Eq. (2.5)) which has some characteristic bandwidth. The resonant condition and the phasematching condition compete in such a way as to determine the operating point. This operating point is unstable since small shifts in the frequency of the pump laser and/or changes in the length of the cavity determine a different set of cavity modes for which the gain is optimum. These small shifts result in a mode hop [24]. A mode hop is a sudden change in the spectral output of the device. Also, since the Q of the cavity also changes with a mode hop, we can expect the amplitude of the DRO to fluctuate as well. Finally, with three waves incident on the nonlinear crystal, the three-wave mixing process will be sensitive to the phases of the incoming waves, which depend on cavity length. This also affects the amplitude stability of a DRO. This instability is not present in a SRO since the idler builds up from parametric noise. The devices reported on here are singly resonant. Thus, as a benchmark, it is useful to note the best power conversion efficiency for a SRO. Recently a cw SRO converted 93% of the incident pump into the signal and idler beams [16]. This corresponded to a 25% power conversion efficiency for the idler radiation.

In this work we report experimental results showing that the idler efficiency of an OPO can be increased by about a factor of 1.8 by placing a DFM crystal within the OPO cavity. The increase in efficiency due to the addition of the DFM in the cavity can be described as follows: for an OPO, the best photon-conversion efficiency possible for the idler is $\eta_i = 1$. In other words, for every pump laser photon, one new photon at the idler wavelength is generated. Actual useful efficiencies will

be reduced by losses in the system and incomplete pump conversion. One way to

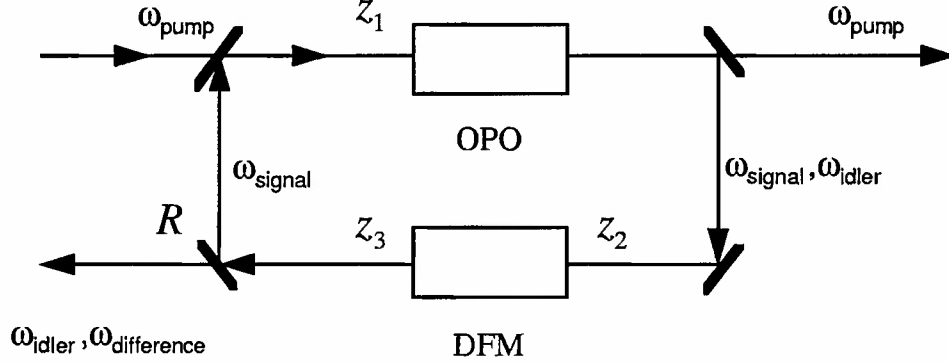


Figure 1.2: Schematic diagram of an OPO-DFM device. The idler and difference-frequency radiation are outcoupled after the intracavity DFM crystal.

increase the photon-conversion efficiency is to place a second nonlinear crystal in the OPO cavity. In this crystal the signal and idler are difference-frequency mixed. For each signal photon another idler photon could possibly be created. Thus, for every pump photon used, now up to two idler photons can be generated. Although the increase in idler photons can also be produced with extra-cavity difference-frequency mixing as well, there are several advantages to placing the DFM crystal intracavity. These advantages were discussed in Section 1.1 In summary, the OPO with intracavity DFM, or OPO-DFM device, has a theoretical efficiency limit which is twice that of the OPO. Figure 1.2 is a schematic diagram of an OPO-DFM device.

1.3 Periodically poled lithium niobate and quasi-phasematching

Efficient generation of radiation with the required wavelengths depends on the availability of crystals with the right material properties. Nonlinear crystals commonly

used to produce mid-infrared radiation include LiIO_3 [25,26], LiNbO_3 [8], KTiOPO_4 [17] and AgGaS_2 [18,27]. In general, the wavelengths generated in a nonlinear conversion process are set by the requirements of phasematching (conservation of momentum) and energy conservation. In addition, there are the requirements that the crystal be transparent at all wavelengths taking part in the conversion process and that the crystal have a high laser damage threshold. In general it is not possible to phase-match for any set of given wavelengths obeying energy conservation. Phasematching ability depends upon the properties of the crystal being used, and hence is dictated by nature.

Quasi-phasematching allows one to obtain efficient conversion for any set of wavelengths obeying energy conservation (as long as each wavelength is in the transmission range of the crystal). This is done by engineering the crystal with a given period of polarization sign-changes so that the phase mismatch is readjusted periodically. A schematic indicating the periodic nature in the crystal is shown in Fig. 1.3. Also shown is the second harmonic output, plotted as a function of propagation distance in units of coherence length for non-phasematched, phasematched, and quasi-phasematched interactions, all other parameters being equal. A coherence length, l_c , is the distance the waves need to travel before they are π radians out of phase. After a coherence length in the non-phasematched case, energy flows from the second harmonic back into the pump. Note that in general, all other parameters being equal, quasi-phasematching is not as efficient as birefringent phasematching (see Sec. 2.2.1).

There has been an explosion of nonlinear devices using QPM techniques. An excellent review is given by Byer [28]. Probably the most successfully and most often used material in quasi-phasematching devices is lithium niobate [29]. One way in which the lithium niobate crystal period is produced is by spontaneously reversing the polarization through electric poling and microlithography techniques. For this reason the material is called periodically poled lithium niobate or PPLN (pronounced

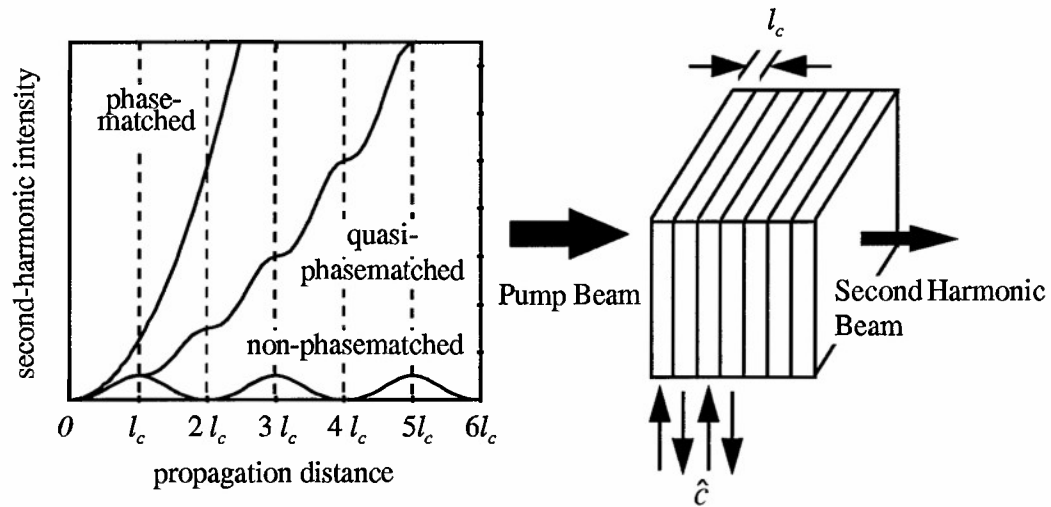


Figure 1.3: Second harmonic output vs. distance for a quasi-phased-matched nonlinear process.

pip-lynn) for short. With PPLN, infrared wavelengths can be efficiently generated as far as the cut-off wavelength of about five microns. Because PPLN can be engineered by employing microlithography techniques to produce tailored grating structures, it is possible to phase-match such that all waves in the nonlinear process travel as extraordinary waves. With this type of interaction the largest nonlinear coefficient of lithium niobate is accessed and the waves experience no spatial walk-off. The largest nonlinear coefficient cannot be used when employing the birefringent phase-matching technique. Thus, although there is a reduction in efficiency when quasi-phase-matching is compared to birefringent phase-matching (see Fig. 1.3), the increased nonlinear coefficient in the quasi-phase-matching process more than makes up for this. The effective nonlinear gain for a quasi-phased-matched process is a factor of 20 greater than a birefringent phase-matched process for lithium niobate. Also, since all waves in the quasi-phased-matched process are extraordinary, there is no spatial walk-off. This makes it a very attractive alternative to conventional birefringent phase-matching

techniques. PPLN has been used successfully in a variety of nonlinear frequency conversion devices [30–32].

The operation of an OPO-DFM system is a logical step in the development of solid-state tunable devices. The predicted improved efficiency of the OPO-DFM device over the OPO promises simpler and smaller systems over those currently in use. This device, coupled with the technology of PPLN crystals and quasi-phasematching, can be the basis for a highly efficient, widely tunable optical source for many applications. Thus, we plan to demonstrate and characterize a synchronously pumped SRO with intracavity DFM of the generated idler and signal radiation.

1.4 Historical development

Here we quickly review the main theoretical and experimental milestones reached which in the development of the OPO-DFM concept. The theory of three-wave mixing, including OPO operation, was presented in a paper by Armstrong *et al.* in 1962 [33]. The authors of this paper were the first to analytically solve the coupled wave-equations and introduced concepts such as phasematching, quasi-phasematching, and a formalism for the induced nonlinear electric dipole and higher moments in an atomic polarization system. The first tunable OPO was demonstrated in 1965 by Giordmaine and Miller [23]. They observed idler and signal radiation at $1.058\text{ }\mu\text{m}$ using $0.529\text{ }\mu\text{m}$ pump light from a Q-switched laser. This proved that the operation of a cavity with a nonlinear crystal as a gain element was practical with high enough pump intensities.

In 1970 Smith [34] presented the theory of placing a second-harmonic crystal inside a laser cavity. This concept is similar to the OPO-DFM concept in that a nonlinear loss mechanism was introduced into an oscillator.

Then in 1971 Campillo and Tang were the first to mention the concept of having two three-wave mixing processes, representing nonlinear gain and loss, within the same optical cavity [35]. Then in 1972 Campillo reported experimental results for

a Q-switched DRO with intracavity sum-frequency generation SFG [36]. He found that the power conversion efficiency for the sum frequency of the pump and signal was 4%, which compared to 1% when the pump and signal were mixed external to the cavity. Bey and Tang introduced a plane-wave theory for the cw, singly resonant, coupled parametric oscillator-upconverter in 1972 [37]. They took into account the SFG interaction for the OPO by changing the transmission of the signal from T_m to $T = T_m + T_+ - T_m T_+$ and plugging this into the full plane wave solutions of the OPO. T_m is the outcoupling mirror transmittance and T_+ is an effective transmittance due to the SFG interaction which is determined by self-consistently solving for the SFG conversion efficiency.

In 1993 Ellingson and Tang published results on a synchronously pumped SRO with intracavity SHG [38]. They produced 115 mW of SHG for 2.1 W of pump power. The SHG pulse length was less than 115 fsec. The OPO was pumped by a Ti:sapphire laser with 100 fsec pulses at 81 MHz. Also in 1993, in two separate papers, Moore and Koch [39, 40] extended Bey and Tang's work on the plane wave theory of SROs with intracavity SFG. They found for the correct material and cavity parameters, that the device was efficient over a large dynamic range of pump intensities. They solved the plane-wave equations, neglecting group velocity mismatch (GVM) and group velocity dispersion (GVD) terms (see Section 3.2.2 for more detail), for the OPO and SFG interactions within the cavity in terms of Jacobi-elliptic functions. After identifying complete pump depletion states, they iterated solutions of the plane wave equations for these states until a steady state was achieved. Since this is a plane-wave theory and neglects GVM and GVD terms, the solutions it provides does not account for effects of diffraction, spatial walk-off, temporal walk-off and pulse broadening. For short pulses more realistic solutions of the coupled wave equations can be found including GVM and GVD effects as well as using Gaussian spatial profiles for the interacting beams. The plane-wave theory of a synchronously pumped OPO which included GVM and GVD effects was published in 1990 by Cheung and Liu [41]. This

theory was then modified in 1991 to include the spatial effects when the interacting beams are Gaussian [42].

To date, no theoretical published work has been presented on OPO-DFM devices that provide pulsed solutions. In Chapter 4 and the appendix we present a simple modification to the analysis in Cheung's paper [41] to include a second non-linear interaction. We specifically present computational results. We also note that cavity detuning effects can be simulated in the plane wave theory by adjusting the pump intensity in accordance with the temporal pump profile. Here the spontaneous parametric generation of the signal was used as a fitting parameter.

Then in 1994 Cheung, Koch and Moore successfully operated and characterized a synchronously pumped OPO-SFG device using AgGaS₂ for the OPO and KTP for the SFG process [43]. The OPO-SFG device was pumped by a 76 MHz, 20 W Nd:YAG laser producing 100 psec pulses. Extracavity and intracavity SFG power efficiencies at around 0.589 μm were about 3.5% and 10.5% respectively.

In 1995 Moore, Koch and Cheung presented the theory of synchronously pumped singly resonant OPO-SHG [44]. Later in 1995 they published their OPO-DFM theory [7]. In both papers they followed the procedure as in their earlier work, determining complete pump depletion states and iterating the plane wave solutions for these states. For the OPO-DFM they found idler quantum efficiencies approaching two and difference frequency quantum efficiencies approaching one for a large dynamic range of incident pump intensity. A summary of the milestones leading to operation of the OPO-DFM is shown in Table 1.1.

Analysis of the OPO-DFM device, promising increased idler efficiency, in addition to the successful operation an OPO-SFG device, has encouraged us to construct, operate, and characterize a synchronously pumped OPO-DFM device. We have chosen to use PPLN for the OPO and DFM crystals. PPLN is used since it has a high nonlinear coefficient ($d_{eff} \sim 2$ times greater than AgGaS₂) and can be engineered with the correct period to phasematch for any wavelength (with the caveat that all

Month & Year	Milestone	Ref.
May 1962	Three-wave mixing equations solved analytically. Birefringent and quasi-phasematching techniques introduced.	[33]
Jun 1965	First tunable OPO experimentally realized. It was doubly resonant.	[23]
Jul 1971	The idea of having a second crystal inside of an OPO providing nonlinear loss was introduced.	[35]
Dec 1972	First operation of OPO-SFG. It was doubly resonant.	[36]
Aug 1993	Full plane-wave theory of OPO-SFG device published.	[39] [40]
Dec 1994	First singly resonant OPO-SFG device operated.	[43]
Jan 1995	Plane wave theory of OPO-SHG device. The device was singly resonant and pulsed.	[44]
Nov 1995	Plane-wave theory of OPO-DFM device published.	[7]
May 1998	Experimental demonstration of OPO-DFM device.	[45]

Table 1.1: Historical milestones leading to development of OPO-DFM device.

interacting wavelengths must be in the transparency range of lithium niobate). As mentioned earlier, PPLN can be phasematched such that there is no Poynting vector walk-off between the waves, since all waves interacting in the process are extraordinary and propagate perpendicularly to the crystal axis. The OPO-DFM device studied here generates radiation around $3.5 \mu\text{m}$ for the idler, $1.5 \mu\text{m}$ for the signal, and $2.7 \mu\text{m}$ for the difference frequency at room temperature.

1.5 Report organization

The rest of this dissertation is organized as follows. Chapter 2 reviews quasi-phasematching theory in detail. Chapter 3 presents theoretical and experimental results on a synchronously pumped PPLN SRO. The experimental set-up of this OPO provides the

basis of the OPO-DFM work that was done. Chapter 4 presents theoretical and experimental results of the OPO-DFM. Conclusions about this work and suggestions for future areas of research are given in Chapter 5.

Chapter 2

Quasi-phasematching & periodically poled LiNbO₃

2.1 Introduction

In a three-wave mixing process, efficient conversion occurs when there is energy conservation and phasematching (momentum conservation). Mathematically these requirements (for a collinear interaction between the beams) are given by,

$$\frac{1}{\lambda_3} = \frac{1}{\lambda_2} + \frac{1}{\lambda_1}, \quad (2.1)$$

$$\frac{n_3}{\lambda_3} = \frac{n_2}{\lambda_2} + \frac{n_1}{\lambda_1}, \quad (2.2)$$

where the n_i 's $i = 1, 2, 3$, are refractive indices at their respective wavelength denoted by the subscript. In birefringent phasematching the phase mismatch is eliminated by making each wave see a refractive index such that the equalities in Eqs. (2.1,2.2) are satisfied. The refractive index of an extraordinary wave in a uniaxial crystal, such as lithium niobate, depends on the propagation direction of the wave with respect to the optic axis and is given by [46],

$$n(\theta, \lambda) = \frac{n_e(\lambda)n_o(\lambda)}{(n_e^2(\lambda)\sin^2\theta + n_o^2(\lambda)\cos^2\theta)^{\frac{1}{2}}} \quad (2.3)$$

Here n_o is the ordinary index, n_e the extraordinary index and θ is the “propagation angle”, or angle between the k -vector of the wave and the optic axis. The ordinary refractive index is independent of propagation direction. With a uniaxial crystal there are only two possible ways in which phasematching can occur. These are called Type I and Type II phasematching [46]. The phasematching geometries for positive $n_e > n_o$ and negative $n_o > n_e$ uniaxial crystals is given in Table 2.1.

	Type I	Type II
$n_o > n_e$	$n_3^e(\theta)\omega_3 = n_2^o\omega_2 + n_1^o\omega_1$	$n_3^e(\theta)\omega_3 = n_2^o\omega_2 + n_1^e(\theta)\omega_1$
$n_e > n_o$	$n_3^o\omega_3 = n_2^e(\theta)\omega_2 + n_1^e(\theta)\omega_1$	$n_3^o\omega_3 = n_2^e(\theta)\omega_2 + n_1^o\omega_1$

Table 2.1: Type I and Type II phasematching.

The superscripts indicate either extraordinary or ordinary waves and the subscripts once again label the different frequencies. Here $\omega_3 > \omega_2 > \omega_1$. It is also possible in some cases to use Type II phasematching such that the e and o superscripts for the two lower frequency waves in Table 2.1 are interchanged. For this case it has been suggested that instead of referring to this as Type II phasematching, it should be denoted as Type III phasematching [47, 48]. The Type III nomenclature has not been widely used by the scientific community.

Quasi-phasematching was first suggested as a way to adjust for the phase mismatch in a three-wave mixing process by Armstrong, *et al.* in 1962 [33]. The idea is to correct at regular intervals for the phase angle by means of a structural periodicity in the nonlinear material being used. To good approximation, as we show in Section 2.2, Eqs. (2.1,2.2) become, for collinear quasi-phasematching,

$$\frac{1}{\lambda_3} = \frac{1}{\lambda_2} + \frac{1}{\lambda_1}, \quad (2.4)$$

$$\frac{m}{\Lambda_g} = \frac{n_3}{\lambda_3} - \frac{n_2}{\lambda_2} - \frac{n_1}{\lambda_1}, \quad (2.5)$$

where Λ_g is the period of the crystal grating and n is an integer.

Many different materials have been modified to effect QPM by producing a periodic $\chi^{(2)}$ structure. Here $\chi^{(2)}$ is the second order susceptibility and is responsible for the nonlinear processes in three-wave mixing interaction. Some of the materials produced with modified $\chi^{(2)}$ structures include LiNbO_3 [29] and $\text{MgO}:\text{LiNbO}_3$ [49, 50], LiTaO_3 [51], KTP [52], and polymers [53–55]. Several techniques have been employed to effect this structural $\chi^{(2)}$ periodicity with varying degrees of success. For example, stacks of thin plates of several materials, including LiNbO_3 and GaAs were constructed with alternating directions for the effective nonlinear coefficient [56, 57]. Lithium niobate with periodic structures has also been created with laser-heated pedestal growth techniques [58], indiffusing dopants [59], and rotationally twinning layers [60]. To date, the most successful method to create periodic structures in LiNbO_3 has been poling of the crystals to spontaneously reverse the polarization [29]. Because of the good periodic structures and commercial availability, as well as other benefits discussed in Section 2.2, we have chosen to use periodically poled lithium niobate for both the crystals in our OPO-DFM device.

In addition to modulation of $\chi^{(2)}$, quasi-phasematching may also be achieved by modulating the linear susceptibility $\chi^{(1)}$ and hence the material refractive index [61, 62]. In general this technique has been difficult to implement because of the requirement that the index modulation must be comparable to the dispersion.

2.1.1 Periodically poled lithium niobate

PPLN crystals with a thickness of 0.5 mm and periods as short as 10 μm are now routinely manufactured and commercially available. They have been used in a wide vari-

ety of nonlinear devices, a few of which include: pulsed [29], synchronously pumped by pulsed laser [63], cw synchronously pumped [26], and cw OPOs [16], second harmonic generation [60], and difference frequency mixing [64]. An excellent review article on quasi-phasematched devices is given by Byer [28].

The PPLN grating period required to phasematch for a given set of wavelengths can be determined by simultaneously solving Eqs. (2.4,2.5). Since the indices of refraction depend on wavelength, these equations cannot be solved analytically and numerical techniques must be used. The wavelength dependence of the refractive indices is given by Sellmeier equations with experimentally determined coefficients [65]. Phasematching grating-period contours can be plotted in wavenumber-wavenumber (and wavelength-wavelength) space as shown in Fig. 2.1.

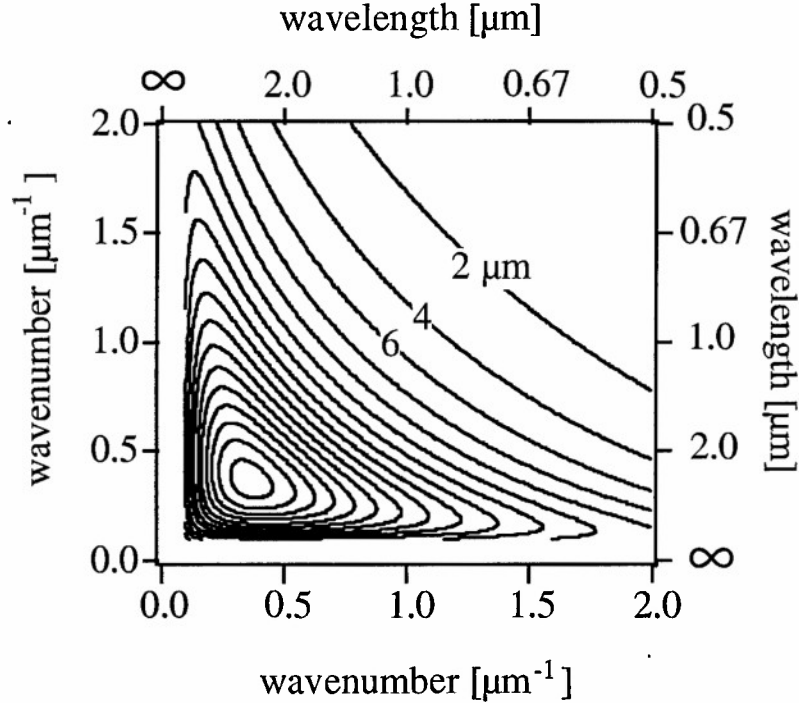


Figure 2.1: Room temperature grating contour diagram for lithium niobate. Contours are solutions to Eqs. (2.4, 2.5) for given PPLN grating period.

These types of plots are referred to as grating contour diagrams [66] and are

symmetric about a diagonal running from the lower left to the upper right corners.

Given the wavelengths of the waves in the interaction, these plots can be used to approximate the required grating period for a three-wave mixing process. This can be determined as follows:

1. For the smallest of the three wavelengths in the interaction draw a line (with a negative unity slope) which intersects the left y -axis and bottom x -axis at the correct wavenumber.
2. Draw two horizontal lines across the grating contour diagram, one intersecting the left y -axis at one of the remaining wavenumbers and one intersecting the left y -axis at the final wavenumber.
3. Repeat step two, except draw vertical lines intersecting the bottom x -axis at the appropriate wavenumbers.
4. There are now two points on the grating contour diagram at which three lines intersect. Due to the symmetry of the diagram, these are the same point in wavenumber-wavenumber space. The PPLN grating period required to phasematch for these three wavelengths is then the contour which passes through these intersection points.

A similar process will identify the two wavelengths that are generated with a given pump: draw a diagonal for the pump, see where it intersects a grating contour, and draw horizontal and vertical lines from this point to identify the signal and idler wavelengths. Grating contour diagrams are helpful in approximating required periods for QPM and/or wavelengths, as well as in identifying additional nonlinear processes which may be phasematched.

Finally, note that a different grating contour diagram would have to be generated for each temperature at which phasematching contours are desired. As the crystal temperature changes, the values for the refractive indices change as well. Thus, the phasematching condition given by Eq. (2.2) is satisfied for a different set of wavelengths. The temperature dependence of the refractive index is modeled by an equation with experimentally determined coefficients [67] and referred to as a Sell-

meier relation. In addition to the materials temperature dependent dispersion, there is the added contribution of the grating period change due to material expansion with temperature. The expansion of lithium niobate with temperature is given as,

$$\frac{d}{d_R} = 1 + \alpha(T - T_R) + \beta(T - T_R)^2 = f(T) \quad (2.6)$$

where d_R is the length of the material at the reference temperature, T_R . The coefficients α and β in Eq. (2.6) depend on the way in which the lithium niobate is oriented. The orientations are referred to as x , y or z cut because of their relationship to the crystallographic axes (a, b, c) and are shown in Fig. 2.2.

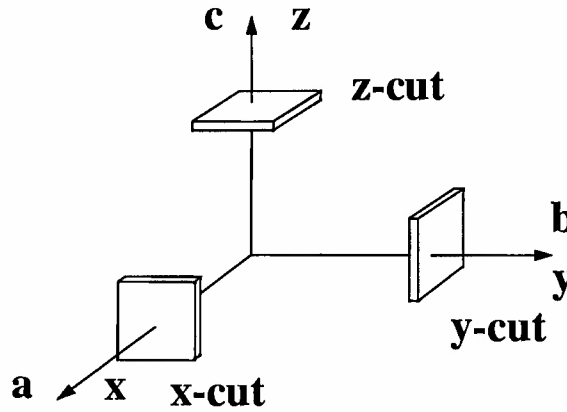


Figure 2.2: Orientations of lithium niobate with respect to crystallographic axes (a, b, c). The PPLN used in our experiments is x -cut.

When birefringently phasematching, thermal expansion of the crystal does not affect the phasematching condition. In lithium niobate, the effect of material expansion on the phasematching condition is small as compared to temperature dispersion. For example, Fig. 2.3 shows theoretical temperature tuning plots of a $29.75 \mu\text{m}$ grating period, PPLN crystal pumped by a $1.064 \mu\text{m}$ source. Tuning of the signal for an

OPO interaction is shown. Two tuning lines are given: one includes refractive index and grating period changes, and the other shows tuning if just the grating period changed.

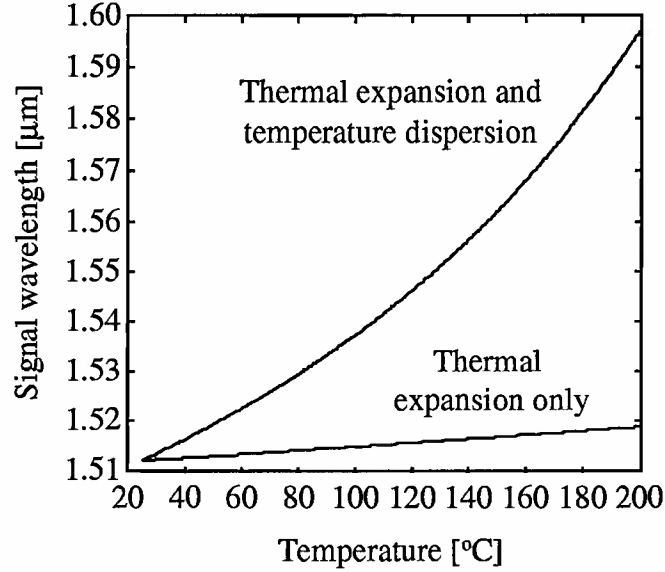


Figure 2.3: Theoretical temperature tuning plots for 29.75 μm PPLN crystal.

2.1.2 Production of periodically poled lithium niobate

Production of PPLN relies heavily on microlithography techniques borrowed from the electronics industry. The entire production process is schematically diagrammed in Fig. 2.4. An aluminum grating with the desired period is patterned by lift-off lithography onto the $+z$ face of a wafer of congruent lithium niobate to create an electrode structure. A layer of photoresist is applied over the grating, leaving a portion of the metal pattern exposed to contact with a liquid electrolyte. The photoresist layer insulates the aluminum electrodes, and forms the contour of an isopotential surface when covered with the electrolyte. This isopotential surface is important in that it controls fringing fields at the edges of the grating lines, improving pattern uniformity.

The $-z$ face is contacted uniformly with the electrolyte. The sample is clamped between high-voltage electrodes. Extra insulation such as O-rings is necessary to prevent arcing. A typical poling configuration is shown in Fig. 2.4(c).

When lithium niobate is then subjected to an electric field on the order of 21 kV/mm, spontaneous polarization occurs [29]. This is called the coercive field. Domain formation has been broken into four distinct phases: nucleation, tip propagation, wall propagation and stabilization [68]. The wall propagation regime determines the final width of the domains.

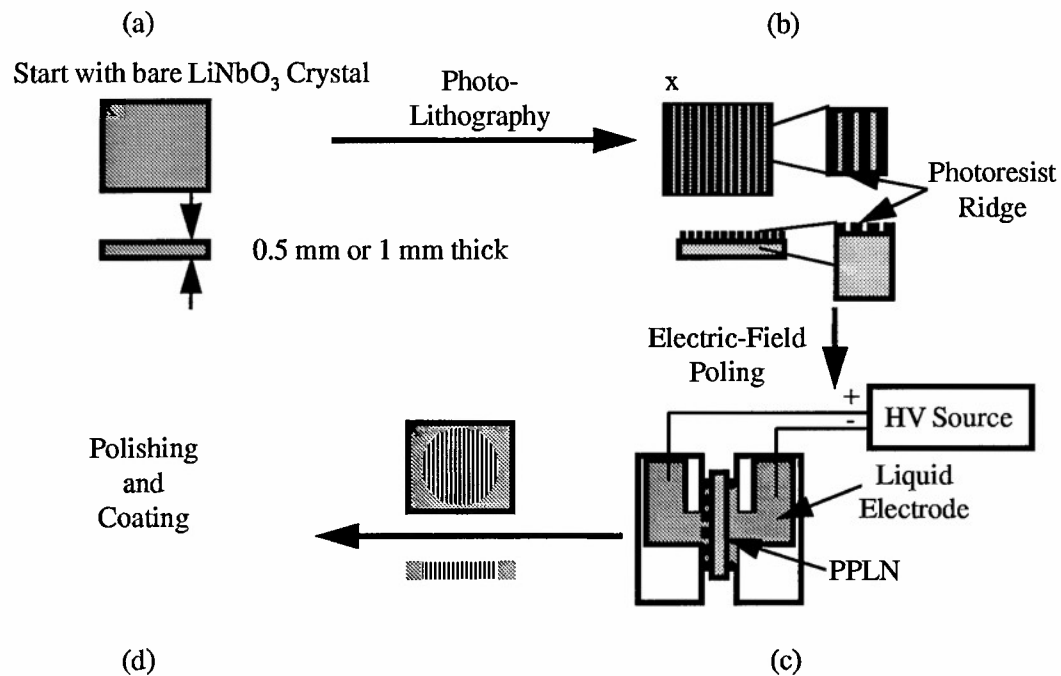


Figure 2.4: Schematic diagram of PPLN production process.

Nucleation occurs as the applied field is raised above the coercive field. For good substrate homogeneity, microscopic domains occur first at the $\pm z$ faces of the lithium niobate. The tips of the nucleated domains then propagate rapidly towards

each other and to the x and y faces of the crystal. As the tips propagate, the domain walls spread out in the x - y plane, widening the domains. In the wall propagation phase, domain walls straighten to become nearly parallel to the z -axis. The domain walls move in the x - y plane with a speed that depends on the applied electric field. In the final phase, domain stabilization, the applied field has to be lowered to zero in a time longer than 60 milliseconds. The reason for this is that during the first three phases an internal electric field is generated. This internal field has a decay constant on the order of 60 milliseconds. Thus, to prevent all of the domains initially formed from reverting to their original state, the applied field must be lowered at a slower rate than this decay time.

2.1.3 Photorefractive effect

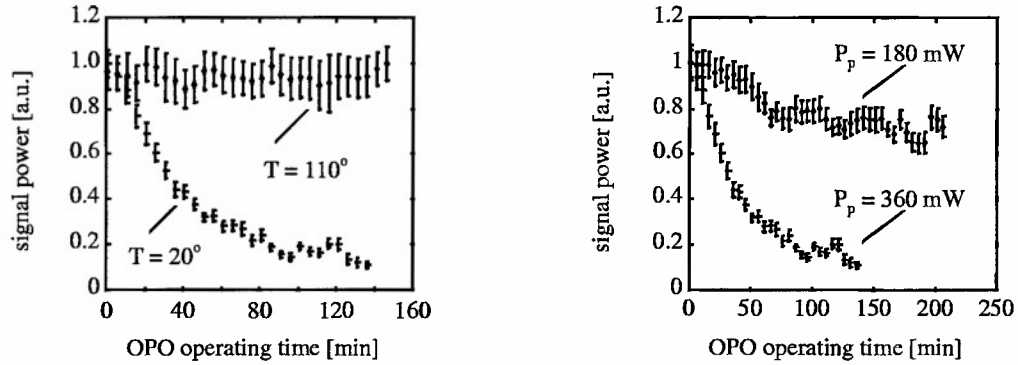
In general, the photorefractive effect is the change in a material's index of refraction due to the optically induced redistribution of electrons and holes in the material and depends upon the linear electro-optic effect. We describe here the general physics of the photorefractive effect. Later in Section 2.3 we develop the basic photorefractive theory and perform a simple quantitative analysis. When a beam is incident on a material, it causes a spatially modulated intensity distribution. Due to the transverse profile of the beam, this distribution is transverse to the propagation direction and creates a transverse electric field. Photo-excited electrons and free carriers drift, due to this electric field, from regions of high intensity to low intensity or to the edges of the beam. (There is a small amount of free carriers, due to donor and acceptor impurities in the crystal.) Once outside of the illuminated region, the charge carriers are retrapped. Thus there is a change in the charge density of the material which causes a local static electric field to be generated. This local static field changes the refractive index of the lithium niobate through the linear electro-optic effect. Experiments have been performed which support this basic process, and changes in refractive index for LiNbO_3 as high as 10^{-3} have been measured [69]. Since this process depends on the

production of photo-excited carriers, it only becomes important for radiation which near the wavelength absorption cut-off for lithium niobate, which is ~ 400 nm at room temperature [70].

The change in refractive index is a local effect and can have a significant effect on the efficiency of a three-wave mixing process by affecting the phase mismatch of the interaction. Even when a system is designed to operate with all wavelengths above the wavelength absorption cut-off line, one still has to be concerned about the photorefractive effect due to non-phasematched conversion processes that may occur, creating radiation with wavelengths below the cut-off. Any device that is pumped by or creates radiation around one micron can be susceptible to the photorefractive effect because this radiation can be converted to green light by non-phasematched SHG which is near the cut-off wavelength.

The photorefractive damage that is caused is not permanent. It has been found that illumination of the material by light or heating of the material will eliminate the damage that was caused [69]. The explanation for this is the trapped electrons are then freed and diffuse to eliminate the charge density gradient, and hence the static electric field and change in refractive index. In fact, several researchers have found that by operating their nonlinear frequency conversion device at high temperature, photorefractive damage could be reduced or avoided during operation [29]. We have also observed this behavior. Figure 2.5(a) shows our experimental results of operation of a ~ 18 W, 100 psec, Nd:YAG, synchronously-pumped PPLN SRO which is phase matched to generate radiation around 1.5 and 3.6 μm for the signal and idler respectively. The PPLN piece was 15 mm long and 0.5 mm thick. The pump is chopped and the average incident power is either 180 or 360 mW. Operation of the SRO resulted in visible green light which was spectrally determined to be the non-phasematched second harmonic of the pump. The plot shows signal power versus time. Note that with 360 mW of incident pump power and the crystal at 20° C the output of the SRO decays to a steady state value: this can be compared to operation of the SRO with the

crystal 110°C where the signal output remains at its original level. This is in good agreement with previous reports [29]. Note that the larger error bars in the measured signal at the higher temperatures are due to fluctuations caused by turbulence from heat convecting from the oven used to heat the PPLN. This is discussed more fully in Section 3.6.2.



(a) OPO signal output versus time for incident pump at 360 mW and crystal at 20°C and 110°C .

(b) Crystal at 20°C and incident pump at 180 mW and 360 mW.

Figure 2.5: Effect of photorefractive damage on OPO output as function of time.

Since the photorefractive effect depends on the number of photo-excited carriers, it should also depend on the average power in the crystal. We found this is indeed the case for our OPO. Figure 2.5(b) shows the signal output versus time and clearly illustrates that when the average power was increased by a factor of two from 180 to 360 mW, the output of the signal declined faster and reached a lower steady state value.

In PPLN the photorefractive effect has been observed to have some unusual features [71] which include two clear symmetric diffraction orders appearing in the far field. The effect occurs only when the PPLN is pumped with green light above a certain threshold power. Below this threshold only a broad spread of scattering

angles is observed. A mechanism to describe these features was reported [72] and hypothesizes that the domain structure of PPLN results in a photorefractive gratings that provides new schemes for four-wave mixing. The photorefractive effect can play a significantly detrimental role in the operation of high average-power devices. Somewhat promising is the fact that the photorefractive effect in PPLN has shown evidence of not being as severe as in unpoled lithium niobate [73]. The reason for this is discussed further in Section 2.3.

2.2 Quasi-phasematching theory

In three-wave mixing, two waves of frequency ω_i and ω_j interact with the nonlinear susceptibility of a material to produce a polarization wave at ω_k . In general the waves travel at different phase velocities and thus there is a continuous phase slip between them. Since the sign of power flow from one wave to another is determined by the relative phase between the waves, there is an alternation in the direction of flow of power from one wave to another. The distance over which the relative phase of the waves changes by π is called the coherence length, l_c .

$$l_c = \frac{1}{2} \left[\frac{n_3}{\lambda_3} - \frac{n_2}{\lambda_2} - \frac{n_1}{\lambda_1} \right]^{-1} \quad (2.7)$$

In practice, one way to make the coherence length infinite and phasematch the interaction is to use the birefringence of an anisotropic material as discussed in Section 2.1. Another way to obtain efficient conversion is to quasi-phasematch the nonlinear process.

The quasi-phasematching concept leads to efficient nonlinear conversion by periodically correcting for the phase mismatch in a three-wave mixing process. There are three main advantages of quasi-phasematching over birefringent phase matching in lithium niobate. First, we can phasematch for any set of wavelengths in the transparency range of the crystal since the grating period is engineerable. As already mentioned, this is not necessarily true for birefringent phasematching.

Second, all the waves in the interaction can be extraordinary and hence there is no spatial walk-off. In general walk-off occurs since the ray direction and Poynting vector (flow of energy) are not parallel to each other for extraordinary waves while for ordinary waves they are. Thus, unless noncritically phasematched (propagation of the waves at $\theta = 90^\circ$ to the optic axis) there will be walk-off between the extraordinary and ordinary waves when birefringently phasematching.

Finally, QPM allows us to access the largest nonlinear coefficient of lithium niobate, which is not possible when birefringently phasematching. For lithium niobate, the quasi-phasematching technique employs the d_{33} coefficient which is given by $d_{33} \sim 27$ pm/V. With birefringent phasematching the d_{31} coefficient must be used with $d_{31} \sim 5$ pm/V. We can now calculate that the nonlinear drive for the quasi-phasematched case is

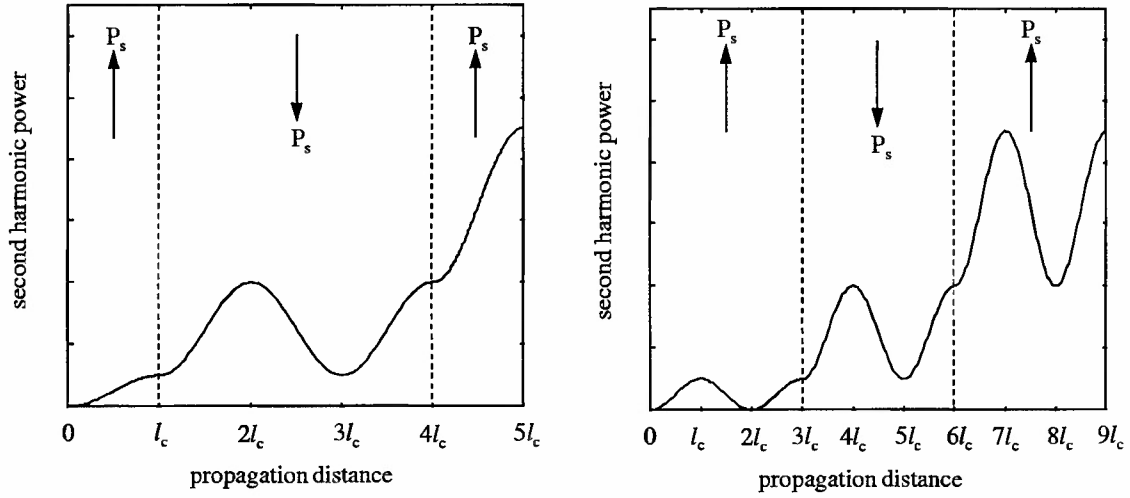
$$\left[\frac{(d_{33}2/\pi)}{d_{31}} \right]^2 \sim 18 \quad (2.8)$$

times greater than the nonlinear drive for the birefringent phasematching case. The appearance of the factor $2/\pi$ in Eq. (2.8) arises in the development of quasi-phasematching theory and is explained later.

The most efficient conversion will be obtained when the sign of the polarization is changed every coherence length. This is called first-order QPM. In general n th order $n = 1, 3, 5 \dots$ odd QPM process can be accomplished by using alternate domain length of nl_c and any m th order $m = 2, 4, 6 \dots$ even QPM process can be accomplished by using alternating domain lengths of $(m-1)l_c$ and $(m+1)l_c$. Second harmonic power as a function of propagation distance are plotted in Fig. 2.6 for second-order and third-order QPM processes.

2.2.1 Analytical approach

The analytical investigation of QPM for SHG has been examined in detail by Fejer *et al.* [74]. Here we modify their approach for a general three-wave mixing process. We



(a) Second-order quasi-phasematching.

(b) Third-order quasi-phasematching.

Figure 2.6: Second harmonic power as function of propagation distance for quasi-phasematched processes.

express the nonlinear susceptibility modulation of the material in terms of a Fourier series representation of the nonlinear coefficient $d(z)$,

$$d(z) = d_{eff} \sum_{m=-\infty}^{\infty} G_m \exp(-iK_m z), \quad (2.9)$$

The nonlinear coefficient is proportional to the nonlinear susceptibility. Here d_{eff} is the effective nonlinear coefficient of the same process in single-domain bulk material and is equal to d_{33} for lithium niobate. $K_m = 2\pi m/\Lambda_g$ and G_m are the grating vector and expansion coefficient respectively of the m th Fourier component and Λ_g is the period of the modulated structure. If the nonlinear coefficient $d(z)$ is placed into the coupled plane-wave equations for three-wave mixing we find that there are an infinite number of driving terms in each of the coupled wave equations. The driving term in each wave equation that is phasematched will dominate and we can ignore the other non-phasematched components. The coupled plane-wave equations in the time

domain for a general three-wave mixing process are then written

$$\begin{aligned}\frac{dE_1}{dz} &= i \frac{\omega_1 d_Q}{n_1 c} E_3 E_2^* \exp(i \Delta k_Q z) \\ \frac{dE_2}{dz} &= i \frac{\omega_2 d_Q}{n_2 c} E_3 E_1^* \exp(i \Delta k_Q z) \\ \frac{dE_3}{dz} &= i \frac{\omega_3 d_Q}{n_3 c} E_1 E_2 \exp(-i \Delta k_Q z)\end{aligned}\quad (2.10)$$

which have analytical solutions in terms of Jacobi-elliptic functions. In these equations the effective nonlinear coefficient for the QPM interaction is,

$$d_Q = d_{eff} G_m \quad (2.11)$$

and d_{eff} is assumed to have no frequency dependence. The phase mismatch for a collinear QPM interaction is,

$$\Delta k_Q = k_3 - k_1 - k_2 - K_m \quad (2.12)$$

In writing Eqs. (2.10) we have also have neglected group velocity and group velocity dispersion terms, as well as higher order terms stemming from the frequency dependence of the wavevectors.

Note that there is now an extra degree of freedom in the phase mismatch term, the grating period, which is engineerable. This is one of the attractive features of the QPM technique. When the polarization is modulated with periodic sign reversals, as in PPLN, simple Fourier analysis gives the Fourier coefficients of Eq. (2.9) as,

$$G_m = \frac{2}{m\pi} \sin(m\pi D) \quad (2.13)$$

where the duty factor $D = l/\Lambda_g$ is given by the length l of the reversed domain divided by the period Λ_g of the grating reversal. For an odd-order QPM processes with a 50% duty cycle we have,

$$d_Q = \frac{2}{m\pi} d_{eff}. \quad (2.14)$$

The theory given here is a very good approximation when there is small nonlinear conversion over a single coherence length. At very high pump levels, it may be possible to have high levels of conversion within a coherence length of the material. The signal and idler waves then act back on the pump wave, introducing a nonlinear phase shift. This nonlinear phase shift changes the required QPM grating period that is needed for efficient conversion. Thus, it is possible that other terms in the Fourier expansion of the grating period can become significant. As an example of this effect on the required period we examine a Nd:YAG pumped PPLN OPO producing radiation near 1.5 and 3.6 μm for the signal and idler respectively. A numerical calculation of the phase mismatch indicates that the required grating period at a pump intensity of 10 MW/cm² is 29.75 μm . At pump powers 1000 times this (10 GW/cm²) a numerical solution to the three coupled wave equations indicates that the grating period should be 29.79 μm or 40 nm longer than at low powers. We should note here that the damage threshold for LiNbO₃ is around 150 MW/cm² for 30 ns pulses [75] so that this 40 nm change in grating period occurs at irradiances far above the damage threshold and thus is not an effect to be concerned with in LiNbO₃.

It has been known for some time that large nonlinear phase shifts due to cascaded $\chi^{(2)}$ effects can occur for parametric processes [76]. These phase shifts can be thought of as being due to effective nonlinear index of refraction n_2^{cascad} [77] and have been observed in LiNbO₃ [78]. For low intensities or large phase mismatch and large $\Delta k_Q L$ an effective n_2 was measured to be $n_2^{\text{cascad}} \approx 2 \times 10^{-13} \text{ cm}^2/\text{W}$.

There is also the usual nonlinear refractive index change at high intensities which depends on the third-order electronic nonlinearity of the material (or third-order susceptibility $\chi^{(3)}$). This nonlinearity can affect the required grating period for generating specific frequencies with nonlinear conversion. The change in refractive index with intensity is mathematically modeled by the equation,

$$n(\lambda, T, I) = n_o(\lambda, T) + n_2 I \quad (2.15)$$

where n_o is the “normal” refractive index at low intensities, I is the irradiance and

T is temperature. n_2 is the nonlinear refractive coefficient with units of cm^2/W . For LiNbO_3 a value for n_2 of $5.3 \times 10^{-15} \text{ cm}^2/\text{W}$ has recently been reported [79]. Calculations indicate that for these values of n_2 and n_2^{cascade} the change in the grating period for QPM is effectively zero for any realistically achievable irradiances.

2.2.2 Tuning characteristics of quasi-phasematched devices

The tuning characteristics of a nonlinear device are important to understand, since they play an important role in device performance. One of the main reasons for using nonlinear devices is their ability to produce output over a wide ranges of frequencies for a given pump frequency. For collinear phasematching, the tuning characteristics can be determined by simultaneously solving Eqs. (2.4, 2.5) for energy and momentum conservation. An illustrative plot of the tuning of a PPLN device with temperature was given in Fig. 2.3. As stated in Section 2.1.1, the tuning for a collinear QPM device depends on two effects, the temperature dependence of the refractive indices given by Sellmeier relations, and the thermal expansion of the PPLN, changing the grating period.

So far we have only examined QPM with collinear interaction of the three beams. Figure 2.7(a) shows a wave-vector diagram for this case. \vec{K}_m is the grating vector component that phasematches the interaction. In general, the phase mismatch is a vector equation and the QPM condition depends on the angles between grating vector \vec{K}_m and the wave vectors \vec{k}_1 , \vec{k}_2 and \vec{k}_3 . Thus, by changing the angle of the QPM crystal with the incident pump, and/or changing the angle between the incident pump and signal (which can be controlled because in an SRO the signal is resonated) it is possible to angle-tune the nonlinear device. Here we are only considering the case where all waves have wave vectors that are perpendicular to the optic (z) axis.

Figure 2.7(b) is a diagram of the wave vectors for a general interaction where all of the vectors are in the plane of the diagram. \vec{k}_3 is at an angle ϕ with respect to the grating vector \vec{K}_m . For an OPO interaction this is the incident pump wave

vector. In the laboratory the grating vector and pump are easily made collinear by retroreflecting the pump from the crystal face. (Assuming the grating vector and crystal faces are perpendicular.) It is possible to achieve other values of ϕ by rotating the crystal azimuthally.

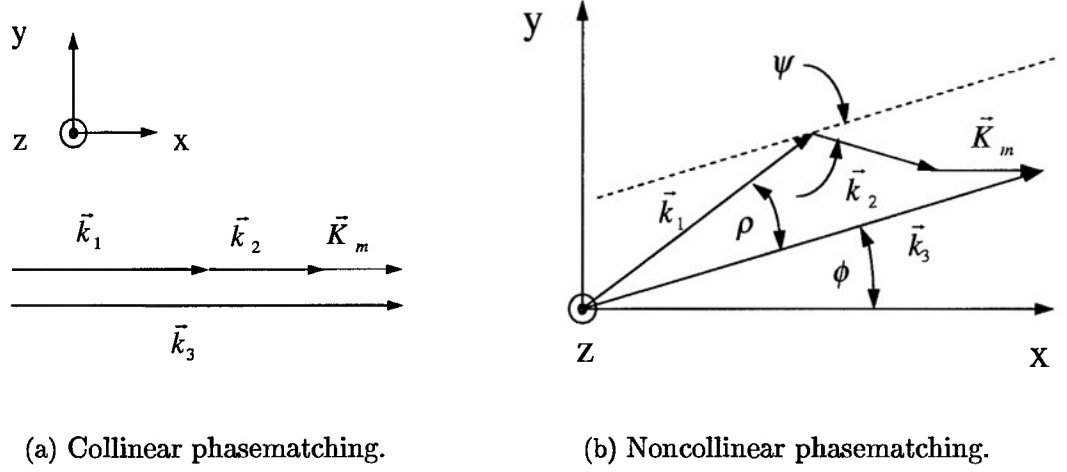


Figure 2.7: Wave vector diagrams for three wave mixing interaction.

Referencing Fig. 2.7(b) we find the two equations,

$$\begin{aligned}
 |\vec{k}_2| \cos(\phi - \psi) + |\vec{k}_1| \cos(\rho + \phi) &= |\vec{k}_3| \cos(\phi) - |\vec{K}_m| \\
 -|\vec{k}_2| \sin(\phi - \psi) + |\vec{k}_1| \sin(\rho + \phi) &= +|\vec{k}_3| \sin(\phi)
 \end{aligned} \tag{2.16}$$

In these equations, $|\vec{k}_l|$, $l = 1, 2, 3$ are functions of wavelength and can be rewritten as, $|\vec{k}_l| = 2\pi n_e(\lambda_l)/\lambda_l$ where n_e is the extraordinary refractive index. These two equations, along with the energy conservation condition Eq. (2.4) give three equations with three unknowns: ρ , ψ , and λ_2 for a given values of ϕ , λ_1 and λ_3 . Note that when ϕ , ρ , and ψ are equal to zero, these two equations correctly reduce to the equations for collinear phasematching, Eqs. (2.4,2.5).

Figure 2.8 examines the specific case of an OPO interaction where $1 \rightarrow s$, $2 \rightarrow i$, and $3 \rightarrow p$. The subscripts s , i , and p represent the signal, idler and pump of

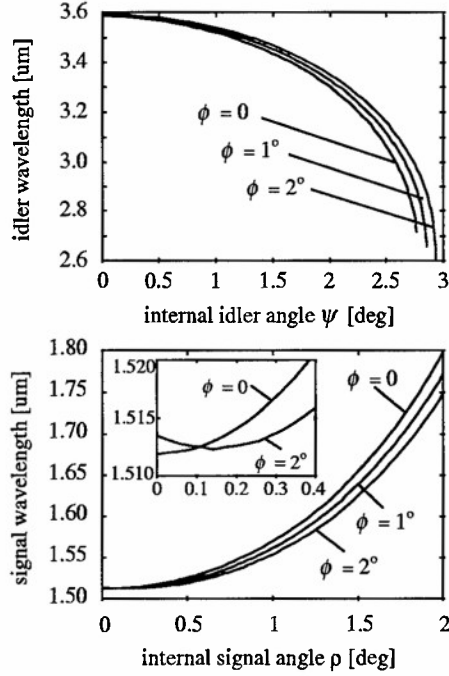


Figure 2.8: Angle tuning plots of signal and idler. ϕ is the angle between the pump and grating vector, ρ the angle between the pump and signal and ψ the angle between the pump and idler.

the interaction. Here we plot theoretical room temperature tuning curves of the signal and idler wavelengths versus the respective phasematching angles ρ and ψ for three different values of ϕ . A vertical line at any point through both figures gives the signal and idler wavelengths, and the corresponding angles, ρ and ψ when phasematched. The pump wavelength used to generate the plots was $1.064 \mu\text{m}$ and the grating period was $29.75 \mu\text{m}$.

There is a large tuning range for the signal and idler when the signal internal angle ρ is varied from 0 to 2 degrees. For non-collinear phasematching, we must keep in mind that even for an $e \rightarrow e + e$ interaction, there will be spatial walk-off between the beams, limiting the interaction length and the nonlinear gain. The walkoff in noncollinear phasematching is different from birefringent walkoff. It is possible to have both types of walkoff present in a nonlinear interaction. Looking at

the inset, we note that when the internal angle is zero the phasematching wavelength of the signal increases for increasing ϕ . The reason for this is that the signal in effect sees a longer grating period when it is at an angle to the grating vector. From Fig. 2.1 we see that a larger grating period implies a longer signal wavelength (and shorter idler wavelength). As the angle ρ between the pump and signal increases from zero the phasematching wavelength of the signal initially decreases (and the wavelength of the idler increases). This can be explained as follows. An increase in ρ means a smaller angle between the signal and grating vector. Thus the signal sees a shorter grating period and thus the phasematching wavelength moves closer to the phasematching wavelength for a collinear interaction. As ρ continues to increase, the effect of the changing refractive indices (because of changing wavelengths) begins to play an important role and the signal wavelength begins to increase as in the case where ϕ is zero.

2.2.3 Bandwidth characteristics of quasi-phasematched devices

The method used to evaluate the bandwidth characteristics of nonlinear devices is well known [24]. More specifically, Fejer, *et al.* [74] have addressed the theory of tuning and tolerances for QPM second harmonic generation. We follow Fejer's work here modifying it for a general three-wave mixing process.

If the wave equations, Eqs. (2.10), are solved with the assumption that there is no pump depletion, called the small-signal regime, one finds that the small-signal gain G of the device is dependent on the phase mismatch as,

$$G = \Gamma^2 L^2 \frac{\sinh^2\left(\sqrt{\Gamma^2 - \frac{\Delta k_Q^2}{4}} L\right)}{\left(\Gamma^2 - \frac{\Delta k_Q^2}{4}\right) L^2} \quad (2.17)$$

L is the length of the crystal and Γ is a parameter that depends the crystal material properties, wavelengths of the radiation taking part in the interaction, and the

incident pump power. For interactions in the small signal regime and with phase mismatch such that $\Delta k_Q^2 L^2/4 \gg \Gamma^2 L^2$ we find for the small signal gain G ,

$$G = \Gamma^2 L^2 \text{sinc}^2\left(\frac{\Delta k_Q L}{2}\right) \quad (2.18)$$

The small signal gain is down to half of its maximum when $\Delta k_Q L/2 = 0.4429\pi$. We use this criterion below to calculate various bandwidths that characterize nonlinear QPM devices.

In general, the phase mismatch Δk_Q is a function of wavelength λ and general parameter η . Examples of specific parameters that η can be replaced with are temperature T and spectral frequency ω . The phase mismatch is expanded in a power series about the phasematching parameter η_o which achieves QPM for $\lambda = \lambda_o$, so that $\Delta k_Q(\eta_o, \lambda_o) = 0$ to obtain:

$$\Delta k_Q L(\eta, \lambda) = (\eta - \eta_o) \frac{\partial \Delta k_Q L}{\partial \eta} + (\lambda - \lambda_o) \frac{\partial \Delta k_Q L}{\partial \lambda} + \frac{1}{2}(\eta - \eta_o)^2 \frac{\partial^2 \Delta k_Q L}{\partial \eta^2} \quad (2.19)$$

If Δk_Q has a first order dependence on η we neglect higher order dependencies in the expansion. The FWHM bandwidth in η , denoted $\delta\eta$, is found by fixing $\lambda = \lambda_o$ and solving Eq. (2.19) for the value of $(\eta - \eta_o)$ which satisfies $\Delta k_Q L/2 = 0.4429\pi$ and then doubling it. This gives,

$$\delta\eta = 5.57 \left| \frac{\partial \Delta k_Q L}{\partial \eta} \right|^{-1} \quad (2.20)$$

Eqs. (2.19,2.20) will now be used to derive useful equations for various acceptance bandwidths of a three-wave mixing process.

As stated earlier, in the nonlinear conversion process energy must be conserved and the most efficient conversion from pump to idler and signal is when the phasematching condition $\Delta \vec{k}_Q = 0$ is satisfied. The phasematching condition is only satisfied for the midband wavelengths of the three waves and does not occur at all frequencies within the spectral range of each of the pulses. This is especially important when dealing with broad spectral widths of ultrashort pulses. Using Eqs. (2.19,2.20)

we find that the phasematching spectral bandwidth for fixed wavelength λ_3 is given by,

$$\delta\omega = \frac{5.57c}{L} \left(n_2 - n_1 + \omega_2 \frac{dn_2}{d\omega} \Big|_{\omega_2} - \omega_1 \frac{dn_1}{d\omega} \Big|_{\omega_1} \right)^{-1} \quad (2.21)$$

where c is the speed of light. Note that the grating vector K_m does not contribute to this bandwidth since it is independent of wavelengths (or frequencies) of the interacting waves. As an example of the magnitude of this bandwidth we examine the following OPO interaction. We take a 13 mm piece of PPLN with a $29.75 \mu\text{m}$ grating period that is pumped by $1.064 \mu\text{m}$ radiation. Phasematching gives an idler wavelength of $\lambda_i = 3.55 \mu\text{m}$ and a signal wavelength of $\lambda_s = 1.5 \mu\text{m}$ at 25°C . This gives a spectral bandwidth of $\delta\omega = 3.97 \times 10^{12} \text{ sec}^{-1}$, or in terms of wavelength, $\delta\lambda = 4.8 \text{ nm}$. It is relevant to note that the spectral width of a 100 psec pulse is about 0.01 nm and the spectral width of a 100 fsec pulse about 5 nm. At longer wavelengths, the spectral bandwidth tends to increase because of the decrease in dispersion.

Because of photorefractive effects which were mentioned earlier, it is usually necessary to heat the crystal for extended efficient operation. Heating the crystal is also a way to tune the output of nonlinear devices because of the dependence of the refractive indices and grating period on temperature. There will be a limitation to the temperature stability of any feedback control system. For this reason one needs to know the temperature acceptance bandwidth. Referring to Eq. (2.19) we see that we need the derivative of $\Delta k_Q L$ with respect to temperature. The length L of the crystal and the grating period have explicit dependencies on temperature given by Eq. (2.4). Thus we have,

$$\begin{aligned} \frac{\partial \Delta k_Q L}{\partial T} &= \left[\frac{\partial \Delta k_Q}{\partial T} L_R f(T) \right] + \left[\Delta k_Q L_R \frac{\partial f(T)}{\partial T} \right] \\ \frac{\partial \Delta k_Q L}{\partial T} &= \left[\frac{\partial \Delta k}{\partial T} L_R f(T) + \frac{2\pi}{\Lambda_R f^2(T)} \frac{\partial f(T)}{\partial T} L_R f(T) \right] + \\ &\quad \left[\Delta k L_R \frac{\partial f(T)}{\partial T} - \frac{2\pi}{\Lambda_R f(T)} L_R \frac{\partial f(T)}{\partial T} \right] \end{aligned} \quad (2.22)$$

where L_R and Λ_R are the crystal length and grating period at the reference temper-

ature, $\Delta k = 2\pi(n_3/\lambda_3 - n_1/\lambda_1 - n_2/\lambda_2)$ is the crystal material phase mismatch (no grating contribution), and $f(t)$ is given by Eq. (2.6). The second and fourth terms of this expression cancel leaving no dependence on the grating period. Plugging Eq. (2.22) into Eq. (2.20),

$$\delta T = 5.57 \left| \frac{\partial L}{\partial T} \Delta k + L \frac{\partial \Delta k}{\partial T} \right|^{-1} \quad (2.23)$$

Using the same OPO example as earlier, this gives a rather large temperature acceptance bandwidth of 16.6° C. As in spectral bandwidths, the temperature bandwidth increases for longer wavelengths.

The pump laser will have a linewidth and pointing stability. Therefore acceptance bandwidths of the pump wavelength and angular acceptance should be quantified. Here the pump is considered the wave with the shortest wavelength. The acceptance bandwidth for the pump is determined by taking the derivative of $\Delta k_Q L$ with respect to the pump wavelength while fixing the signal wavelength. We get,

$$\begin{aligned} \frac{d\Delta k_Q L}{d\lambda_3} &= 2\pi L \left[\frac{1}{\lambda_3} \frac{dn_3}{d\lambda_3} - \frac{n_3}{\lambda_3^2} - \left(\frac{1}{\lambda_2} \frac{\partial n_2}{\partial \lambda_2} - \frac{n_2}{\lambda_2^2} \right) \frac{\partial \lambda_2}{\partial \lambda_3} \right] \\ \frac{d\Delta k_Q L}{d\lambda_3} &= 2\pi L \left[\frac{1}{\lambda_3} \frac{dn_p}{d\lambda_3} - \frac{n_3}{\lambda_3^2} + \frac{\lambda_1 \lambda_3}{(\lambda_1 - \lambda_3)^2} \right. \end{aligned} \quad (2.24)$$

$$\left. - \left(\frac{1}{\lambda_2} \frac{\partial n_2}{\partial \lambda_2} - \frac{n_2}{\lambda_2^2} \right) \left(\frac{\lambda_1}{\lambda_1 - \lambda_3} \right) \right] \quad (2.25)$$

The grating period does not depend on the wavelength and thus does not show up in the derivative. Specifically for the OPO interaction, we plug Eq. (2.25) into Eq. (2.20) to obtain a relation for the acceptance bandwidth of the pump laser $\delta\lambda_p$ when the signal wavelength is fixed. A value of $\delta\lambda_p = 1$ nm is obtained for the example. For comparison our Nd:YAG pump laser has a linewidth of 20 GHz or 0.1 nm which is well within the acceptance bandwidth of the example device.

To derive an equation for the acceptance angle, we need to determine how the phase mismatch $\Delta k_Q L$ depends on angle of the incident pump angle with the grating vector. First we calculate the angular acceptance bandwidth for a material

that is assumed to be isotropic. This condition holds for PPLN material as long as the propagation of the waves is in the plane perpendicular to the optic axis (the $x - y$ plane). Furthermore, we fix the wavelengths of the interacting waves. For simplicity we suppose that waves 1 and 2 change direction, but remain collinear as the angle ν between the wavevector for 3 and the normal $\hat{\eta}$ to the crystal input face is changed. Figure 2.9 shows the geometry for this case. Here $\hat{\tau}$ is a tangential unit vector to the crystal input face. Initially we take the $\hat{\eta}$ and $\hat{\tau}$ axes to be the x and y axes respectively. The geometry is then the same as Fig. 2.7 except that the grating vector and $\hat{\eta}$ are now at an arbitrary angle κ as opposed to being parallel to each other. As before, ϕ is the angle between the grating vector and direction of pump propagation. We note here that in the experiments we performed with PPLN, this angle is zero.

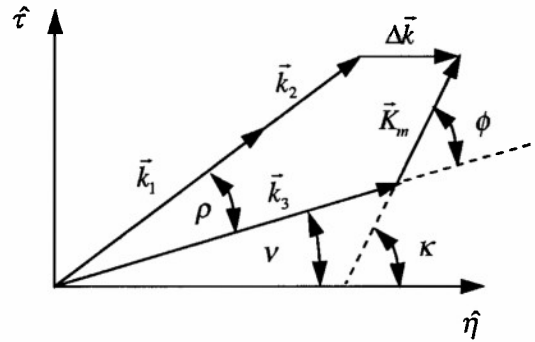


Figure 2.9: Wave vector diagram for QPM angle acceptance bandwidth analysis. The idler and signal wavevectors are chosen to be parallel for simplicity as was done previously [29]. ρ is the angle between the pump and signal and idler wavevectors. The angle between the pump and grating vectors is ϕ .

From Fig. 2.9 we identify the two boundary conditions,

$$(|\vec{k}_1| + |\vec{k}_2|) \sin(\nu + \rho) - |\vec{K}_m| \sin(\kappa) - |\vec{k}_3| \sin(\nu) = 0 \quad (2.26)$$

$$(|\vec{k}_1| + |\vec{k}_2|) \cos(\nu + \rho) - |\vec{K}_m| \cos(\kappa) - |\vec{k}_3| \cos(\nu) = \Delta k_Q \quad (2.27)$$

Now holding the wavelengths fixed and taking the derivative of Δk_Q with respect to

the pump angle ν we get,

$$\frac{\partial \Delta k_Q}{\partial \nu} = -(|\vec{k}_1| + |\vec{k}_2|) \sin(\nu + \rho) \left(1 + \frac{d\rho}{d\nu} + |\vec{k}_3| \sin(\nu) \right) \quad (2.28)$$

Evaluating Eq. (2.28) for the phasematched case and using Eq. (2.20) we have,

$$\begin{aligned} \delta\nu &= 5.57 \left| \frac{\partial \Delta k_Q L}{\partial \nu} \right|^{-1} \\ \delta\nu &= \frac{5.57 \cos(\nu)}{|\vec{K}_m| L \sin(\kappa - \nu)} \left[1 + \frac{\cos(\kappa) |\vec{K}_m|}{\cos(\nu) |\vec{k}_3|} \right] \quad (\phi \neq 0) \end{aligned} \quad (2.29)$$

For phasematching with $\phi = 0$ (the usual case) the phase mismatch has no first-order dependence on the angle ν and the second derivative term of Eq. (2.19) must be used. Performing the necessary algebra and evaluating the second derivative for $\Delta k_Q L = 0$,

$$\delta\nu = 2 \sqrt{\frac{1.722 l_c}{L} \cos(\nu) \frac{|\vec{k}_1| + |\vec{k}_2|}{|\vec{k}_3|}} \quad (\phi = 0) \quad (2.30)$$

For QPM with $\phi = 0$, the bandwidth depends inversely on the square root of the crystal length, rather than the inverse of crystal length as in QPM with $\phi \neq 0$. For the OPO example we have examined so far we find that for non-critical phasematching with $\phi = 0$, the acceptance bandwidth is $\delta\nu(x, y) = 83$ mrad, where the (x, y) notation here means the pump is tilted in the $x - y$ plane.

If the angle of the incident pump changes in a plane such that the polarizations of the interacting waves do not remain parallel to the optic (z) axis of the crystal, the indices of refraction seen by the waves are no longer constant. For a uniaxial crystal such as PPLN the change in refractive index is given by Eq. (2.6). Referring back to Fig. 2.9, the $\hat{\eta} - \hat{\tau}$ plane is now also the $x - z$ plane with the x -axis along the grating vector. Eqs. (2.30) still apply, but Eq. (2.29) becomes much more complicated. Furthermore, the first derivative again vanishes for the case $\phi = 0$ and the second derivative must be used. After much tedious algebra a complicated expression can be found for the acceptance angle bandwidth. Here we just provide a numerical result for the example with κ equal to zero. We find $\delta\nu(x, z) = 93$ mrad.

A summary of the various acceptance bandwidths are summarized in Table 2.2 for the example chosen. This example was chosen since the experimental results presented in Chap. 3 are for an OPO with these parameters. Furthermore, the 13 mm PPLN piece with the 29.75 μm grating period was the OPO crystal in the OPO-DFM system presented in Chap. 4.

Temp. BW ($^{\circ}\text{C}$)	Pump Accept. BW (nm)	Spectral BW (nm)	Pump Angle Accept. BW (x, y) (mrad)	Pump Angle Accept. BW (x, z) (mrad)
16.6	1.0	4.8	83	93

Table 2.2: Acceptance bandwidths for 13 mm PPLN OPO with the following parameters: operating temperature, 25 $^{\circ}\text{C}$, grating period 29.75 μm , pump wavelength 1.064 μm , signal wavelength 1.51 μm , idler wavelength 3.5 μm , interaction $e \rightarrow e + e$, nonlinear coefficient d_{33} .

2.3 Photorefractive effect in material with periodic $\chi^{(2)}$ structure

In Section 2.1.3 we mentioned that there has been experimental evidence that the photorefractive (PR) effect in PPLN seems to be mitigated as compared to bulk LiNbO_3 [73, 80]. Since high power nonlinear device operation is affected by the PR effect, it is important to understand the reason for the better results with PPLN over a bulk crystal.

As stated earlier, the PR effect is a change in the refractive index of a material. When light is incident on lithium niobate, a space charge field E_{sc} is generated. The linear electro-optic effect [81] then makes use of this field to cause an index change. This change is mathematically given by,

$$\Delta n = \frac{1}{2} n^3 r E_{sc} \quad (2.31)$$

where n is the refractive index and r is the applicable linear electro-optic coefficient. We now qualitatively compare what happens in unpoled and poled lithium niobate when it is irradiated by a Gaussian beam. For both poled and unpoled crystals, the space charge field in lithium niobate is mainly due to the photovoltaic effect. The photovoltaic effect is generation of a current \vec{j}^{pv} by the excitation of photoelectrons into a charge transfer band with a preferential velocity along the polar axis, \hat{c} . For the usual configuration of PPLN where the d_{33} coefficient is used in an $e \rightarrow e + e$ interaction the photovoltaic effect can be modeled as $\vec{j}^{pv} = pI\hat{c}$, where I is the incident light irradiance and p is the Glass photovoltaic constant [82]. This current is the movement of charge carriers to the periphery of the light beam where they are then retrapped causing the space charge field.

In unpoled lithium niobate, the polar axis is in one direction throughout the crystal and the space charge field E_{sc} is purely transverse (see Fig. 2.10(a)). In PPLN the polar axis direction periodically alternates with each ferroelectric domain. This means the photovoltaic current direction alternates as well. The space charge density gradient and space charge field in each ferroelectric region are now reduced since charge is now able to flow in the longitudinal direction due to the longitudinal fields caused by the alternating transverse field directions (see Fig. 2.10(b)). This physically is the main reason for the reduction in the index change for poled crystals.

Taya, *et al.* developed a theory of the steady-state photorefractive index perturbations in PPLN caused by incident light [83]. Here we outline their analysis. The constitutive relation for the current density \vec{j} can be written as,

$$\vec{j} = \mu n \vec{E}_T + pI\hat{c} + \frac{k_B T \mu}{e} \nabla n \quad (2.32)$$

\vec{E}_T is the total space charge field, n is the carrier density, T is temperature, k_B is the Boltzmann constant, e is the electron charge and μ is the mobility. Note that $n\mu$

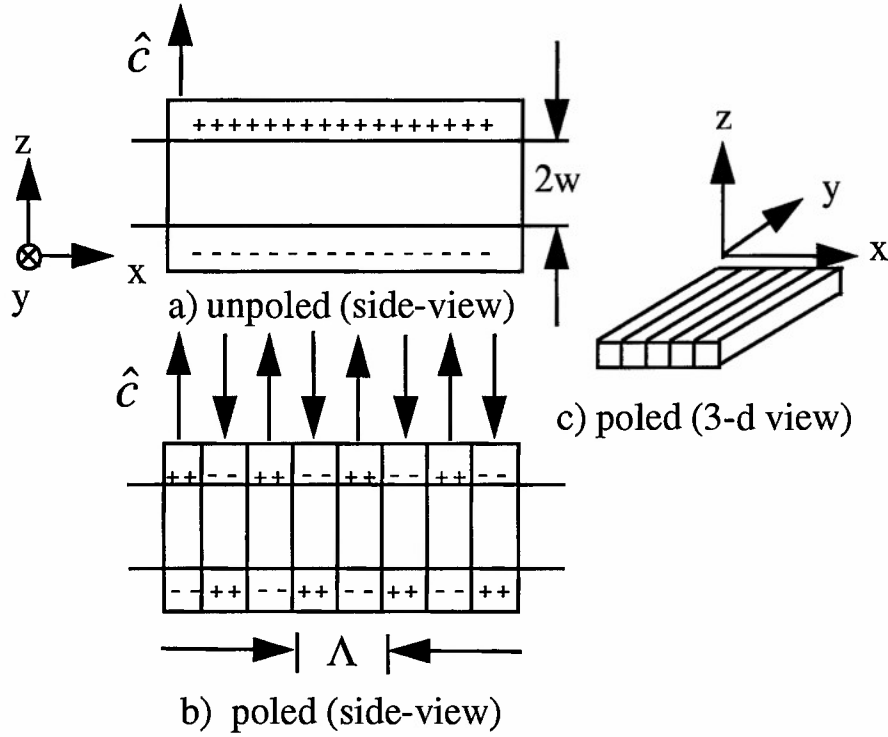


Figure 2.10: Space charges in a) unpoled and b) poled lithium niobate. c) is a 3-d schematic view of a poled crystal. \hat{c} is the optical axis.

is proportional to the photoconductivity of the material. In steady state the current must obey $\nabla \cdot \vec{j} = 0$. For homogeneously poled lithium niobate, p is a constant and the divergence of Eq. (2.32) is directly integrated to give the space charge field,

$$\vec{E}_T = -\frac{1}{n\mu}(pI\hat{c} - \vec{j}_b) + \frac{k_B T}{en}\nabla n \quad (2.33)$$

where \vec{j}_b is a current density given by the boundary conditions. The first term on the right hand side is due to the photovoltaic effect and the last term on the right is due to diffusion. Experimental setups in our lab have open-circuit boundary conditions and $\vec{j}_b = 0$.

For low irradiances the carrier density is given by $n = s_e I + n_d$, where n_d is the dark density and s_e is a constant which depends upon material properties. We can then write for the transverse field,

$$E_z(\zeta) \approx E_{pv}(\zeta, T, I) \left(\frac{\bar{I}(\zeta)}{\bar{I}(\zeta) + I_d(T)/I_o} \right) \quad (2.34)$$

$E_{pv} = -p_b/s_e\mu$ is the photovoltaic field, $I_d = n_d/s_e$ is the dark intensity, I_o the peak irradiance and \bar{I} the normalized irradiance. p_b is a constant that is equal to the bulk value of the Glass coefficient. Here the diffusion part of the space charge field has been neglected since it is several orders of magnitude smaller than the photovoltaic field.

For a QPM material such as PPLN, integration of Eq. (2.32) is more complicated because of the longitudinal dependence of the Glass photovoltaic coefficient $p = p(z)$. Thus a Fourier analysis is performed where the Glass coefficient is expanded in a Fourier cosine series with $K_m = mK_g$ as the expansion vectors and a_m as the expansion coefficients. Here m is an integer and K_g is the PPLN grating vector. Furthermore, instead of working with the electric-field, they use the scalar potential ϕ where $\vec{E}_T = \nabla\phi$ and obeys the equation,

$$\nabla \cdot (n\mu\nabla\phi) = \hat{c} \cdot \nabla(pI) \quad (2.35)$$

(Again the diffusion field has been neglected.) Expanding the potential in a Fourier cosine series, and using some simple assumptions they could then relate independently each Fourier component of the potential in terms of the corresponding Fourier component of the Glass coefficient. Doing this they determined the transverse and longitudinal components of the space charge field in PPLN. They are given by,

$$E_{z,m} \approx - E_{pv}(\zeta, T, I) \frac{a_m}{(K_m w)^2} \frac{d}{d\zeta} \left(\frac{\bar{I}(\zeta)}{\bar{I}(\zeta) + I_d(T)/I_o} \frac{d\bar{I}(\zeta)}{d\zeta} \right) \quad (2.36)$$

$$E_{x,m} \approx E_{pv}(\zeta, T, I) \frac{a_m}{K_m w} \left(\frac{\bar{I}(\zeta)}{\bar{I}(\zeta) + I_d(T)/I_o} \frac{d\bar{I}(\zeta)}{d\zeta} \right) \quad (2.37)$$

Note that due to the ability for space charge to move longitudinally in response to the longitudinal field, the transverse field (and hence index change) in PPLN is

reduced by a factor of $(K_m w)^2$ compared to the unpoled case. w is the laser waist size. These results were derived with a duty cycle of 50% which is the ideal case. If there is even a small deviation from the 50% duty cycle, the reduction predicted for the ideal case can be strongly reduced. The reason for this is that for duty cycles other than 50%, the Fourier expansions give dc ($m = 0$) components of the Glass coefficient and hence, the space charge field. This dc space charge field is not affected by the $(K_m w)^{-2}$ factor that the ac components ($m \neq 0$) are, so that the dc component of the field can be larger than the ac components.

Their result makes physical sense in that the reduction factor becomes smaller as the grating period increases. A typical grating period of around 20 μm and laser waist size of 100 μm predicts reductions of about 1000 in the refractive index change.

We now use Taya's model to obtain numerical results that predict the PR refractive index change in unpoled lithium niobate at room temperature. Numerical results can be benchmarked against reported results in the literature for the index change.

The dependence of the carrier density on physical properties of the material can be determined by solving a set of equations for the electron density n_{e^-} which include rate and current equations for electrons, equation of continuity, Poisson's equation, and an equation for the total number of dopants in the material participating in the photorefractive process. These equations are commonly referred to as Kukhtarev's equations [84]. These equations depend on I the light irradiance, N_D , the total number density of dopants responsible for the photorefractive effect, N_A , the number density of negative ions that compensate for the charge related to the acceptor sites in the dark, as well as γ , s , and β which are the recombination coefficient, cross section of photoionization and dark generation rate respectively. Linearizing the equations we find that to lowest order the carrier density is given by,

$$n_{e^-} = \frac{(sI + \beta)(N_D - N_A)}{N_A \gamma} \quad (2.38)$$

where we have made the assumption that $n_e \ll N_A$ and $(N_D - N_A)$. This is a good

approximation for lithium niobate at irradiances $< 1.7 \text{ kW/m}^2$ since typical carrier densities for this irradiance are $< 10^{21} \text{ m}^{-3}$. Typical values of N_A and $(N_D - N_A)$ are $10^{23} - 10^{25} \text{ m}^{-3}$. Eq. (2.38) gives formulas for s_e and n_d in terms of material properties and are given by,

$$s_e = \frac{s(N_D - N_A)}{N_A \gamma} \quad (2.39)$$

$$n_d = \frac{\beta(N_D - N_A)}{N_A \gamma} \quad (2.40)$$

Plugging Eqs. (2.39,2.40) into Eqs. (2.31,2.37,2.38) for for the periodically poled case and Eqs. (2.31,2.34) for the homogeneous case we are able to predict refractive index changes due to the PR effect in homogeneously poled and periodically poled lithium niobate. Figure 2.11 shows the refractive index changes for 20 mW of incident light focused into a $50 \mu\text{m}$ waist size. The peak refractive index change of $\sim 5 \times 10^{-3}$ at 20° C for the homogeneously poled crystal agrees well with published data for steady state changes [69].

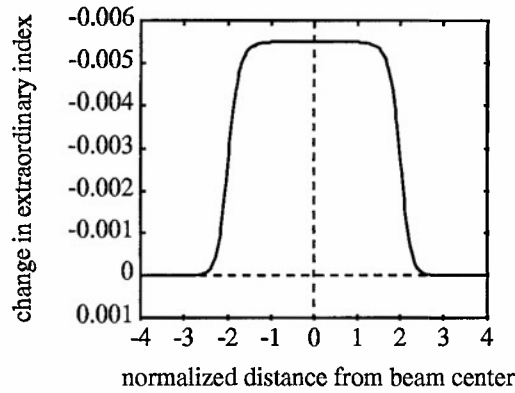


Figure 2.11: Theoretical refractive index changes due to photorefractive effect in lithium niobate for a homogeneous crystal. Crystal are at room temperature. Cross section of beam used in calculation was Gaussian and x -axis is normalized to the waist.

2.3.1 Alternative QPM materials

The use of PPLN in high average-power devices may be limited due to the photorefractive effect. Because of this, it is important to identify possible methods using QPM materials to push to high average-powers. It is well known that the PR effect can be erased in real time by heating the crystal [69]. Published results show that by heating the crystal to 170° C there is no distortion of an incident light beam. We have observed in the work performed here that heating of the PPLN crystals does indeed prevent PR damage. Experimental results were plotted in Fig. 2.5.

Another way to push to higher average power is to use nonlinear materials which are more resistant to the PR effect. A good candidate would be MgO doped LiNbO₃. It has been reported that LiNbO₃ doped with concentrations of MgO above 4.6% can sustain incident cw power levels of radiation 100 times that of LiNbO₃ at room temperature without photorefractive damage [73, 80]. The reason for this enhanced resistance is due to the 100 fold increase in photoconductivity. We can see from Eq. (2.31) that as the photoconductivity increases, the transverse field decreases, and hence so does the change in refractive index of the material. Recently, bulk MgO doped LiNbO₃ crystals have been poled using a corona discharge method, producing grating periods as short as 4.75 μm [49]. The samples were successfully used in intracavity frequency doubling of a diode pumped 946-nm Nd:YAG laser.

Finally we should mention that use of materials not susceptible to the PR effect would be ideal. There are a few materials such as KTP [62] and it's isomorphs [85] and GaAs [86] that have been engineered for quasi-phasematched interactions and research is currently being conducted. For example, bulk GaAs that can be QPM [86] has been produced by diffusion bonding GaAs wafers with alternating directions of the \hat{c} axis to create a crystal with a periodic grating. With GaAs there is also the added benefit of the large nonlinear coefficient: d_{14} of GaAs is about five times greater than d_{33} of LiNbO₃ [87] and transparency range out to 16 μm [88]. A drawback of GaAs, depending on the application, is that it is not good in the visible.

Chapter 3

Synchronously pumped optical parametric oscillator using periodically poled LiNbO₃

3.1 Introduction

As mentioned previously, the optical parametric oscillator (OPO) is a relatively efficient source of tunable mid-infrared radiation. We also covered the advantages of using PPLN crystals and QPM techniques for the nonlinear interaction. Specifically, PPLN eliminates many of the problems associated with conventional birefringent phasematching such as low nonlinear coefficients and spatial walk-off. Thus, we have chosen to use PPLN for both the OPO and DFM interactions in our OPO-DFM device.

A good understanding of the OPO-DFM device can start with a thorough characterization and understanding of the OPO without intracavity DFM. We can consider the OPO to form a baseline operating parameter regime for the OPO-DFM device. Thus, in this chapter the characterization of a synchronously pumped optical parametric oscillator with PPLN will be discussed. Theoretical, computational and

experimental results are presented. Particular emphasis is placed upon temporal and spatial characteristics of the transmitted pump pulses including the behavior of back-conversion. The reason for this is that the OPO-DFM device is predicted to mitigate back-conversion effects. In fact, plane-wave analysis predicts complete pump depletion over a large dynamic range of incident pump intensities. The plane-wave theory of the OPO-DFM device is discussed in Chap. 4

3.2 Coupled wave equations

The plane-wave equations for three-wave mixing were already introduced in Chap. 2. In the following two Sections we derive these equations in detail. A thorough derivation is important so that when we begin to make approximations in the theoretical models we understand what limitations these place on the validity of the models.

3.2.1 Nonlinear polarization

The strength of the second-order nonlinear interaction of light beams is characterized by the second-order nonlinear polarization \vec{P} . In general we can write for the nonlinear polarization,

$$\vec{P}(\vec{r}, t) = p(\vec{r}, t)e^{i\vec{k}\cdot\vec{r} - i\omega_n t} + \text{c.c.} = \vec{p}(\omega_n)e^{-i\omega_n t} + \text{c.c.} \quad (3.1)$$

where $\vec{p}(\vec{r}, t)$ is a slowly varying envelop. We now define cartesian components of the second-order susceptibility tensor χ_{ijk} as the constants of proportionality in the equation

$$P_i(\omega_n + \omega_m) = \epsilon_0 \sum_{j=1}^3 \sum_{k=1}^3 \sum_{(nm)} \chi_{ijk}(\omega_n + \omega_m; \omega_n, \omega_m) E_j(\omega_n, \omega_m) E_k(\omega_m). \quad (3.2)$$

Here the subscripts i , j , and k all run from one to three. The notation (nm) means to perform summation over n and m such that the sum $\omega_n + \omega_m$ is held fixed. Thus the nonlinear susceptibility tensor has 27 components. $E_j(\omega_q)$ is the j th component

of the field at the frequency of the argument ω_q and ϵ_0 is the permittivity of free space. In general, experimentalists use the nonlinear coefficient d rather than the second-order susceptibility to characterize a given interaction. In this work we use the nonlinear coefficient. There is some ambiguity to the relationship between the nonlinear susceptibility and the nonlinear coefficient [24]. We use the relationship,

$$d_{ijk} = \frac{1}{2}\chi_{ijk}. \quad (3.3)$$

Very often in nonlinear optics the nonlinear coefficient is taken to be independent of the frequencies of the interaction. This approximation is very good when the frequencies of interest are in the transmission range of the material. Thus one is free to permute any two indices of the nonlinear coefficient. This is referred to as Kleinman's symmetry. [89] Because of the overall permutation symmetry of the nonlinear coefficient, one is able to introduce a condensed notation so that the components of the coefficient are described by two subscripts rather than three. The condensed notation is given in Table 3.1.

$d_{ijk} = d_{ikj}$	d_{ijk} in condensed notation
d_{i11}	d_{i1}
d_{i22}	d_{i2}
d_{i33}	d_{i3}
d_{i23}	d_{i4}
d_{i13}	d_{i5}
d_{i12}	d_{i6}

Table 3.1: Condensed notation for nonlinear coefficient when Kleinman's symmetry conjecture is applicable.

For a given experimental geometry an effective nonlinear coefficient for the nonlinear interaction can be determined. For example, suppose we have LiNbO_3 as the crystal and two linearly polarized plane waves traveling in the crystal at an angle θ to the optic axis. Further, we take the plane containing the optic axis and the

propagation direction of the rays to make an angle ϕ with the x -axis. We then find,

$$d_{eff} = d_{31} \sin(\theta) - d_{22} \cos(\theta) \sin(3\phi) \quad (3.4)$$

for Type I phasematching. More specifically for our experiment, where the three interacting waves are extraordinary, we find that $d_{eff} = d_{33}$. Recalling the discussion of quasi-phasematching in Sec. 2.2, the nonlinear coefficient then seen by the waves for first order QPM is given by $d_Q = d_{eff}2/\pi$.

3.2.2 Derivation of coupled-wave equations

The derivation of the wave equations starts with Maxwell's equations. (Of course no optics dissertation would be complete without referencing these equations.)

$$\vec{\nabla} \times \vec{E} = -\frac{\partial \vec{B}}{\partial t} \quad \vec{\nabla} \times \vec{H} = \vec{J} + \frac{\partial \vec{D}}{\partial t} \quad (3.5)$$

$$\vec{\nabla} \cdot \vec{D} = 0 \quad \vec{\nabla} \cdot \vec{B} = 0 \quad (3.6)$$

In addition to these we also have the constitutive relations,

$$\vec{D} = \epsilon_0 \epsilon \vec{E} + \vec{P} \quad (3.7)$$

$$\vec{B} = \mu_0 \vec{H} \quad (3.8)$$

The linear polarization is contained in ϵ so that \vec{P} contains only the nonlinear polarization terms. Now taking the waves to be plane-waves traveling in the z -direction (and thus, neglecting diffraction) we find,

$$\frac{\partial^2 E}{\partial z^2} - \mu_0 \sigma \frac{\partial E}{\partial t} - \mu_0 \epsilon_0 \epsilon \frac{\partial^2 E}{\partial t^2} = \mu_0 \frac{\partial^2 P}{\partial t^2} \quad (3.9)$$

Using the slowly varying envelope approximation (SVEA) [90] we find,

$$\left(\frac{\partial}{\partial z} + \frac{1}{v_{g1}} \frac{\partial}{\partial t} + \alpha_1 + i \frac{D_1}{2\omega_1 c} \frac{\partial^2}{\partial t^2} \right) E_1(z, t) = \frac{i\omega_1^2}{k_1 c^2} d_{eff} E_2^* E_3 e^{i\Delta k z}, \quad (3.10)$$

$$\left(\frac{\partial}{\partial z} + \frac{1}{v_{g2}} \frac{\partial}{\partial t} + \alpha_2 + i \frac{D_2}{2\omega_2 c} \frac{\partial^2}{\partial t^2} \right) E_2(z, t) = \frac{i\omega_2^2}{k_2 c^2} d_{eff} E_1^* E_3 e^{i\Delta k z}, \quad (3.11)$$

$$\left(\frac{\partial}{\partial z} + \frac{1}{v_{g3}} \frac{\partial}{\partial t} + \alpha_3 + i \frac{D_3}{2\omega_3 c} \frac{\partial^2}{\partial t^2} \right) E_3(z, t) = \frac{i\omega_3^2}{k_3 c^2} d_{eff} E_1 E_2 e^{-i\Delta k z}, \quad (3.12)$$

Here $E_j(z, t)$ is the electric field envelope of the j th wave. α_j is the loss of the j th wave given by $1/2\mu_0\sigma c/n_j$ and σ is the crystal conductivity. v_{gj} and D_j are the group velocity and dimensionless dispersion constant respectively for the j th wave. Finally, Δk is the phase mismatch of the three interacting waves evaluated at the carrier frequencies.

$$v_{gj} = \left(\frac{\partial k_j}{\partial \omega} \right)^{-1} \Big|_{\omega_j} \quad (3.13)$$

$$D_j = c\omega_j \left(\frac{\partial^2 k_j}{\partial \omega^2} \right) \Big|_{\omega_j} \quad (3.14)$$

When we employ the coordinate transformation $\zeta = z$ and $\tau = t - (z/v_{g3})$ Eqs. (3.10–3.12) become,

$$\left(\frac{\partial}{\partial \zeta} + \frac{\delta T_{13}}{L} \frac{\partial}{\partial \tau} + \alpha_1 + i \frac{D_1}{2\omega_1 c} \frac{\partial^2}{\partial \tau^2} \right) E_1 = \frac{i\omega_1^2}{k_1 c^2} d_{eff} E_2^* E_3 e^{i\Delta k \zeta}, \quad (3.15)$$

$$\left(\frac{\partial}{\partial \zeta} + \frac{\delta T_{23}}{L} \frac{\partial}{\partial \tau} + \alpha_2 + i \frac{D_2}{2\omega_2 c} \frac{\partial^2}{\partial \tau^2} \right) E_2 = \frac{i\omega_2^2}{k_2 c^2} d_{eff} E_1^* E_3 e^{i\Delta k \zeta}, \quad (3.16)$$

$$\left(\frac{\partial}{\partial \zeta} + \alpha_3 + i \frac{D_3}{2\omega_3 c} \frac{\partial^2}{\partial \tau^2} \right) E_3 = \frac{i\omega_3^2}{k_3 c^2} d_{eff} E_1 E_2 e^{-i\Delta k \zeta}, \quad (3.17)$$

where $\delta T_{jk} = L(1/v_{gj} - 1/v_{gk})$ is the walk-off time. This is the amount of time by which two pulses at central frequencies ω_j and ω_k are separated from each other after traveling through a crystal of length L .

We are now in a position to understand some of the approximations we make when we write the simplified Eqs. (2.10). Specifically, we neglect any loss, GVD and GVM of the waves. Furthermore, we assume that Kleinman's symmetry is in effect. When we do this, we get Eqs. (2.10) with $\Delta k \rightarrow \Delta k_Q$ and $d_{eff} \rightarrow d_Q$.

If we write the complex-field amplitudes E_j , $j = 1, 2, 3$ in terms of real amplitudes ρ_j and phases ϕ_j according to $E_j = (\omega_j/n_j)^{1/2} \rho_j \exp(i\phi_j)$ Eqs. (3.15–3.17)

become (neglecting GVD, GVM, and loss)

$$\frac{d\rho_1}{d\zeta} = -\kappa\rho_2\rho_3 \sin(\theta), \quad (3.18)$$

$$\frac{d\rho_2}{d\zeta} = -\kappa\rho_1\rho_3 \sin(\theta), \quad (3.19)$$

$$\frac{d\rho_3}{d\zeta} = \kappa\rho_1\rho_2 \sin(\theta), \quad (3.20)$$

$$\frac{d\theta}{d\zeta} = \Delta k \left(\frac{\rho_1\rho_2}{\rho_3} - \frac{\rho_2\rho_3}{\rho_1} - \frac{\rho_1\rho_3}{\rho_2} \right), \quad (3.21)$$

where $\theta = \Delta k\zeta + \phi_3 - \phi_2 - \phi_1$ and

$$\kappa = \frac{d_{eff}}{c} \left(\frac{\omega_3\omega_2\omega_1}{n_3n_2n_1} \right)^{1/2} \quad (3.22)$$

Solutions to Eqs. (3.18–3.21) can be expressed in terms of Jacobi-elliptic functions [33, 91] and Manley-Rowe constants. In the work that follows, the notation and properties of elliptic integrals and Jacobi-elliptic functions are taken from *Handbook of Mathematical Functions*. [92]

3.2.3 OPO solutions to simplified coupled-wave equations

To this point in this chapter we have been general and the analysis can refer to any three-wave mixing process. Now we become more specific, looking at an optical parametric process and developing solutions to the simplified coupled wave equations (Eqs. (3.18–3.21)) with $3 \rightarrow p$, $2 \rightarrow i$, and $1 \rightarrow s$. Once again the subscripts p , i , and s refer to the pump, idler and signal waves. The Manley-Rowe constants for the OPO are

$$C_s = \rho_s^2 + \rho_p^2, \quad (3.23)$$

$$C_i = \rho_i^2 + \rho_p^2. \quad (3.24)$$

In general the solutions for the OPO equations are written in terms of a cubic equation. However, when one of the three fields in the interaction is zero at the

entrance of the crystal (as is the case for an SRO, which is of current interest to us, since we have a singly resonant cavity) this cubic equation reduces to the quadratic equation

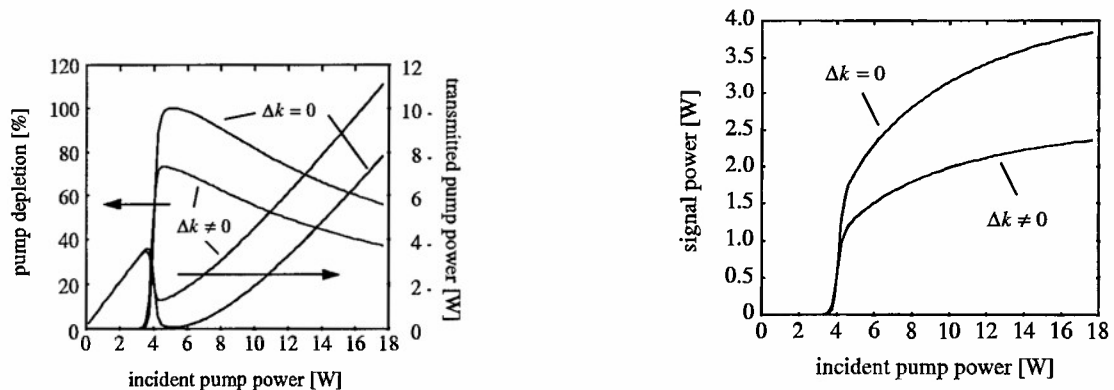
$$C(C - C_s) - \left(\frac{\Delta k}{2\kappa}\right)^2 (C - C_i) = 0. \quad (3.25)$$

Let $C = C_>$ and $C = C_<$ be the larger and smaller of the roots of Eq. (3.25). These are ordered according to $0 \leq C_< \leq C_i \leq C_s \leq C_>$ and $C_>$ is positive unless $\Delta k = 0$. The solution for the pump field is

$$\rho_p^2(\zeta) = C_< + (C_i - C_<) \text{sn}^2(Z|m), \quad (3.26)$$

where $Z = K - \sqrt{C_> - C_<} \kappa |\zeta|$, $K = K(m)$, and $m = (C_i - C_<)/(C_> - C_<)$. The function $K(m)$ is the complete elliptic integral of the first kind. [92] At the end of the crystal $\zeta = L$. The solutions for the signal and idler fields can be found from Eq. (3.26) and the Manley-Rowe constants Eqs. (3.23,3.24). Note that it is impossible to completely deplete the pump field when $\Delta k \neq 0$ and that when $\Delta k = 0$ we have $C_< = 0$, $C_> = C_s$, and $m = C_i/C_s$.

Solutions to a given system can now be calculated using an iterative process. A small amount of signal radiation which is represented physically by parametric fluorescence [93] is necessary to begin the process. This small seed signal plus the incident pump intensity are used as inputs into the crystal. The idler, signal and pump radiation out of the crystal are determined from Eq. (3.26) and the Manley-Rowe equations. After the appropriate signal loss due to outcoupling, scattering and absorption, the signal is used as a new input to the crystal for the next pass. Figure 3.1(a) shows the transmitted pump power and pump depletion versus input power for the two cases $\Delta k = 0$ and $\Delta k = 0.5$. For the case $\Delta k = 0$ there is complete pump depletion. Figure 3.1(b) plots the signal power versus average incident pump power. We plot the signal power in arbitrary units since the actual value is relatively sensitive to the outcoupling value that is chosen. All of the parameters for the two cases $\Delta k = 0$ and $\Delta k \neq 0$, except the loss, used to generate the plots were chosen



(a) Transmitted pump power and pump depletion for an OPO as a function of incident pump.

(b) Signal power as a function of incident pump power.

Figure 3.1: Plane-wave theoretical results for transmitted pump power and signal power as a function of incident pump power. Two cases are shown: $\Delta k = 0$ and $\Delta k = 0.5$. The curves are calculated for the following parameters: $1.064 \mu\text{m}$ Nd:YAG pump, modelocked at 76 MHz, producing 100 psec pulses, and focused to $120 \mu\text{m}$ waist; $1.51 \mu\text{m}$ signal wavelength; 13 mm long PPLN crystal. The loss of the system for each of the two cases was chosen independently such that the thresholds were equal and approximately the same as what is observed experimentally. The incident pump power shown is the average power.

to be equivalent to those in the actual OPO that was studied. The loss for each of the two cases was varied so that thresholds for both cases were equal and the same to what was experimentally observed. The loss needed theoretically to match the experimental results was 15% and 10% for the phasematched and non-phasematched cases respectively. These losses are higher than the estimated experimental loss of 5%. As expected, for equal losses we found that the threshold for the case with phase mismatch is greater than when there is perfect phasematching.

3.2.4 Self consistent OPO solutions to complete coupled plane Wave Equations

It is also possible to obtain self-consistent pulsed solutions for Eqs. (3.15–3.17) which take into account GVD and GVM for a synchronously pumped system. The theory has been presented by Cheung [41] and here we briefly outline their analysis. Repetitively pulsed laser systems are governed by the equation [94–96]

$$\left[G(t) - L_l(t) + \delta T \frac{d}{dt} + \frac{1}{\omega_c^2} \frac{d^2}{dt^2} \right] E_1(t) = 0 \quad (3.27)$$

which describes the intensity profile of the pulses in the steady state. For the OPO, $E_1(t)$ is the intracavity signal pulse. $G(t)$ and $L_l(t)$ represent the total round-trip field gain and loss respectively. The cavity-detuning time is given by, $\delta T = T - T_R$ where T is the repetition time period of pump pulses and T_R is the round-trip propagation time of the signal radiation in the cavity. The cavity bandwidth is ω_c and is determined by frequency dependent components of the cavity.

Cheung takes the loss L_l to be $L_l = \alpha L_c - \ln \sqrt{R}$ with R the total reflectance of the cavity mirrors, L_c the total cavity length, and α the distributed cavity loss due to other losses in the cavity such as scattering and absorption. The gain $G(t)$ is approximated by expanding in the longitudinal spatial coordinate the exact solution of Eq. (3.18) for the signal. This approximation requires that the change in the signal through the gain process is small, which is usually well satisfied when the OPO is operating at steady state. This expansion provides a temporally dependent gain coefficient which includes the following effects: dominant gain, effect of pump depletion on gain, phase mismatch reduction of the gain and the evolution of the phase difference θ on the gain.

To include the effects of GVM the parameters δT_{jk} in Eqs. (3.15,3.16) are treated as perturbations to the exact solutions and appropriate expansions are made to determine the effect of this mismatch. This introduces two effects, one which is due to the fact that the pump and signal pulses see different round-trip cavity times

due to GVM. The second effect describes the effect on gain due to the signal pulse's temporal walk through the pump pulse.

GVD effects cause the pulses to temporally broaden or shorten as they travel through the nonlinear crystal. GVD effects are treated as perturbations similar to the GVM effects. Dispersion of the pump and idler is neglected, since it affects the signal pulse only through higher-order effects on the signal. Cheung finds that GVD introduces one more term into the gain which only modifies the phase of the signal pulse.

Thus, Cheung was able to write for Eq. (3.27) for an OPO

$$\left[g(t) - L_i - S(t) + \frac{\pi^2}{3\Delta\omega_n^2} a I_p(t) \frac{d^2}{dt^2} + \frac{1}{\omega_c^2} \frac{d^2}{dt^2} - i D_1 L_i \frac{d^2}{dt^2} - \delta T_n(t) \frac{d}{dt} - 2\delta T_{13} \frac{d}{dt} + \delta T \frac{d}{dt} \right] E_1(t) = 0 \quad (3.28)$$

where a is a nonlinear parametric coefficient given by

$$a = \frac{16\pi^3 \omega_s^2 \omega_i^2 \omega_p}{k_s k_i k_p c^6} d_{eff}^2 L^2, \quad (3.29)$$

$\delta T_n(t)$ is a time-varying dephasing time shift

$$\delta T_n(t) = \frac{2\pi}{3\Delta\omega_n} a I_p(t) \left\{ 1 - \frac{2}{5} \left[2a I_p(t) + \frac{\omega_p}{\omega_s} a I_1(t) \right] \right\} + \frac{2}{3} a I_p(t) \delta T_{13}, \quad (3.30)$$

$g(t)$ is the primary gain process,

$$g(t) = a I_p(t) + \frac{2}{3} a^2 I_p^2(t), \quad (3.31)$$

and $S(t)$ describes the effect of gain saturation due to the depletion of the pump pulse,

$$S(t) = \frac{2a^2 \omega_p}{3\omega_s} I_p(t) I_1(t). \quad (3.32)$$

Results presented in this thesis are found by solving Eq. (3.34) below numerically using a finite difference method. For the pump source we use a Gaussian pulse shape

$$I_p(t) = I_{p0} \exp\left(-4\ln 2 \frac{t^2}{\delta t_p^2}\right). \quad (3.33)$$

In order to perform the numerical calculations it is useful to use normalized variables for the intensity, time, and frequency parameters to $I_o = 1/a$, $T_o = \delta t_p$, and $\Omega_o = 1/\delta t_p$ respectively. Normalized parameters are written with a caret ($\hat{}$). Then Eq. (3.28) becomes

$$\left[\hat{I}_p(\hat{t}) + \frac{2}{3} \hat{I}_p^2(\hat{t}) - L_l - \frac{2\hat{\omega}_p}{3\hat{\omega}_s} \hat{I}_p(\hat{t}) \hat{I}_1(\hat{t}) + \frac{\pi^2}{3\Delta\hat{\omega}_n^2} \hat{I}_p(\hat{t}) \frac{d^2}{d\hat{t}^2} + \frac{1}{\hat{\omega}_c^2} \frac{d^2}{d\hat{t}^2} - \delta\hat{T}_n(\hat{t}) \frac{d}{d\hat{t}} + \delta\hat{T}_{eff} \frac{d}{d\hat{t}} \right] \hat{E}_1(\hat{t}) = 0. \quad (3.34)$$

Here $\delta\hat{T}_{eff} = -2\delta\hat{T}_{13} + \delta\hat{T}$.

The output signal, idler and pump pulses are given by

$$I_s(t) = (1 - R_o) I_1(t) \quad (3.35)$$

$$I_i(t) = 2 \frac{\omega_i}{\omega_s} a I_p(t) I_s(t) \left\{ 1 + \frac{2}{3} \left[a I_p(t) - \frac{\omega_p}{\omega_s} a I_s(t) \right] \right\} \quad (3.36)$$

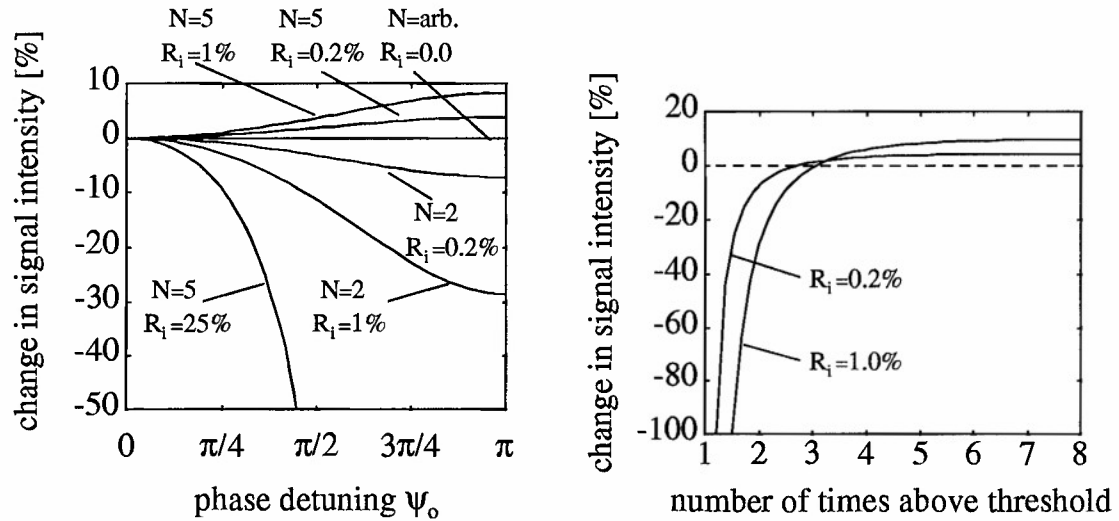
$$I_{xp}(t) = I_p(t) - \frac{\omega_p}{\omega_i} I_i(t) \quad (3.37)$$

In Eq. (3.35) R_o is the reflectance of the outcoupler for the cavity.

As a final note for completeness we should mention that Cheung has also published a theory based on this self-consistent approach for Gaussian beams. [42] The theory thus includes the effects of diffraction and walk-off in the nonlinear interaction. It does not provide solutions for the transverse spatial profiles of the beams. The OPO we operate here is loosely focused such that the Rayleigh range to the crystal length is ~ 6 . With this type of focusing and with no walk-off since the interaction is non-critically phasematched, the differences between the Gaussian beam theory and the plane-wave theory are not large. In other words the effects of diffraction are small for a loosely focused system and the use of the plane-wave theory is sufficient.

3.3 Amplitude fluctuations of singly and doubly resonant OPO's

There is a need to understand power characteristics of doubly and singly resonant OPOs and the underlying dominant physical reasons for these characteristics. We have seen amplitude fluctuations and we want to determine if these instabilities are due to doubly resonant problems. The doubly to singly resonant transition has been studied in detail by Yang *et al* [22]. Here we review their theoretical analysis of the amplitude stability of OPOs.



(a) Change in signal amplitude for an OPO as a function of phase detuning for several values of R_i .

(b) Maximum change in signal output as a function of number of times above threshold for several values of R_i .

Figure 3.2: Amplitude stability of an OPO due to doubly resonant effects.

Yang *et al.* start with Eqs. (3.10–3.12) and neglect the loss GVM and GVD terms. In their analysis they assume that the cavity is high Q at the signal and thus the signal field is spatially invariant. By assuming a constant signal field the three coupled equations are reduced to two coupled equations which leads to approximate

analytical solutions for the pump and idler fields. By using the pump and idler field solutions, they then plug these into the signal-field derivative and integrate over crystal length L . Finally, self-consistency is imposed on the signal field leading to a self-consistency equation (Eq. (6) in reference [22]). The real part of this equation is used to determine the intracavity signal-field intensity. The corresponding round-trip signal phase shift is found from the imaginary part of the self-consistency equation.

It is of interest to plot the normalized signal intensity as a function of phase detuning, idler reflectance and number of times above threshold. Phase detuning has been parameterized by Falk [97] as

$$\Psi_s + \Psi_i = \Psi_o + \Delta kL, \quad (3.38)$$

$$\Psi_o = -\frac{\omega_p}{c}[n_p L + (L_c - L)], \quad (3.39)$$

for a ring cavity. Here L is the length of the cavity, n_p is the crystal index of refraction for the pump wave, and L_c is the length of the crystal. The round-trip phase shifts for the signal and idler are given by Ψ_s and Ψ_i respectively. Different values of the phase detuning between 0 and π are plugged into the self-consistency equation (Eq. (6) in reference [22]), together with given values of the signal reflectance R_s , idler reflectances R_i , and the number of times above threshold N with which the OPO is pumped. The real part of the self-consistency equation is calculated and is related to the intracavity signal intensity. The results are plotted in Fig. 3.2.

From Fig. 3.2(a) we see that for a 8% change in the signal amplitude of the OPO, approximately one percent idler reflectance is needed when pumping five times above threshold. If pumping only 2 times above threshold the change is -28%. If the idler reflectance is zero, the output of the OPO is constant for phase detuning. For $R_i = 25\%$ the curve intersects the x -axis at 0.52π radians. Physically this means the OPO can not oscillate when $\psi_o \geq 0.52\pi$ radians. The percent change is negative for small N due to less efficient nonlinear conversion due to phase mismatch. It is negative for smaller N compared to larger N because of back-conversion effects of

the pump wave. At higher N values there is more back-conversion of the pump, and hence less signal, when $\psi_o = 0$ as compared to when $\psi_o = \pi$ radians.

Figure 3.2(b) plots the maximum signal amplitude change as a function of the number of times above the pumping threshold for two different idler reflectances. The change in signal intensity is normalized to the signal intensity when $\psi_o = 0$. As just stated, for strong pumping the signal output increases for increasing ψ_o because back-conversion of the pump is mitigated. The change in signal intensity goes to -100% for values of N greater than one. (In other words the OPO stops oscillating for values of $\psi_o < \pi$ radians.) This is clearly seen in Fig. 3.1(a) where the OPO stops oscillating for $\psi_o \geq 0.52\pi$ radians when $R_i = 25\%$ and $N = 5$. For pumping values up to about 8 times threshold we see that the change in signal intensity reaches a steady-state value for small idler reflectance. Finally we should note that as the idler reflectance increases, the actual threshold pump irradiance decreases. The threshold for a DRO can be as much as 100 times lower than a SRO [21]. Thus it is not surprising that the first OPO was a doubly resonant device demonstrated in 1965 [23]. It was not until 1969 that the first SRO was operated [98].

3.4 OPO cavity design and OPO characterization

Given the nonlinear crystal and incident pump source to be used for the OPO, we are then free to optimize the cavity and pumping geometries for best operation. In addition to this we are able to calculate various bandwidths as discussed in Chap. 2. The bandwidth characteristics provide operating requirements for the OPO. The crystal was a 15 mm×20 mm×500 μm piece of PPLN with a room temperature grating period of 29.75 μm . The poled region was 13 mm, leaving 1 mm of unpoled crystal between the poled region and the exit and entrance faces of the crystal. The pump laser is a commercial mode-locked Nd:YAG producing up to 18.0 W of 1.064 μm radiation. The repetition rate is 76 MHz and the pulsewidth is 100 psec. With this pump

and grating period, the signal and idler radiation is near 1.5 and 3.5 μm respectively when the OPO crystal is near room temperature.

First we examine the ideal pumping geometry. Considerable effort has been given to determining the optimum Gaussian pump beam that will transfer the greatest amount of power to the idler and signal beams for second harmonic generation [99,100] and parametric generation. [101,102] In a paper by Boyd and Kleinman [102] the optimum geometry for the focusing of the pump was characterized by a focusing parameter

$$\zeta = L/b \quad (3.40)$$

where b is the confocal length of the pump beam

$$b = \frac{2\pi\omega_p^2}{\lambda_p}. \quad (3.41)$$

They found that the optimum focusing parameter is 2.84 when there is no walk-off between the beams. We summarize in Table 3.2 the beam spot sizes at the waists w_{j0} , at the entrance face of the OPO crystal w_{jc1} (assuming the waist to be at the center of the OPO crystal, and at an output mirror placed 34 cm from the waist for several focusing parameters. Here $j = p, s$ or i indicates the pump signal, and idler beams respectively. Also shown is the spot size at the exit face of the DFM crystal (assuming the waist to be between the OPO and DFM crystals). Since the OPO is singly resonant for the signal wave, its spatial mode can be controlled. In these calculations we take the confocal parameter of the signal wave to be equal to that of the pump wave and calculate the corresponding signal waist size. On the other hand the idler is a free wave and its mode will be dictated by an interplay of the driving polarization wave. If the interacting beams are Gaussians the idler polarization wave is thus dictated by,

$$\exp\left(-\frac{r^2}{w_i^2}\right) = \exp\left(-\frac{r^2}{w_s^2}\right) \exp\left(-\frac{r^2}{w_p^2}\right) \quad (3.42)$$

Thus, we calculate the waist size of the idler wave for two cases. In one case the idler waist is calculated assuming that the pump, signal and idler waves have the same confocal parameter, $b_i = b_s = b_p$ and in the second case the idler waist size is calculated assuming that the idler waist will have the same size as the driving polarization wave and thus $b_i \neq b_s = b_p$. The idler waist for the second case, $b_i \neq b_s = b_p$, is deduced from Eq. (3.42),

$$w_{io} = \sqrt{\frac{w_{so}^2 w_{po}^2}{w_{so}^2 + w_{po}^2}}. \quad (3.43)$$

Both cases are shown in Table 3.2 and if we consider the worst case scenario where $b_p = b_s \neq b_i$ we are then limited to focusing parameters near $\zeta = 0.175$ if we wish to avoid clipping of the idler beam at the exit face of the 0.5 mm thick DFM crystal.

ζ	Pump				Signal			
	w_{po}	w_{pc1}	w_{pc2}	w_{pm}	w_{so}	w_{sc1}	w_{sc2}	w_{sm}
5	23	115	264	5259	27	138	318	6327
2.84	30	90	200	3964	36	108	241	4769
1	50	71	128	2352	61	85	154	2830
0.5	71	80	110	1664	86	96	132	2003
0.175	120	122	130	991	145	147	157	1193

ζ	Idler $b_p = b_s = b_i$				Idler $b_p = b_s \neq b_i$			
	w_{io}	w_{ic1}	w_{ic2}	w_{im}	w_{io}	w_{ic1}	w_{ic2}	w_{im}
5	41	207	475	9457	17	474	1106	22110
2.84	54	162	360	7127	23	358	833	16664
1	90	128	230	4230	39	215	496	9888
0.5	128	143	197	2993	55	159	354	6992
0.175	216	220	234	1782	93	128	227	4138

Table 3.2: Waist sizes of interacting beams (in μm) for various focusing parameters. Here w_{jo} is the beam waist for the pump $j = p$, signal $j = s$, and the idler $j = i$. The spot size at the exit face of the OPO crystal is given by w_{jc1} and at the exit face of the DFM crystal by w_{jc2} , $j = p, s, i$. Finally the spot size of the beams at a cavity mirror placed 0.35 m from the waists is given by w_{jm} .

Boyd and Kleinman [102] determined the optimum focusing parameter assuming that the confocal parameters of the pump, idler and signal beams were equal.

This is possible because they examined a DRO where both the signal and idler beams can be controlled by the resonator. In a later theoretical paper it was found that for an SRO the confocal parameters, and hence focusing parameters for the pump and signal beams, should not be equal for lowest threshold. [103] For example if $\zeta_p = 1$, then it is optimal to have $\zeta_s = 1.8$. This difference becomes even larger for looser focusing. With $\zeta_p = 0.1$ they predict that ζ_s should be 0.5.

Finally it is important to operate the OPO well below damage threshold. There are two types of damage to be concerned with: surface damage and self-focusing damage. The surface damage threshold has been measured and it was found that constant fluences of less than 2.7 J/cm^2 should be maintained. [75] Thus we can now estimate the minimum spot sizes of the signal and pump at the entrance face of the crystal. In order to do this we need to have an estimate of the intracavity signal intensity. If we take 80% pump depletion we know from the Manley-Rowe equations that a fraction of the incident pump equal to $0.8\omega_p/\omega_s$ goes into the signal. If we then assume a 1% signal outcoupling, we have an intracavity signal intensity that is 56 times greater than the incident pump (assuming the same spot size). Thus the minimum spot size for the signal is the limiting design parameter and must be $> 16 \mu\text{m}$. If we wish to be at least 10 times below threshold this becomes $52 \mu\text{m}$ and the minimum signal waist should be no smaller than this length. Referring to Table 3.2, we note that the signal waist is smaller than $52 \mu\text{m}$ for $\zeta > 1$. Since we are limited to focusing parameters with $\zeta < 1$ due to clipping considerations, surface damage should not be of concern for this system.

Dispersion constant	Walk-off time (psec)
$D_s = 0.04$	$\delta T_{ps} = -1.5$
$D_i = -0.14$	$\delta T_{pi} = 0.06$
$D_p = 0.13$	N/A

Table 3.3: Walk-off times and GVD constants for OPO.

Self-focusing in a material occurs when the intensity dependent refractive index and a beam with a transverse intensity profile combine to form a positive lens. Gaussian beam self-focusing damage has been studied by Kerr [104] and small-scale self-focusing by Suydam [105,106]. Suydam found that small-scale self focusing has a damage threshold given by

$$I_d \left(\frac{\text{W}}{\text{cm}^2} \right) = \frac{\lambda_o c n}{48 \pi^2 n_2} \frac{\ln(3/\delta)}{z_f} \times 10^{-7} \quad (3.44)$$

where z_f is a focusing length. δ is a dimensionless parameter which characterizes small spatial beam perturbations in the amplitude of the incident electric field. It varies between 0 and 1, 0 indicating no perturbation. The units for the other parameters in Eq. (3.44) are CGS. Plugging in the appropriate values for lithium niobate, $z_f = 10$ mm and $\delta = 1$, we find that I_d is greater than the surface damage threshold and thus is not of concern.

Acceptance bandwidth calculations are also useful. Calculation of acceptance bandwidths was discussed in detail in Chap. 2 and the results for the OPO in this section were summarized in Table 2.2. In addition to these values, we calculate the group velocity mismatch times δT_{pj} , $j = s$ and $j = i$ and the group velocity dispersion constants D_j , $j = p, s$, and i which were introduced in Section 3.2.2 for the OPO. Since the pump pulsewidth is 100 psec, we see that the GVM for this OPO is relatively small. In addition we can calculate that the GVD terms lead to less than a tenth of a picosecond pulse broadening over the length of the crystal for the given group velocity dispersion constants and in effect can be ignored.

Finally it is useful to plot the signal wavelength which phasematches for a given signal angle ρ with respect to the pump. In Fig. 3.3 we plot the results for three different pump angles ϕ with respect to the grating period. (The crystal face and grating period are taken to be perpendicular.) The center line of the each set of three lines is the phasematched results such that $\Delta k L$ is zero. The two lines on either side of the center line are the points at which the phase mismatch $\Delta k L$ is equal to $\pm \pi$ radians. The width of the three lines in effect gives a way to visualize the spectral

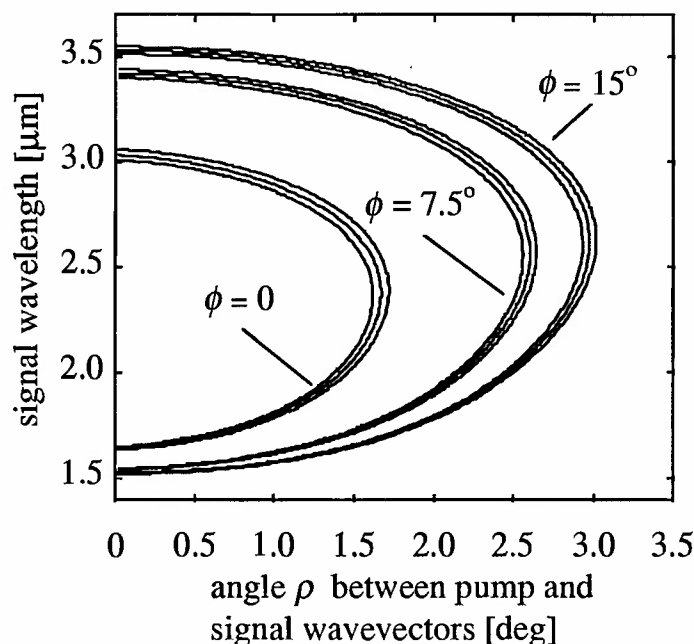


Figure 3.3: Signal wavelength versus noncollinear angle ρ . See Fig. 2.7(b) for wave vector diagram.

bandwidth of the OPO. The figure also provides a way to visualize the pump and signal angular acceptances. The rate of change in the signal wavelength as one moves along a given line is related to the signal angular acceptance. Moving vertically in the y -direction for a given signal angle ρ gives a feel for the pump acceptance bandwidth for a given angle of the signal with respect to the pump.

3.5 Experimental description

The experimental system consists of essentially three components; the pump laser, the OPO and the diagnostics. A schematic of the general experimental layout is shown in Fig. 3.4. We completely describe the system so that all relevant parameters are contained here in a single Section.

The pump source is a commercial, continuous-wave, mode-locked Nd:YAG

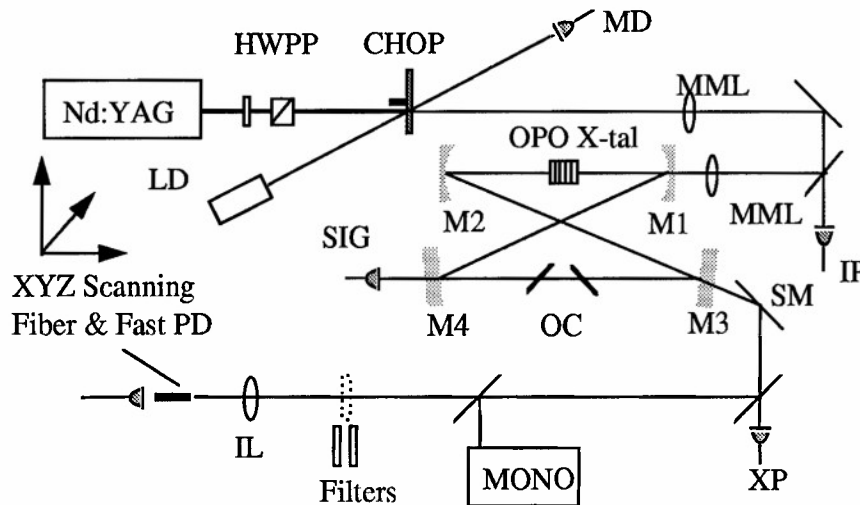


Figure 3.4: Schematic of experimental set-up for OPO.

laser operating at $1.064 \mu\text{m}$ and producing nominally 100 psec FWHM pulses in a 76 MHz pulse train with 18 W of average power. Before injection into the OPO cavity the pump laser is mechanically chopped (CHOP) at 40 Hz with a 96:1 duty cycle. The peak intensity is controlled by a halfwave plate and polarizing beamsplitter (HWPP) and monitored by a photodetector (MD). In our initial experiments, conducted at room temperature, the mechanical chopping reduces the average power of the pump laser driving the OPO to $\sim 180 \text{ mW}$, which, as discussed in Section 2.1.3, has the effect of postponing the onset of photorefraction in lithium niobate, in our case almost indefinitely. The nonlinear optical crystal is PPLN with the dimensions $15 \text{ mm} \times 20 \text{ mm} \times 0.5 \text{ mm}$ and a room temperature grating period of $29.75 \mu\text{m}$. The actual poled region is circular in shape. There is a section of the circle that has been designed so that there is a poled region 2 mm wide with a constant 13 mm length. The entrance and exit faces of the crystal are anti-reflection (AR) coated with a broadband antireflection coating and yields 98% transmission at $1.064 \mu\text{m}$ and from 97-98% for signal radiation around $1.5 \mu\text{m}$.

The cavity consists of two curved mirrors, M1 and M2, with 0.75 m radius of curvature and two flat mirrors, M3 and M4, which form a tightly folded bow-tie ring resonator. The cavity is in a vertical plane ~ 1 m long and 2.5 cm high giving an $\sim 1^\circ$ fold angle. M4 is on a translation stage to adjust the cavity for synchronization of cavity and pump pulses. The tightly folded cavity allows M4 to be scanned ± 2 mm (from the signal/pump beam overlap condition) with less than $50\text{ }\mu\text{m}$ of vertical translation of the signal beam. M1 is dielectric coated to be highly transmissive (HT) at the pump wavelength. All four mirrors are dielectric coated to be highly reflective from $1.4\text{ }\mu\text{m}$ to $1.6\text{ }\mu\text{m}$. The pump experiences Fresnel reflection from mirrors M2–M4 while the idler experiences Fresnel reflection from all of the mirrors as well as at the crystal entrance and exit faces. This gives a maximum total round-trip reflectance of $2 \times 10^{-4}\%$ for the idler. With this idler reflectance, the analysis performed in Section 3.3 indicates that the OPO should not exhibit amplitude fluctuations due to doubly resonant effects and can be considered as singly resonant at the signal radiation. The OPO cavity is designed to produce a signal waist size of $140\text{ }\mu\text{m}$ at the center of mirrors M1 and M2. The pump waist was measured to be $120\text{ }\mu\text{m}$ and is mode matched using, external to the cavity, mode matching lenses (MML). Referencing Table 3.2 we see this corresponds to a focusing parameter $\zeta = 0.175$. This value of ζ was chosen so that we would be sure to avoid any clipping of the beams on the crystal faces for OPO and/or OPO-DFM operation. A pair of intracavity glass plates mounted on rotation stages act as variable output couplers (OC). The two plates were inserted such that displacement of the signal beam due to the refraction at the glass surfaces was canceled. Changing the angle of the plates alters the Fresnel losses and thus the outcoupling experienced by the circulating signal. The output coupling can be varied smoothly from as much as 18% output coupling, when the plates are near normal incidence, to less than 0.1% at Brewster's angle. In operation the OPO's output is synchronous with the 76 MHz pulse train of the pump laser. However, since the injected pump power is mechanically chopped, operation is in the

form of bursts of synchronous pulses at 76 MHz within the chopper window. The chopper blade clears the incident pump beam in $\sim 25 \mu\text{sec}$ and the chopper window remains open for approximately $250 \mu\text{sec}$. The OPO typically reaches steady state in less than $50 \mu\text{sec}$ for incident pumping at full power, after which the output power remains constant until the chopper window closes. For lower pumping values the build-up time to steady state becomes longer. Figure 3.5 is a typical plot of the time and spatially integrated signal output of the chopped OPO as monitored by an oscilloscope for several different values of incident pumping.

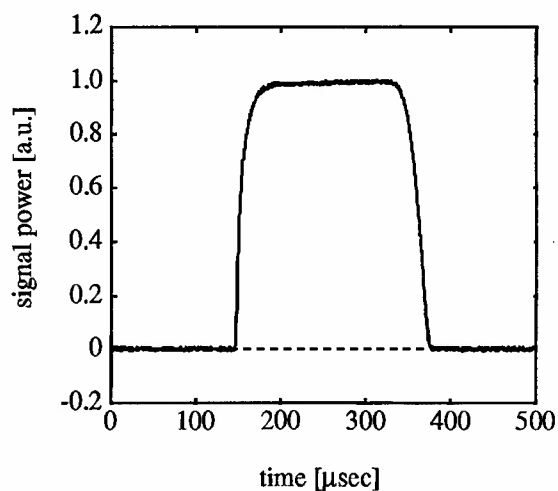


Figure 3.5: Signal output of the chopped OPO.

The rest of the system comprises the diagnostics which are designed to simultaneously monitor the averaged incident pump power, transmitted pump power and signal power, and the temporally and spatially resolved transmitted pump or signal. To monitor the averaged powers we use slow-response, large-area, photodetectors to integrate over the spatial and temporal profiles of the mode-locked pulses from the laser and OPO: The incident pump power is monitored with photodetector (IP), the signal power transmitted through high-reflectivity mirror M4 is monitored by photodetector (SIG) and the residual pump power transmitted through the PPLN

crystal, and cavity mirror M3 is picked off by a steering mirror (SM) and monitored by photodetector (XP). For spatial and temporal resolution we use a fast-response, small-area, fiber-coupled photodetector and a series of dichroic filters. The input end of the fiber is positioned in the image plane of an optical system that images the output face of the PPLN OPO crystal.

The 0.75 m concave mirror M2 and an imaging lens (IL) act as a compound optical system that images the output of the PPLN crystal to a plane where the input end of the optical fiber is scanned. The output end of the optical fiber is connected to a fast-response photodiode (PD). The dichroic filters are mounted on a motorized translation stage to allow computer controlled monitoring of signal or pump wavelengths.

A boxcar integrator, triggered by an auxiliary laser diode (LD) and photodiode (PD) is used to measure the slow large-area photodetector voltages. The integrating window is 30 μsec long and is positioned approximately 175 μsec from the opening edge of the chopper window. This is well within the steady state operation of the system. The signal from the fast-response photodiode is sent to an analog sampling head. The sampling head is triggered by the 38 MHz signal that drives the pump-laser's mode locker. The delay between the triggering and sampling of the photodiode's electrical signal is controlled by the computer through an external input of the sampling head. The temporal resolution of the sampling head binning enables us to resolve structure of the order of 25 psec. The output of the sampling head is sent to the boxcar triggered at the chopper frequency. The boxcar's integrating window's width and delay can be adjusted within the chopper window, enabling one to temporally resolve the transmitted pump and signal behavior through switch-on to steady state.

The experiment is controlled by a computer running commercial data acquisition software. The output voltages of the integrator are sent to an analog to digital converter and are recorded by the computer.

3.6 Computational and experimental results

We thoroughly examined the OPO experimentally and computationally and present the results in the following sections. Computational and experimental results are integrated in a way to produce the most complete picture possible of the operating characteristics of the OPO. We investigate cavity detuning effects, outcoupling behavior, temperature tuning and temperature effects, as well as temporal and spatial characterization of the signal and transmitted pump pulses.

3.6.1 Cavity detuning and lethargy

To obtain optimal performance from the OPO, the signal and transmitted pump powers were studied as a function of desynchronism (OPO cavity length). In Fig. 3.6 we plot the inferred signal power efficiency as a function of cavity length detuning for a series of incident average pump power P_{ip} . By inferred signal power efficiency, we mean that we take the measured signal power and scale it such that the peak is inferred from the relation,

$$\text{peak inferred signal power conversion efficiency} = \left(1 - \frac{P_{xp}}{P_{ip}}\right) \frac{\lambda_p}{\lambda_s} \quad (3.45)$$

where P_{xp} is the minimum in the average transmitted pump power which corresponds to the maximum signal efficiency. Zero on the horizontal axis has been chosen to correspond to the maximum signal efficiency and positive cavity length detuning corresponds to longer cavity lengths.

The peak pump power is varied using the half-wave plate and polarizer beam splitter (HWPP) combination between the laser and OPO resonator, while the cavity length is changed using an optically encoded motorized translation stage to change the position of M4.

There is a discrete switching behavior which is seen here off-synchronism for detunings from -300 to -100 μm . A line connects the data points which in fact indicate that there are two discrete states. We have observed up to four discrete switching

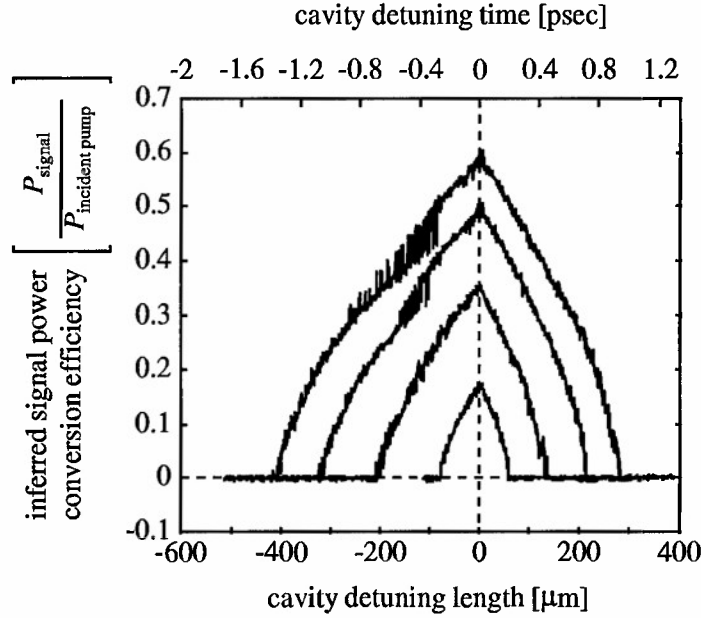


Figure 3.6: Inferred power signal efficiency as a function of cavity detuning.

states for cavity detunings up to zero. The discrete switching has not been seen for positive cavity detunings. Since the total reflectance that the idler experiences is very small, we eliminate doubly resonant effects as the source of switching. We also eliminated the possibility that switching is related to photorefractive effects, since the switching can be still be observed when the OPO crystal is heated to elevated temperatures. Finally we eliminate the possibility that the switching is due to doubly resonant effects caused by idler reflection from the crystal faces. We do this by noting that the idler pulse slips in time by almost a full pulse length after twice traversing the crystal length. Even though the reflectance of the two uncoated crystal faces (at the idler wavelength) is about 2%, the lack of overlap due to the pulse slippage leads to a very small effective reflectance. It is believed that the switching is in some way related to high gain instabilities.

Synchronism does not appear to be a function of the peak pump power or the number of times above threshold. We also observe that the cavity length detuning

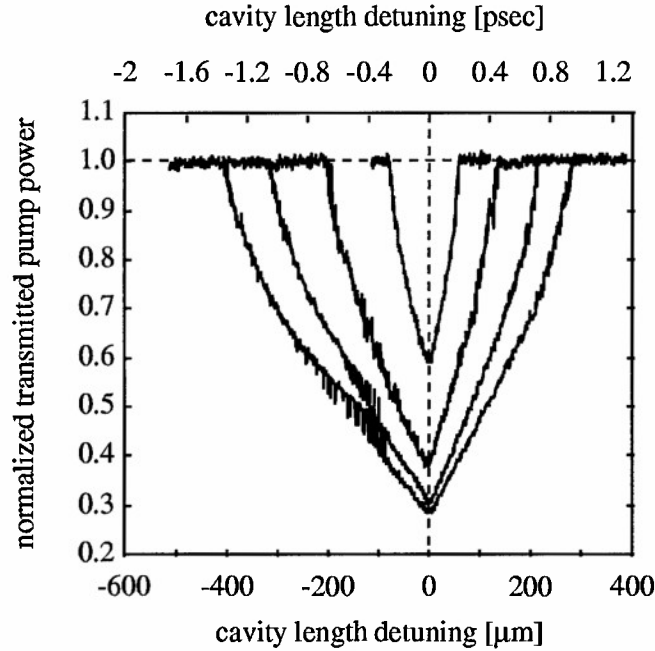


Figure 3.7: Transmitted pump power as a function of cavity detuning.

curves are not symmetric. The signal increases faster for increasing pump power on the short-cavity side of synchronism. This is a general characteristic which is always seen when operating this OPO. One possible reason for this is group velocity mismatch of the interacting waves. The pump pulse experiences a lower group index than the signal and thus moves through the crystal faster than the signal pulse. Thus, if the cavity is on the short side of synchronism so that the signal pulse arrives at the entrance face of the crystal before the pump pulse, there is a longer interaction time for the pulses. In other words, temporal walk-off takes longer for shorter cavity lengths. For the system studied here the walk-off between all three waves is near one psec (see Table 3.3), which is only about 1/100 of a pulsewidth. Thus, group velocity mismatch effects probably can't fully explain the asymmetry.

Another possible reason for the asymmetry is a phenomenon called laser lethargy which was first discovered in calculations involving conventional swept-gain ampli-

fiers. [107–110] Laser lethargy is, in effect, a slowing down of the amplified pulse. The pump pulse causes a “gain window” to be formed in the nonlinear crystal. The gain window will have a delay before it starts emitting coherently with respect to the time when the pump pulse first arrives. The result of this delay is that radiation is added to the later part of the signal pulse, in effect slowing down the signal pulse. Since the signal is slowed down, shorter cavity lengths will see more gain as compared to longer cavity lengths and lead to a detuning asymmetry skewed towards shorter cavity lengths. Since the gain medium for the nonlinear interaction is nearly instantaneous, we do not expect that this plays a strong role in the asymmetry.

In Fig. 3.7 we plot the transmitted pump power for the same conditions as Fig. 3.6. We normalize the transmitted pump by the incident pump power. From these curves it is evident that the system achieves about 73% pump depletion at the largest average pump power, integrated over the temporal and spatial profile of the transmitted pump.

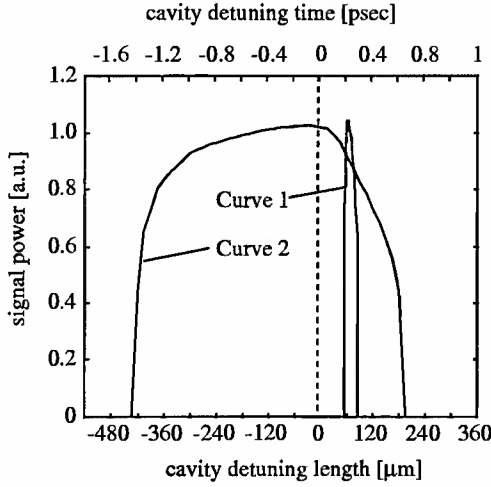
Figure 3.8 shows theoretical curves for the signal and transmitted pump. The curves were generated using Eqs. (3.28,3.35,3.37) to determine the pulse shape and then numerically integrating. The parameter values used when solving for the pulse shape for each of the two curves are given in Table 3.4. The OPO loss for the model was chosen to agree with the experimentally determined value. The peak pump power for the model was set equal to the maximum available from the Nd:YAG laser. All other parameters for Curve 1 match calculated values for the OPO. Curve 2 parameters are the same as Curve 1 except for the crystal-bandwidth. The zero on the x -axis is chosen to be the point at which maximum signal power is achieved, just as in the figures with experimental data. Agreement for the detuning range is improved when the crystal bandwidth is made smaller by a factor of 20. Interestingly we do expect some gain narrowing due to multiple passes of the crystal. [75] The detuning range is expected to increase for smaller crystal bandwidths. [41] The reason is that for smaller bandwidths, energy can be coupled from the peak of the signal pulse to

the tails and this leads to an increase in the net time over which the signal pulse experiences gain. Curve 2 exhibits the same asymmetry in cavity detuning as seen experimentally. The asymmetry in the theoretical curve is due to the term $\delta T_n(t) d/dt$ in Eq. (3.28) where $\delta T_n(t)$ is given by Eq. (3.30). This is the crystal-bandwidth dephasing term. Physically, through the crystal-bandwidth dephasing term, phase mismatch has opposite effects during the rising and falling edges of the pump pulse on the evolution of the net phase difference, θ as the pulses travel through the crystal. This leads to an asymmetry since the leading edge of the signal pulse is favored. Equation (3.30) indicates the asymmetry will increase with increasing incident pump power and this effect is observed in Figs. 3.6 and 3.7. The theoretical pump depletion in Fig. 3.8 is not as great as that seen experimentally. Once again, the reason is that the theoretical calculations exhibit more back-conversion of the incident pump than is observed experimentally. This becomes clear when we examine the temporal shape of the experimental and calculated transmitted pump pulses in Section 3.6.4 below.

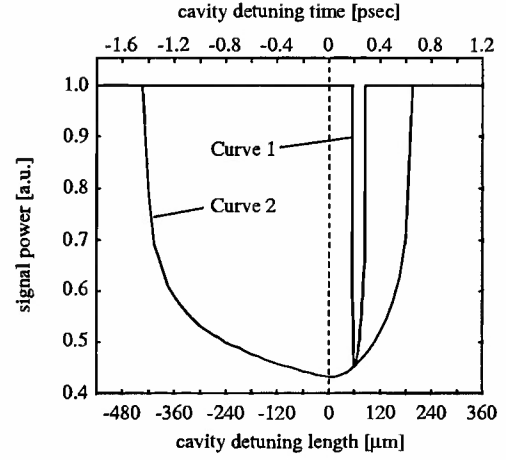
Description	Label	Curve 1	Curve 2
Cavity bandwidth	$\Delta\hat{\omega}_n$	3175	3175
Crystal bandwidth	$\Delta\hat{\omega}_c$	410	20
Loss	L_l	0.014	0.014
Incident pump amplitude	\hat{I}_p	$5L$	$5L$
Group-velocity dispersion constant	D_s	0.122	0.122
Group-velocity walk-off	$\delta\hat{T}_{sp}$	-0.0146	-0.0146

Table 3.4: Parameter values used in generating theoretical detuning curves in Fig. 3.8. Here Curve 1 matches estimated experimental parameters.

In Fig. 3.9, we plot the experimental and theoretical curves for transmitted pump and signal power as a function of incident pump power when the cavity is positioned on synchronism. The two signal power curves are scaled so that they have equal powers at two times above threshold. This point was selected since the transmitted pump powers are equal at this incident pump power. The theoretical curves “bend-back” much sooner and more sharply than the experimental curves. The reason



(a) Theoretical signal power as a function of cavity detuning.



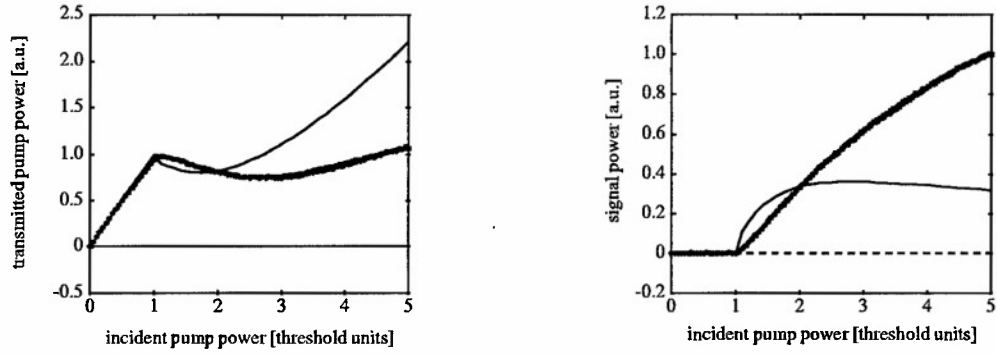
(b) Theoretical transmitted pump power as a function cavity detuning.

Figure 3.8: Theoretical curves of pump and signal power as a function of cavity detuning. All parameters for Curve 1, given in Table 3.4, are chosen to be the same as what is experimentally observed. Curve 2 only changes the crystal bandwidth term, which has a value 20 times smaller than for Curve 1.

is that the numerically generated curves demonstrate stronger back conversion than is seen experimentally. Once again, this is more clearly demonstrated in Section 3.6.4 below.

3.6.2 Temperature effects

As mentioned earlier, it is possible to temperature tune an OPO by heating the non-linear crystal. Heating the crystal changes the refractive index of the crystal and thus changes the wavelengths of the signal and idler at which phasematching occurs. This change in refractive index with temperature is modeled by experimentally determined Sellmeier relations. [65] For PPLN, in addition to the change in refractive indices there is also a change in the grating period due to crystal expansion with temperature. This has a small but measurable contribution to the tuning curve. We find that experimental results of temperature tuning the OPO agree well with the



(a) Transmitted pump power as a function of incident pump power.

(b) Signal power as a function of incident pump power.

Figure 3.9: Transmitted pump and signal power as a function of incident pump power. The solid curves are theoretical results from the model described in Section 3.2.4. Parameters for the generating the theoretical curves and given by Curve 2 in Table 3.4.

calculated values as shown in Fig. 3.10. The solid curve was calculated using the appropriate Sellmeier [65] and thermal expansion [111] relations.

We also found that heating the crystal changed the cavity length at which synchronism was found. The cavity length required for synchronism was shortened as the temperature of the crystal was increased. The reason for this was determined to be related to the change in effective length of the cavity. Two effects come into play here. One is the change in the length of the crystal due to expansion at temperature and the second is the change in the group index γ_s for the signal. For the 15 mm OPO crystal, a change in the temperature from 55 to 185 degrees equates to an experimentally determined cavity length change of $195 \pm 10 \mu\text{m}$. This agrees well with the calculated value of $185 \mu\text{m}$. To calculate the cavity length change we use Eq. (2.6) with $\alpha = 1.54 \times 10^{-4}$, $\beta = 5.3 \times 10^{-9}$, and $T_R = 25^\circ \text{C}$ [111] to determine the crystal length change and the relation

$$\gamma_s = n \left[1 - \frac{\lambda_s^2}{n_e^2} \frac{d(n_e^2)}{d(\lambda)} \right]_{\lambda_s} \quad (3.46)$$

for the group index for the signal γ_s at 20 and 180 degrees Celsius. The index

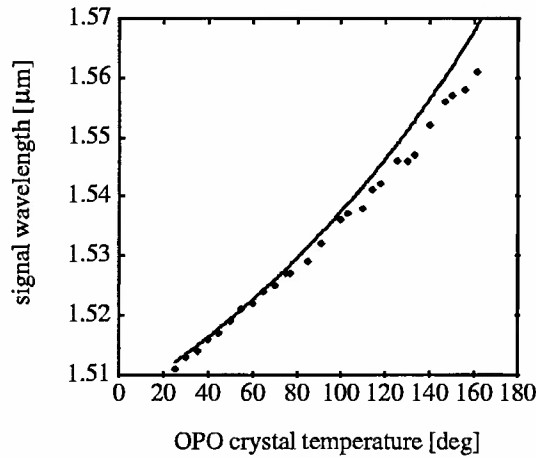


Figure 3.10: OPO signal wavelength as a function of crystal temperature.

$n = c/\nu$ (ν is the free-space signal frequency) and extraordinary index n_e are functions of wavelength and temperature. The extraordinary [65] index is determined by a Sellmeier relation. Eq. (3.46) is the specific application of equation (61) in reference [40] for a wave traveling as a purely extraordinary wave ($\theta = 90^\circ$).

Finally when operating at elevated temperatures, we found it was necessary to baffle the crystal oven from the cavity beams with a thin sheet (1 mm) of copper to prevent perturbations due to convective temperature effects. Figure 3.11 demonstrates this by plotting the signal power as a function of cavity detuning for operation with and without baffling. For this data the crystal was at 60° C. Noisier operation at the elevated temperature is clearly evident.

3.6.3 Output coupling studies

To determine optimum conditions for pump-to-signal conversion we monitored the intracavity signal power as a function of output coupling. The two intracavity glass plates change the cavity loss through the angular dependence of the Fresnel loss.

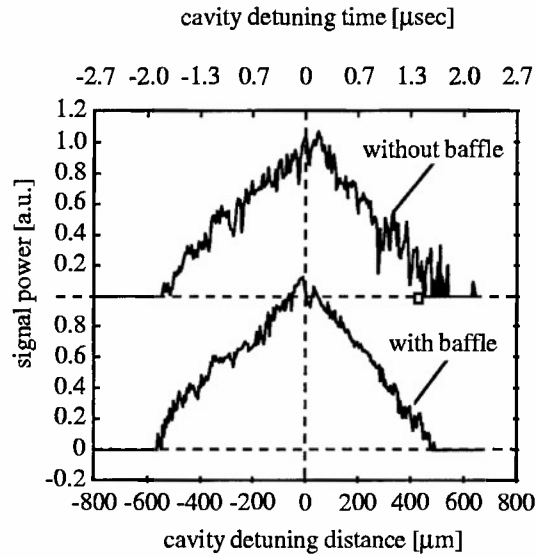


Figure 3.11: OPO signal power as a function of cavity length for operation with and without baffling. OPO crystal temperature is 60° C.

As the angle of the glass plates is adjusted, the cavity length is tuned to maintain synchronism. The output signal is plotted as a function of percentage outcoupling (top scale) and plate angle (bottom scale) in Fig. 3.12. Minimum outcoupling is 55.4°, Brewster's angle. Maximum efficiency occurs at ~3% output coupling for 18.0 W of incident pump power. The solid line is a theoretical curve generated by solving Eqs. (3.28,3.35) for the signal output pulse and temporally integrating. In generating the calculated curve the parameters for Curve 2 in Table 3.4 were used. The detuning time was selected to be the value which gave maximum pump depletion. Not unexpectedly, for smaller incident pump powers the calculated curve is shifted to smaller outcoupling values.

In addition to the outcoupling loss there are losses for the OPO due to absorption, scattering and reflectance losses at the crystal faces. It is possible to estimate these "internal" losses. At threshold we know that loss times gain must be equal to

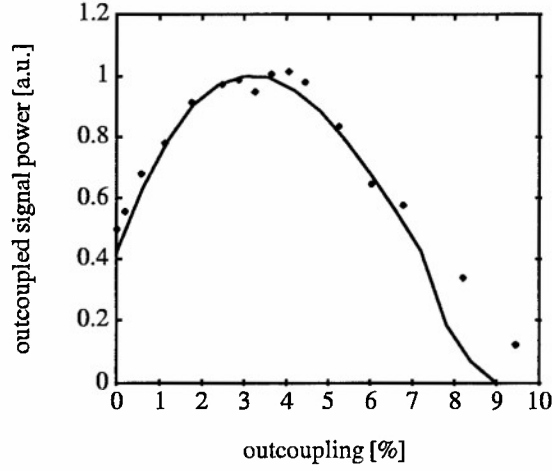


Figure 3.12: Signal power as a function of outcoupling loss.

one. The small-signal gain g_o and the loss L_l can be written as

$$g_o = 1 + 2\Gamma^2 L^2 \quad (3.47)$$

$$L_l = T_o R_{loss} \quad (3.48)$$

where $1 - R_{loss}$ is the internal loss (including the loss of mirrors M1–M4 which are all high reflectors at the signal wavelength) and T_o is the transmission of the Brewster flats. The gain parameter Γ^2 is given by

$$\Gamma^2 = \frac{8\pi^2 I_{th} g_s d_Q^2}{\epsilon_o c n_p n_i n_s \lambda_i \lambda_s} \quad (3.49)$$

where I_{th} is the threshold irradiance of the pump laser and g_s is a coupling factor on the order of one which is due to the failure of the driving polarizations to completely overlap the Gaussian modes of the pump and signal. [21] Performing a nonlinear fit to the equation which states gain times loss equals one, and using R_{loss} as a fitting parameter we find that the internal loss is $\sim 5 \pm 2\%$. Thus the optimum outcoupling for this OPO is $8 \pm 2\%$. This 5% loss was set into the model and the calculated curve in Fig. 3.12 is plotted versus output coupling only.

3.6.4 Temporal and spatial studies

To characterize the operation of the synchronously pumped OPO and to fully observe effects such as pump depletion and back conversion we must be able to resolve structure within the temporal and spatial envelope of a pulse. In our system this requires temporal resolution on the order of 20 psec and spatial resolution of the order of 10 μm . The effect of back-conversion is expected to be observed during strong pumping at the spatial and temporal center of the pump pulse after the system has reached steady-state operation. Thus, we require a fast detection system with high spatial resolution. Such a system is described in the experimental description section (Sec. 3.5). To observe the on-axis pump-depletion, cavity-length detuning scans were repeated using a fiber-coupled fast photodetector to monitor the spatial and temporal center of the transmitted pump. The spatial center was obtained from a two-dimensional scan of the transmitted-pump's intensity profile with the OPO off-resonance. (Spatial studies are discussed more fully in the Section 3.6.4.1.) A narrow, variable-delayed sampling window of ~ 20 psec width was set to record the peak of the spatially resolved transmitted pump signal. The results are shown in Fig. 3.13, which plots the normalized transmitted pump power as a function of cavity detuning for a fixed incident peak power of 18.0 W. Once again synchronism, zero on the horizontal axis, is defined to be the cavity length which gives the maximum pump depletion. Positive cavity length detuning corresponds to longer cavity lengths and longer cavity round-trip times for the signal pulses. For comparison the integrated photodetector measurements are included. It is clear that the peak transmitted pump depletion measured by the fast system is greater than the slow, large-area photodiode measurements. The peak on-axis pump depletion is $\sim 95\%$ at a cavity detuning of $-100 \mu\text{m}$. Pump depletion at synchronism, which is about 79%, is less than off-resonance due to back-conversion effects. The spatially and temporally resolved data is even more asymmetric than the integrated data.

The on-axis behavior, at the peak of the transmitted pump's temporal pulse

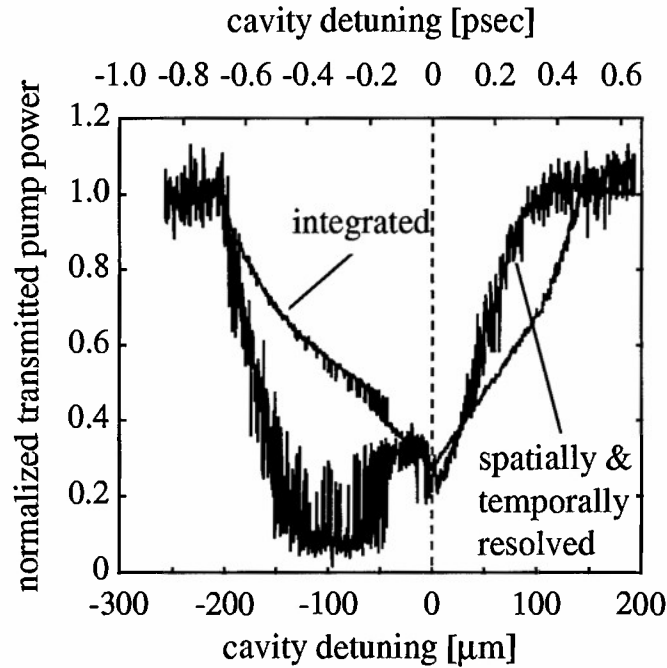
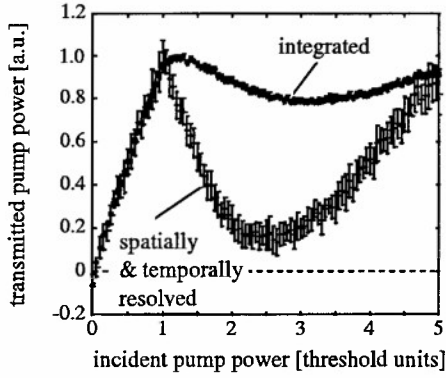
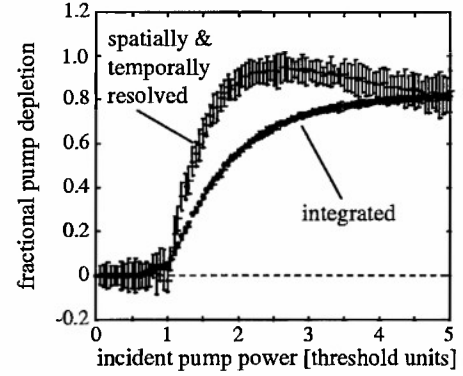


Figure 3.13: Spatially resolved peak transmitted pump power as a function of cavity detuning.

was further studied as a function of incident pump power. Again the cavity is positioned on synchronism and the fiber is in the image plane at the peak of the pump pulse with the fast detector sampling window set at the center of the pulse. Figure 3.14 shows plots of the normalized transmitted pump power and of the percentage of pump depletion, recorded on the fast detector at the spatial and temporal center of the pulse as a function of incident pump power. Also shown for comparison are the slow, large area photodetector measurements. The temporally and spatially resolved transmitted pump again shows greater on-axis pump depletion than the averaged transmitted pump. In Fig. 3.14(b) we see the peak on-axis pump depletion measured at the temporal center of the pulse is $\sim 95\%$ and occurs at approximately 2.5 times above threshold. For incident pump powers greater than twice threshold the pump depletion decreases, an effect lost in the averaged data. The reduction in percentage



(a) Transmitted pump power as a function of incident pump power.



(b) Pump depletion as a function of incident pump power.

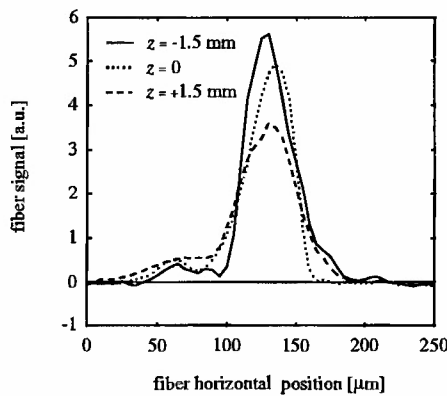
Figure 3.14: Spatially and temporally resolved peak transmitted pump power as a function of incident pump power.

pump depletion is due to back-conversion of signal power to pump power. This is also why the off-resonance cavity detuning resolved pump depletion is greater than when the cavity detuning is zero. Off-resonance the OPO threshold is higher and thus the maximum number of times above threshold with which the OPO is pumped is reduced. Experimental results show that for a cavity detuning of $-100 \mu\text{m}$ the maximum number of times above threshold achievably is 2.5. To ensure that we were measuring transmitted pump radiation ($1.064 \mu\text{m}$) and not a combination of pump and signal wavelengths, a $1.5 \mu\text{m}$ high-reflectivity mirror was positioned in the path of the input beam to the fiber. The idler is absorbed by the cavity optics, and does not escape the cavity.

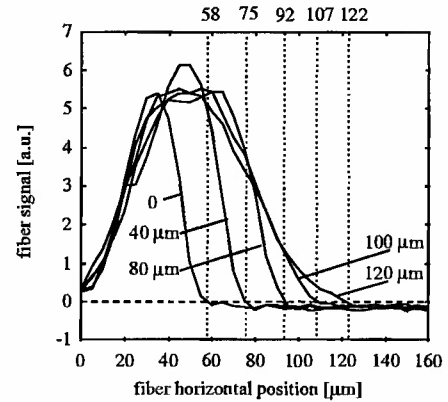
3.6.4.1 Spatial studies of pump and signal beams

To further observe pump depletion and back-conversion, the transmitted pump's spatial profile was recorded as a function of incident power. The effect of pump depletion should “eat” away at the center of the transmitted pump, producing a “volcano like” spatial profile. At high pump irradiances, the effect of back-conversion should begin to

take place at the peak of the signal pulse. For a well-aligned system, on synchronism, back-conversion would appear as an increase in pump intensity at the spatial center of the pump profile. Thus, back-conversion will be seen as an increase in transmitted pump intensity which will tend to fill in the “crater”.



(a) Image plane location determination.



(b) Magnification of imaging system.

Figure 3.15: Imaging plane location and magnification.

For greatest clarity in results, the waists of the pump and signal beams, which are spatially located together, should be imaged at the detector (here the fiber tip). The image plane of the waists was determined by placing a straight edge near the output face of the crystal. This partially blocks a weak incident pump. The fiber was translated longitudinally until the image plane was found. The image plane was judged to be the horizontal scan with the sharpest edge in the light intensity. Also, by translating the straight edge, and observing the translation of the intensity pattern in the image plane, we were able to determine the magnification of our imaging system. Typical results of the a longitudinal scan and magnification measurements are shown in Fig. 3.15. In Fig. 3.15(a) the straight edge is located on the right of the curves (larger fiber position numbers). We see that $z = 0$ has the sharpest fall in power and this is considered to be the image plane. Figure 3.15(b) shows data which indicates

that the magnification M of our system is $M = 1.9$. The numbers on the top of this graph are the x -axis zero crossing points which are used as a convenient way to determine the "edge" of the straight edge in the image plane. The numbers labeling each curve represent the position of the straight edge in the object plane. Here we have chose 0 to be the point at which approximately half the incident beam power is lost.

The spatial experimental data, shown in Fig. 3.16, does indeed show formation of a crater and a back-conversion peak. In this experiment the cavity was carefully aligned for temporal and spatial overlap between the circulating signal and pump. Again the 20 psec temporal window of the sampling head was set at the peak of the pump pulse. Measurements were collected by the scanning fiber and recorded as a function of x and y . The contour plots of are raw data and the x and y axes should be multiplied by the magnification $M = 1.9$ to determine actual spot sizes. A series of profiles was recorded starting close to threshold and increasing to maximum incident pump power. The vertical scale indicates the absolute magnitude of the transmitted pump. All plots are normalized. The threshold for OPO oscillation was $0.22I_o$, where I_o corresponds to maximum incident power of 18.0 W.

Above threshold the overall profile decreases, with maximum depletion taking place at the center of the beam -Fig. 3.16(d). Continuing past three times threshold, the overall pump profile starts to grow a narrow cone in the region where the pump has been depleted and the strongest signal exists. This central cone is due to back-conversion of the pump. The cone continues to grow with increasing incident power. Figure 3.16(h) clearly shows a narrow central cone surrounded by an annulus formed by the remainder of the incident pump that has not been down converted. The central cone is formed by the back-conversion of signal and idler into the pump wavelength. We do not show the spatial profile of the corresponding signal pulses, since at all pump powers the signal pulse is Gaussian and has the same form as in Fig. 3.16(a). Of course the peak power of the signal pulse increases with increasing incident pump

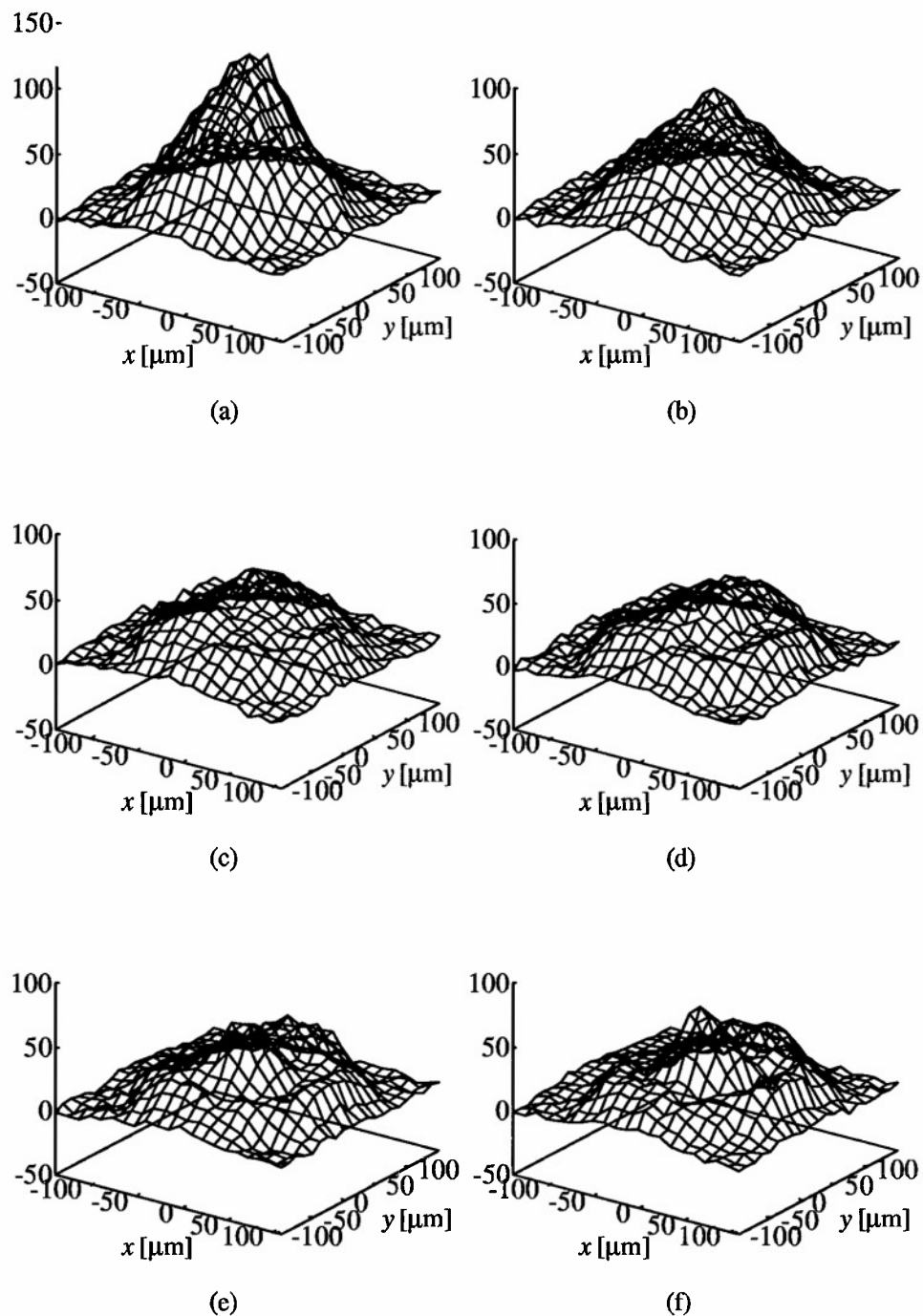


Figure 3.16: Transmitted pump spatial profiles for incident pump powers (a) 1.4, (b) 1.8, (c) 2.3, (d) 2.7, (e) 3.2, and (f) 3.6 times threshold.

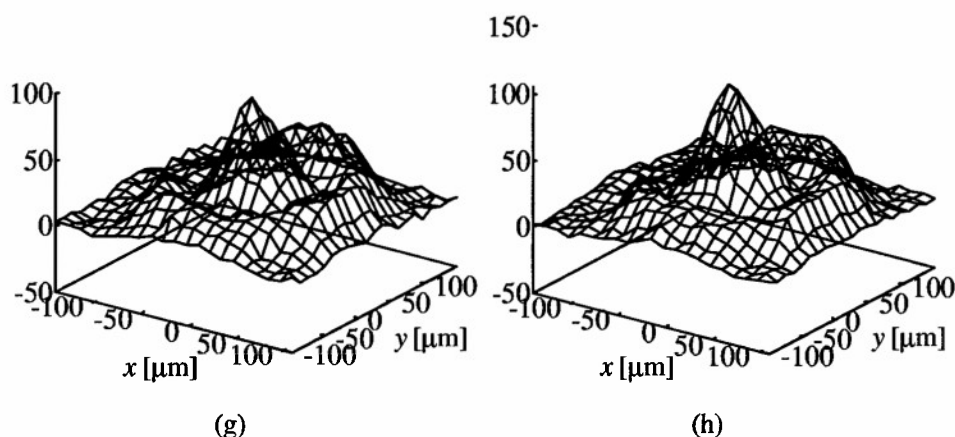


Figure 3.16 (cont.): Transmitted pump spatial profiles for incident pump powers (g) 4.1 and (h) 4.5 times threshold.

power which can be seen in Fig. 3.10.

3.6.4.2 Temporal studies

The operation of the OPO from switch-on through steady-state operation was also studied. The spatial on-axis temporal profiles of the transmitted pump pulse and signal pulse were recorded as a function of time within the chopper window. The following results show typical operation of OPO for strong pumping (18.0 W) and pump pulse of ~ 100 psec FWHM. Figure 3.17 contains plots of the measured signal and transmitted pump temporal profiles measured by integrating over a $20 \mu\text{sec}$ gate delayed at different times during the chopper window with respect to the chopper window turn-on point. The times are 50, 60, 80, 90, 110, and $125 \mu\text{sec}$ for plots a–f respectively. This series of plots represents the turn-on behavior of the OPO. Plots d–f are nominally the same. Switch-off is essentially the reverse of Fig. 3.17. This sequence shows growing pump depletion within the transmitted pump's temporal profile. There is some evidence of back-conversion as well.

We also plot the measured signal and transmitted pump temporal profiles for

six different cavity detunings in Fig. 3.18. Results are averages over 100 μsec window in center of chopper window. For cavity lengths shorter than synchronism (negative cavity detunings) we see that the signal pulse has a shorter round trip time than the pump pulse and “eats” away at the front of the pump pulse. On the other hand for cavity lengths longer than synchronism (positive cavity detunings) the signal pulse has a longer round trip time and is seen to “eat” away at the trailing edge of the pump pulse. The long tails for the trailing edges of the signal and transmitted pump pulses are an artifact of the acquisition electronics and not real. We also see from this data that the signal pulse has a full width half maximum (FWHM) value of ~ 80 psec which is somewhat less than the FWHM of the pump pulses (~ 100 psec). For comparison, in Fig. 3.19 we plot theoretical temporal profiles for the signal and transmitted pump for the cavity detunings indicated. The parameters used to generate this curve are given by Curve 2 of Table 3.4. Once again we see the general characteristics of the signal pulse either at the preceding (negative cavity detunings) or trailing (positive cavity detunings) edge of the pump pulse. Clearly shown is that the model predicts much higher back-conversion than experimental results indicate.

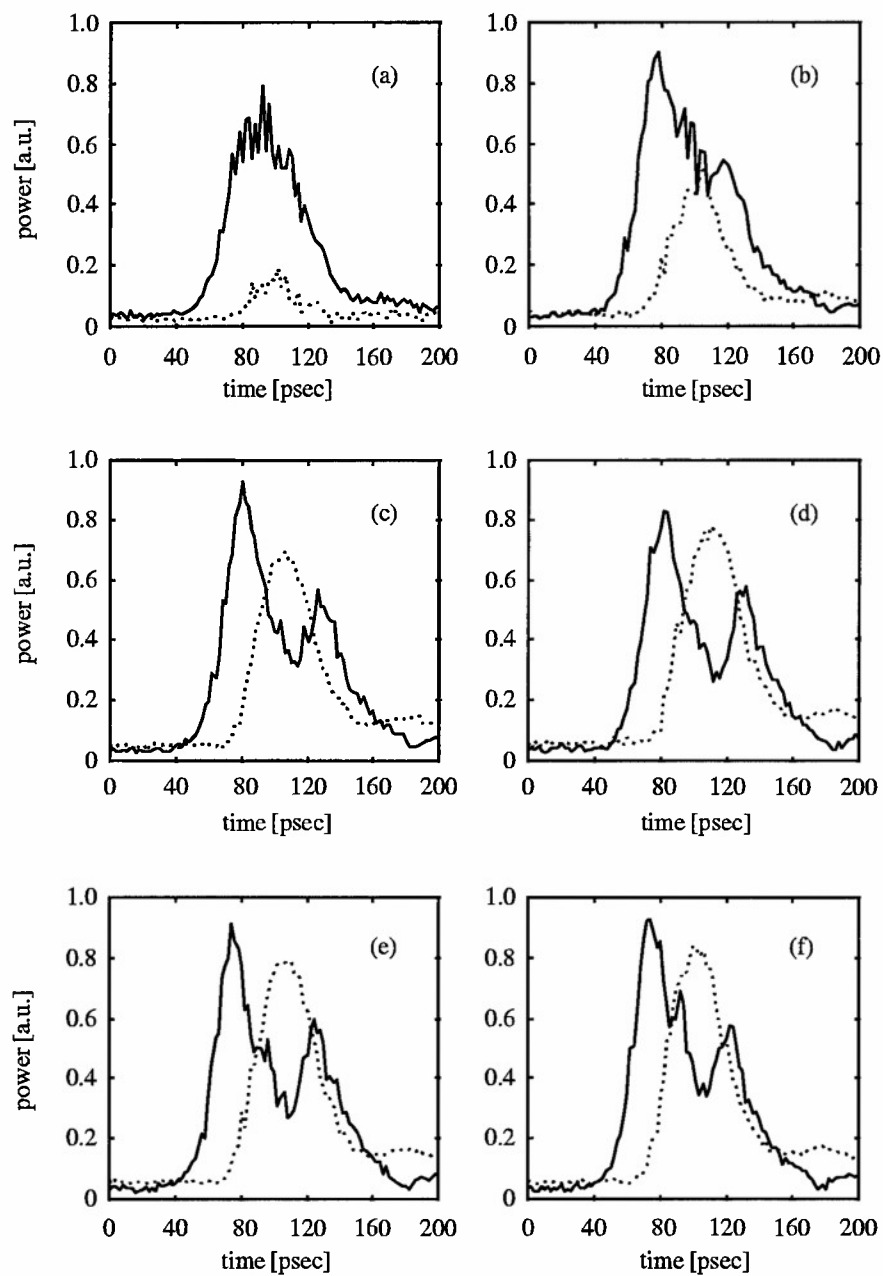


Figure 3.17: Experimental temporal characterization of pump (solid curves) and signal (dotted curves) pulses in OPO during turn-on.

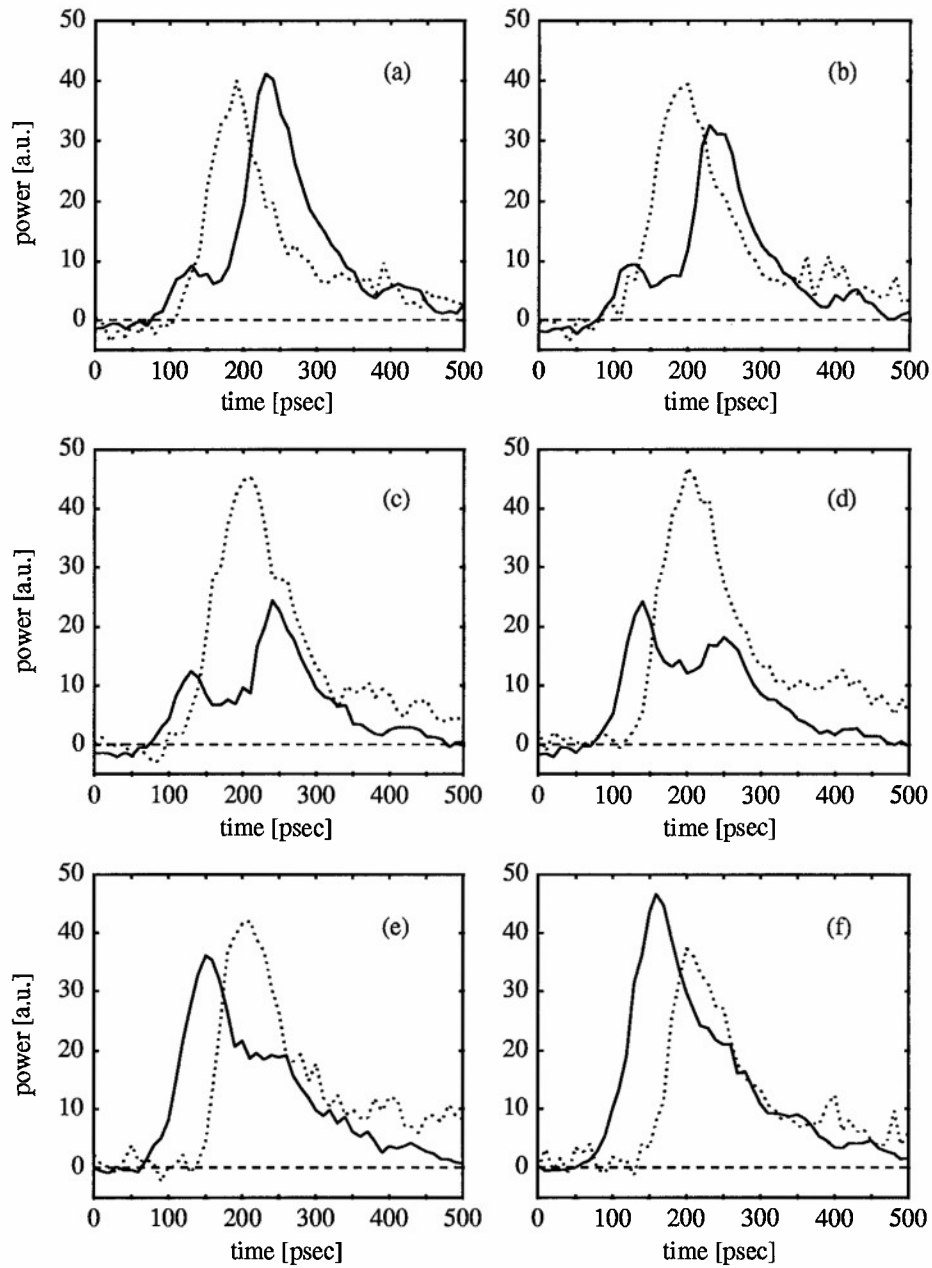


Figure 3.18: Experimental transmitted pump and signal temporal profiles for cavity detunings of (a) -0.80 psec, (b) -0.54 psec, (c) -0.27 psec, (d) on-resonance, (e) $+0.27$ psec, and (f) $+0.54$ psec. The data plotted here corresponds to results in Figs. 3.6 and 3.7

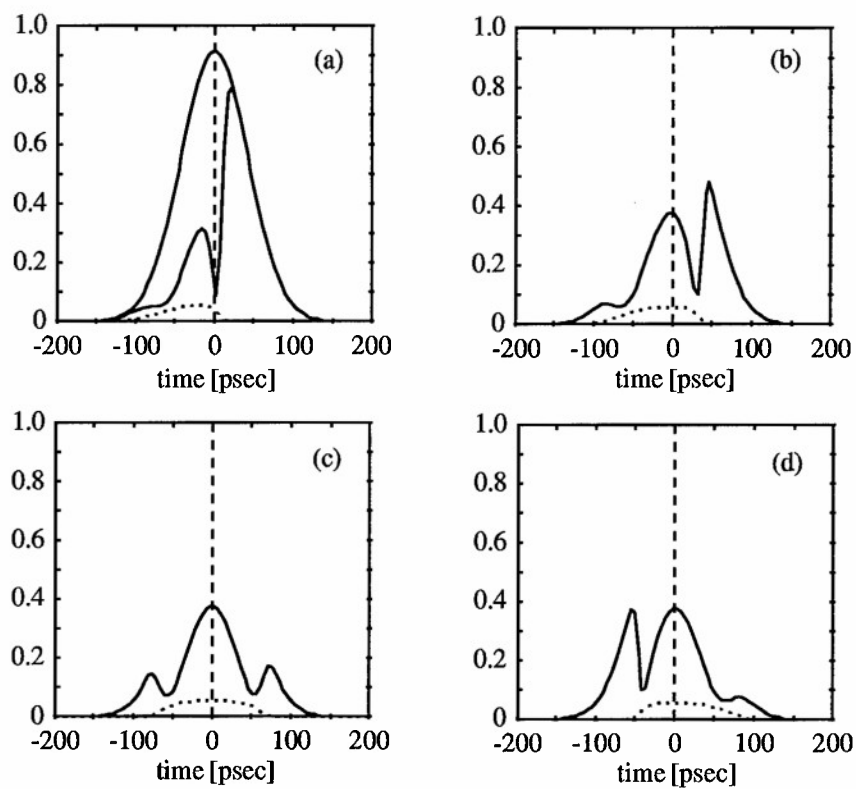


Figure 3.19: Theoretical transmitted pump (solid lines) and signal (dotted lines) pulse temporal profiles for cavity detunings of (a) -0.8 psec, (b) -0.4 psec, (c) on-resonance, and (d) +0.4 psec.

Chapter 4

Optical parametric oscillator with intracavity difference-frequency mixing

4.1 Introduction

A synchronously pumped optical parametric oscillator (OPO) has been investigated and discussed in Chap. 3. Recall that the OPO is a device for tunably downconverting light of frequency ω_p to two frequencies, the signal frequency ω_s and the idler frequency ω_i , which sum to ω_p . The equations describing the three-wave mixing process introduced in Section 3.2.2 (with $3 \rightarrow p$, $2 \rightarrow i$, and $1 \rightarrow s$) indicate that these three frequency components are symmetric with respect to the signal and idler. We use the convention that $\omega_s \geq \omega_i$ and assume the OPO is singly resonant for the signal wave. The Manley-Rowe relations for the three-wave mixing process indicate that one signal and one idler photon are generated for each pump photon that is converted. This limits the idler photon-conversion efficiency η_i — the number of idler photons out of the device divided by the number of pump photons incident on the device — to a maximum of 100% for an OPO. For the OPO discussed in Chap. 3 we found that the

maximum pump depletion was 73% and hence the maximum idler photon-conversion efficiency must be less than this, since there are losses such as absorption and scattering. Here we demonstrate a device that uses intracavity difference-frequency mixing (DFM) between the signal and idler frequencies to better this maximum performance.

Difference-frequency mixing of the signal and idler from an OPO was demonstrated in some early experiments [1–3], and recently a number of investigators have examined mixing the signal and idler waves generated from a synchronously pumped OPO to produce difference-frequency radiation [4–6]. Here the difference frequency ω_d is produced in the DFM interaction, $\omega_d = \omega_s - \omega_i$. The DFM process not only produces radiation at the difference frequency, but for each difference-frequency photon produced, an additional idler photon is produced.

We recently reported that a DFM process inside the OPO cavity resonant for the signal wave has the advantage of providing maximum energy extraction at the idler frequency [7]. Using a plane-wave model, we found that operation at high conversion efficiency occurs over a large dynamic range of incident pump intensity for proper choices of the ratio of the coupling parameters for the OPO and DFM processes. We expect this large dynamic range to improve the conversion efficiency when the pump beam is not a cw plane wave, but has transverse and/or temporal intensity variations. A high-Q cavity is used, since no linear out-coupling of the signal radiation is necessary. Thus, as opposed to extracavity DFM of the signal and idler, any unused signal radiation in the DFM process is recirculated and not lost to the system. In the ideal case where the OPO process heavily depletes the pump radiation, photon-conversion efficiencies for generation of idler and difference-frequency radiation can be close to $\eta_i = 2$ and $\eta_d = 1$, respectively. Here we report experimental results of a singly resonant OPO cavity with an intracavity crystal that mixes the signal and idler waves, enhancing the idler power conversion efficiency. We call this an OPO-DFM device.

4.2 Theory and modeling

The analysis here is aimed at singly resonant devices as in Chap. 3 for the OPO. We once again provide analytical solutions for the simplified coupled-wave equations. Also, Cheung's model [41] for the OPO, which includes GVD and GVM effects and relies on a self-consistency argument, is modified to apply for an OPO-DFM device. This model provides temporal pulse shapes of the idler, signal and transmitted pump. Comparison of the OPO-DFM models to their OPO counterparts provides a basis for understanding the role the DFM nonlinear interaction plays when taking place inside the OPO cavity.

4.2.1 OPO-DFM modeling for simplified coupled wave equations

Plane-wave analysis of three-wave mixing processes is relatively simple and usually is effective in describing the general characteristics of nonlinear devices. The OPO-DFM device has been investigated with a plane-wave analysis [7], and we review this work here. The equations for describing the OPO interaction were developed in Section 3.2.2. The equations for the DFM interaction are similar and can be obtained from Eqs. (3.15–3.17) by making the transformations $1 \rightarrow d$, $2 \rightarrow i$, and $3 \rightarrow s$. It is necessary to subscript θ , κ , Δk , and L to discriminate between the OPO and DFM interactions. We label the OPO and DFM interactions with an a and b subscript respectively. The Manley-Rowe relations are found to be

$$D_i = \rho_i^2 + \rho_s^2 \quad (4.1)$$

$$D_d = \rho_d^2 + \rho_s^2. \quad (4.2)$$

Solutions to the OPO and DFM interactions can be written in terms of Jacobi-elliptic functions. It is useful to transform to the dimensionless Manley-Rowe constants for the DFM interaction $\hat{D}_i = \kappa_b^2 L_b^2 D_i$ and $\hat{D}_d = \kappa_b^2 L_b^2 D_d$. Shown in Fig. 1.2

is a schematic of an OPO-DFM device. All of the idler and difference-frequency radiation is outcoupled after the DFM interaction. Thus the device is singly resonant and the DFM interaction is not phase sensitive. The idler and signal radiation at the entrance face of the DFM crystal z_2 are given by Eqs. (3.23–3.25) with the appropriate a subscript on Z , K and m . The solutions for the DFM interaction are given in Eqs. (4.3,4.4) below, and the Manley-Rowe relation, Eq. (4.1).

$$(\kappa_b L_b \rho_s)^2 = \hat{D}_< + (\hat{D}_d - \hat{D}_<) \text{sn}^2(Z_b | m_b) \quad (4.3)$$

$$(\kappa_b L_b \rho_d)^2 = (\hat{D}_d - \hat{D}_<) \text{cn}^2(Z_b | m_b). \quad (4.4)$$

The solution for ρ_i^2 can be derived from the Manley-Rowe equations. Here $\hat{D}_<$ and $\hat{D}_>$ are the smaller and larger roots of the quadratic equation

$$\hat{D}(\hat{D} - \hat{D}_i) - \left(\frac{\Delta k_b}{2\kappa_b} \right)^2 (\hat{D} - \hat{D}_d) = 0 \quad (4.5)$$

Note that in general solutions of the three plane-wave equations leads to an cubic equation rather than the quadratic equation written. Setting $\rho_d(z_2) = 0$ reduces it to this quadratic form. Similarly to the OPO interaction examined in Sec. 3.2.3, we have $Z_b = K_b - \sqrt{\hat{D}_> - \hat{D}_<} \kappa_b(\zeta)$, $K_b = K(m_b)$ and $m_b = (\hat{D}_d - \hat{D}_<)/(\hat{D}_> - \hat{D}_<)$. If we take Δk_a to be zero for the OPO-DFM, it is possible to completely deplete the incident pump radiation in the OPO interaction. Furthermore, for the case $\Delta k_b = 0$ we have $\hat{D}_< = 0$. At the ends of the crystals we set $Z_m = \Lambda_m$, $m = a$ or b .

In order to characterize the OPO-DFM device we start with a small seed signal at z_1 . This is physically related to the parametric fluorescence which is present at start-up [93]. The signal, idler and pump radiation coming out of the OPO crystal are calculated and used as input into the DFM interaction. The pump is unaffected in the DFM crystal, while idler and difference-frequency radiation is generated at the expense of signal radiation. The idler and pump radiation is outcoupled, while the signal radiation is again used as input into the OPO crystal (after some outcoupling loss). We continue to iterate until a steady state is reached. This typically takes less than 50 iterations. For example, Fig. 4.1 is a typical plot of the signal and

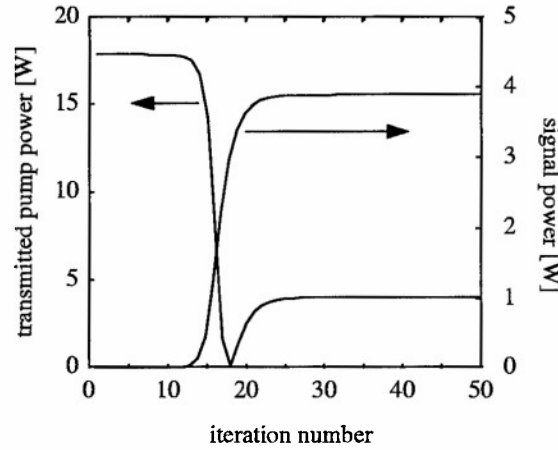


Figure 4.1: Plane wave numerical results of OPO-DFM. Plotted are signal and transmitted pump powers versus iteration number. OPO parameters for generating curve same as for $\Delta k = 0$ case in Fig. 3.1. The DFM crystal length is chosen to be 6 mm.

transmitted pump powers versus iteration number. Steady state is reached in less than 30 iterations. As the incident pump power is reduced, more iterations are necessary to reach steady state. Parameters for generating these curves are the same as in Fig. 3.1 for the case $\Delta k_a = 0$. The DFM interaction was arbitrarily chosen to have a nonlinear drive one third that of the OPO interaction and is also phasematched, $\Delta k_b = 0$.

Now we would like to operate the OPO-DFM device with complete pump depletion (CPD) which means it has 100% power conversion efficiency (assuming no parasitic losses). For CPD $\Lambda_a = -2(n_a - 1)K_a$, where n_a is a positive integer. Here we consider only the case $n_a = 1$, $\Lambda_a = 0$, which corresponds to the lowest incident pump intensity which gives CPD. Energy flows into the OPO-DFM device through the incident pump wave and out of it through undepleted pump, idler and difference-frequency radiation and loss mechanisms such as scattering and absorption. We wish to maximize the conversion of pump radiation into idler and difference-frequency radiation and thus wish to completely deplete the incident pump. Analytical solution

of CPD do exist and can be parameterized in terms of the nonlinear coupling constants g_a and g_b for the OPO and DFM interactions respectively. These coupling parameters are given by

$$g_a = \frac{d_a}{c} \left(\frac{\omega_i \omega_s \omega_p}{n_i n_s n_p} \right)^{1/2} L_a \rho_p(z_1) = \kappa_a L_a \rho_p(z_1) \quad (4.6)$$

$$g_b = \frac{d_b}{c} \left(\frac{\omega_i \omega_s \omega_d}{n_i n_s n_d} \right)^{1/2} L_b \rho_p(z_1) = \kappa_b L_b \rho_p(z_1) \quad (4.7)$$

where L_a and L_b are the lengths of the OPO and DFM crystals respectively. CPD states exist when the DFM interaction limits the signal radiation such that there is just enough signal to completely deplete the pump (no backconversion) and thus $\rho_p(z_2) = 0$. Now through the Manley-Rowe equations (Eqs. (3.23,3.24) for the OPO and Eqs. (4.3,4.4) for DFM) we can determine what sets of values (g_a, g_b) satisfy this constraint.

We use m_a as a generating parameter. Now for a singly resonant OPO where $\rho_i(z_1) = 0$ we have $C_s = \rho_s^2(z_2) = \rho_p^2(z_1)/m_a$, and the condition $\Lambda_a = 0$ becomes

$$g_a = \sqrt{m_a} K_a \quad (4.8)$$

We also have (keeping in mind that $\rho_p(z_2) = 0$) the relation

$$\rho_s^2(z_3) = \left(\frac{1 - m_a}{R m_a} \right) \rho_p^2(z_1) \quad (4.9)$$

where R represents loss at the signal. Because $\rho_s(z_3) \leq \rho_s(z_2)$ we have the condition $m_a \geq 1 - R$. Now the Manley-Rowe constants for the DFM (Eqs. (4.3,4.4)) are functions of g_b and given by $\hat{D}_d = g_b^2/m_a$ and $\hat{D}_i = (1 + 1/m_a)g_b^2$. From Eq. (4.5) we see that $\hat{D}_>$ and $\hat{D}_<$ depend on \hat{D}_d and \hat{D}_i and thus are also functions of g_b . Finally, $m_b = (\hat{D}_d - \hat{D}_<)/(\hat{D}_> - \hat{D}_<)$ and $\Lambda_b = K_b - (\hat{D}_> - \hat{D}_<)^{1/2}$ are functions of g_b as well. Evaluating Eq. (4.4) at $z = z_3$ and thus $Z_b = \Lambda_b$ we have

$$W(m_a, g_b) = \frac{1 - m_a}{R m_a} g_b^2 - \hat{D}_< - (\hat{D}_d - \hat{D}_<) \text{sn}^2(\Lambda_b | m_b). \quad (4.10)$$

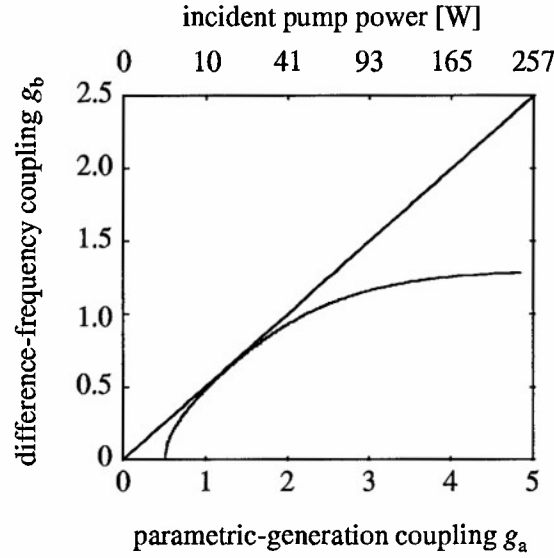
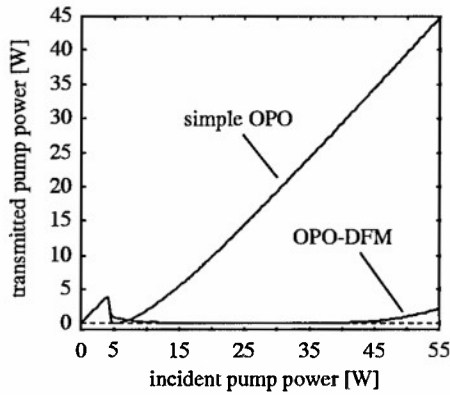
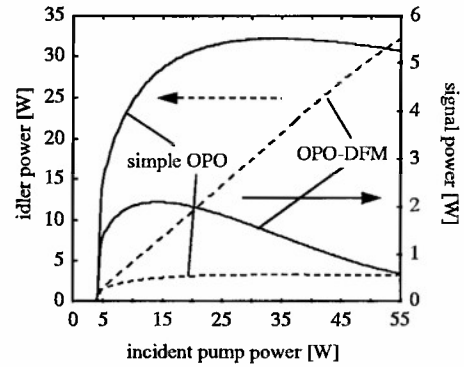


Figure 4.2: Complete pump depletion states for OPO-DFM device plotted in the (g_a, g_b) plane. The slope of the straight line, the operating line for the device, is 0.5.



(a) Transmitted pump power versus incident pump power for OPO-DFM and OPO.



(b) Idler and signal power versus incident pump power for OPO-DFM and OPO.

Figure 4.3: Plane wave numerical results for OPO and OPO-DFM devices. OPO and DFM parameters used to generate curves are chosen to match experimental parameters. The ratio of the coupling parameters for the OPO-DFM device is $g_b/g_a = 0.5$. This corresponds to a DFM crystal length of 10 mm.

Now for a given m_a we can find g_a from Eq. (4.8) and g_b from the zeros of Eq. (4.10). In general the roots must be calculated numerically, although for the case $\Delta k_b = 0$ the values of g_b which give $W(m_a, g_b) = 0$ can be written in terms of incomplete elliptic integrals of the first kind. Results for CPD states are plotted in the (g_a, g_b) plane in Fig. 4.2. Also plotted here is a line with a slope of one half. Since both g_a and g_b are proportional to the square root of the incident pump intensity, this line represents the operating line of the OPO-DFM device with $g_b/g_a = 0.5$. It is clear that there is significant overlap of the operating line with the CPD state. This indicates that there is a large dynamic range of pump intensity over which CPD is achieved. This is a particularly attractive characteristic of the OPO-DFM device since actual devices have spatial and usually temporal variations in the pump irradiance. Figure 4.3 shows plots of the signal, idler and transmitted pump power as a function of incident pump power for $g_b/g_a = 0.5$. All other parameters are as before. The difference frequency power is not plotted. As the transmitted pump power goes to zero over the domain where the two lines in Fig. 4.2 overlap. This is in stark contrast to the OPO, where the transmitted pump continues upward due to back-conversion. We also see a large increase in idler power and decrease in signal power for the OPO-DFM device as compared to the OPO. As pump depletion increases, the signal power out of the OPO crystal increases. Thus, the decrease in signal power observed is at the expense of increased idler power. Of course increased pump depletion also means that more idler radiation is generated in the OPO crystal for the OPO-DFM as compared to the OPO.

Finally we plot in Fig. 4.4 the difference-frequency and idler photon-conversion efficiencies as a function of incident pump power. The idler and difference-frequency photon-conversion efficiencies are near two and one respectively for the range of pump powers over the range of pump powers we can access with our experimental setup. They do not reach two and one due to the outcoupling loss included in the simulation.

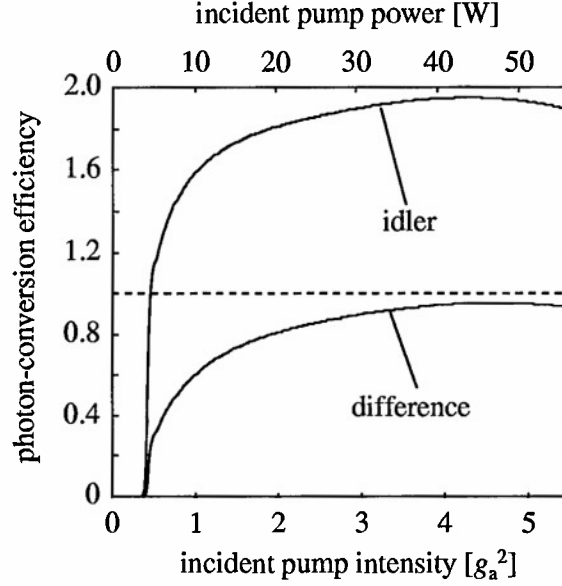


Figure 4.4: Idler and difference-frequency photon-conversion efficiencies for an OPO-DFM device.

4.2.2 OPO-DFM modeling of complete coupled wave equations

In order to model the temporal shape of the pulses in a synchronously pumped OPO-DFM device, we need to modify Cheung's model [41] introduced earlier in Section 3.2.4. Specifically, we change the gain term in Eq. (3.31) so that it includes additional terms representing the parametric loss of the DFM interaction. We then find for the gain

$$g_o(t) = aI_p(t) + \frac{2}{3}a^2I_p^2(t) - abI_1(t)I_p(t) - a^2bI_1(t)I_p^2(t) \quad (4.11)$$

or in terms of the normalized parameters introduced earlier in Section 3.2.4

$$g_o(t) = \hat{I}_p(t) + \frac{2}{3}\hat{I}_p^2(t) - \frac{b}{a}\hat{I}_1(t)\hat{I}_p(t) - \frac{b}{a}\hat{I}_1(t)\hat{I}_p^2(t). \quad (4.12)$$

Details of the derivation of this gain equation and Eqs. (4.13–4.17) below are given in Appendix A. The two additional terms in Eqs. (4.11,4.12) are derived with an

expansion of the solutions (Eqs. (4.3,4.4) and associated Manley-Rowe equation) to the simplified coupled wave equations for the DFM interaction. We neglect GVM and GVD in the DFM interaction since we know from our previous analysis of the OPO in Chap. 3 that these effects are small for this particular system in comparison to the pulse lengths involved in the interactions.

Once Eq. (3.31) is solved with the modified gain term (Eq. 4.12)) we are able to calculate the transmitted pump power $I_{xp}(t)$, idler power generated in the OPO interaction I_{iOPO} , total idler power $I_i(t)$, signal power generated in the OPO interaction $I_{sOPO}(t)$, and difference-frequency power $I_d(t)$.

$$I_{sOPO}(t) = \text{hat}I_1(t) \left[1 + I_p(t) + \frac{2}{3}I_p^2(t) \right] \quad (4.13)$$

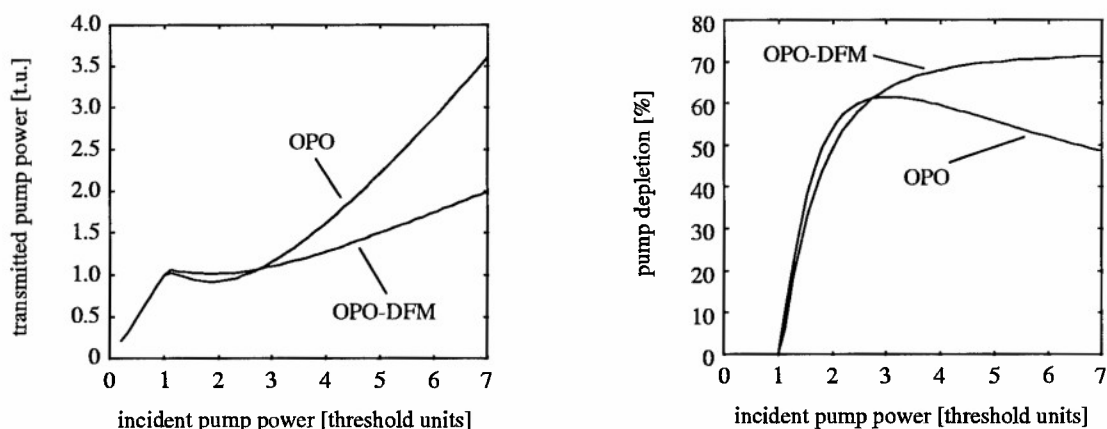
$$I_{xp}(t) = I_p(t) - \frac{\omega_p}{\omega_s} \left[I_{sOPO}(t) - I_1(t) \right] \quad (4.14)$$

$$I_{iOPO}(t) = \left[I_p(t) - I_{xp}(t) \right] \frac{\omega_i}{\omega_p} \quad (4.15)$$

$$I_i(t) = \left[I_{sOPO}(t) - I_1(t) \right] \frac{\omega_i}{\omega_s} + I_{iOPO}(t) \quad (4.16)$$

$$I_d(t) = \left[I_{sOPO}(t) - I_1(t) \right] \frac{\omega_d}{\omega_s} \quad (4.17)$$

Results of this model showing the transmitted pump power and pump depletion as a function of incident pump power are shown in Figs. 4.5(a) and (b) respectively. Also shown are the OPO numerical results for comparison. Figure 4.6 shows the temporal profiles of the transmitted pump pulses for incident pump powers 1.5, 2.5, 5.5 and 7.0 times above threshold for plots (a)–(d) respectively. From the temporal profiles it is clear that back-conversion of the pump in the OPO-DFM device is strongly reduced. This results in greater overall pump depletion for the OPO-DFM device as compared to the OPO for incident pump powers greater than ~ 3 times threshold. Figure 4.5(b) shows that the pump depletion increases from 49% to 71% at pumping seven times above threshold.



(a) Theoretical transmitted pump power for OPO and OPO-DFM versus incident pump power.

(b) Theoretical pump depletion for OPO and OPO-DFM versus incident pump power.

Figure 4.5: Theoretical results for transmitted pump power and pump depletion for OPO and OPO-DFM generated with model discussed in Section 4.2.2. All values, except the OPO crystal bandwidth, for the theoretical parameters used to generate the curves are chosen to be equivalent to the experimental values. The OPO crystal bandwidth was chosen to be 20 times smaller than what is expected from theory.

4.3 Experimental design

The OPO-DFM device we constructed was designed as an extension of the OPO discussed in Chap. 3. Thus the pump laser and PPLN crystal for the OPO interaction are not free to be varied. This then leaves two main issues to be examined: 1) DFM crystal selection and 2) cavity design. It is also useful to calculate the various bandwidths for the DFM interaction and contrast these with those of the OPO interaction.

We choose to use PPLN for the DFM crystal. One reason for this is its ability to noncritically phasematch for any wavelength within its transparency range. Thus, using PPLN eliminates spatial walk-off. In addition to this, PPLN is a good choice because it naturally leads to the next step in OPO-DFM device construction. That is, once the correct DFM grating period and grating length are identified, it will be

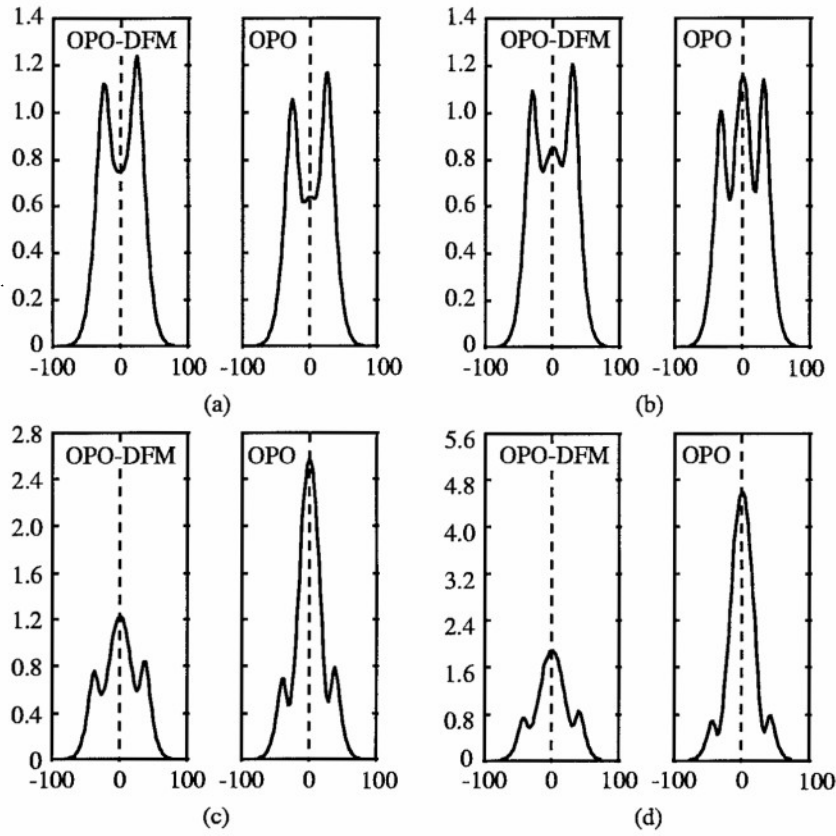


Figure 4.6: Theoretical temporal profiles of transmitted pump for OPO and OPO-DFM generated using model in Section 4.2.2. Parameters used to generate plots same as those for Fig. 4.5 with incident pump powers (a) 1.5, (b) 2.5, (c) 5.5, and (d) 7.0 times above threshold. The effective cavity detuning, δT_{eff} is zero. Power units are arbitrary. Unit for the x -axis are picoseconds.

possible to integrate both the OPO and DFM interactions on the same lithium niobate wafer. This will make the OPO-DFM device compact and eliminate unavoidable losses in the signal and idler radiation between the OPO and DFM crystals. Now we need to identify the required grating periods for the DFM interaction at various OPO crystal operating temperatures and the required grating length for optimum coupling of the OPO and DFM interactions.

The grating length of the DFM interaction is dictated by the particular value of g_a that we have for our baseline OPO and the requirement that the ratio of coupling parameters, $g_b/g_a = 0.5$, is achieved (see Fig. 4.2). Recall that plane-wave theory indicates that this ratio of coupling parameters predicts CPD over a wide range of incident pump intensities for the OPO-DFM device. The DFM coupling parameter g_b is linearly proportional to the grating period length L_b (see Eq. (4.7)). Thus, specifying L_b provides an easy way to engineer the correct value of g_b so that the correct ratio of coupling parameters is satisfied. Specifically we have for L_b

$$L_b = L_a \frac{g_b}{g_a} \frac{d_a}{d_b} \sqrt{\frac{\omega_p n_d}{\omega_d n_p}} \quad (4.18)$$

where d_a and d_b are the effective nonlinear coefficients for the OPO and DFM interaction respectively. The ratio d_a/d_b can be estimated using Miller's rule [112, 113]. In any basic textbook on nonlinear optics the relation

$$\chi_{ijk}^{(2)}(\omega_1, \omega_2, \omega_3) = [\chi_{ii}^{(1)}(\omega_1)][\chi_{jj}^{(1)}(\omega_2)][\chi_{kk}^{(1)}(\omega_3)]\Delta_{ijk} \quad (4.19)$$

is derived for a three-wave interaction [24]. This relation is the general form of Miller's rule who determined that the factor Δ_{ijk} is almost constant for many materials. Now the first order susceptibility $\chi^{(1)}(\omega)$ is proportional to $(n^2(\omega) - 1)$, so that we can write $d_a/d_b = (n_p^2 - 1)/(n_d^2 - 1)$. We find that for the 13 mm baseline OPO crystal that a 10 mm long DFM grating is needed when both crystals are at room temperature. We also calculate that any combination of OPO and DFM crystal temperatures in the temperature range from 20-200° C changes the coupling ratio by less than one percent.

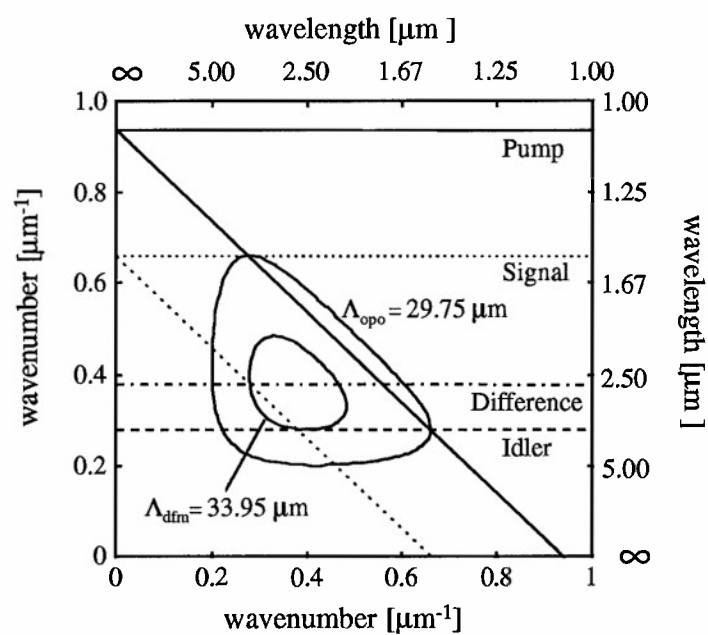
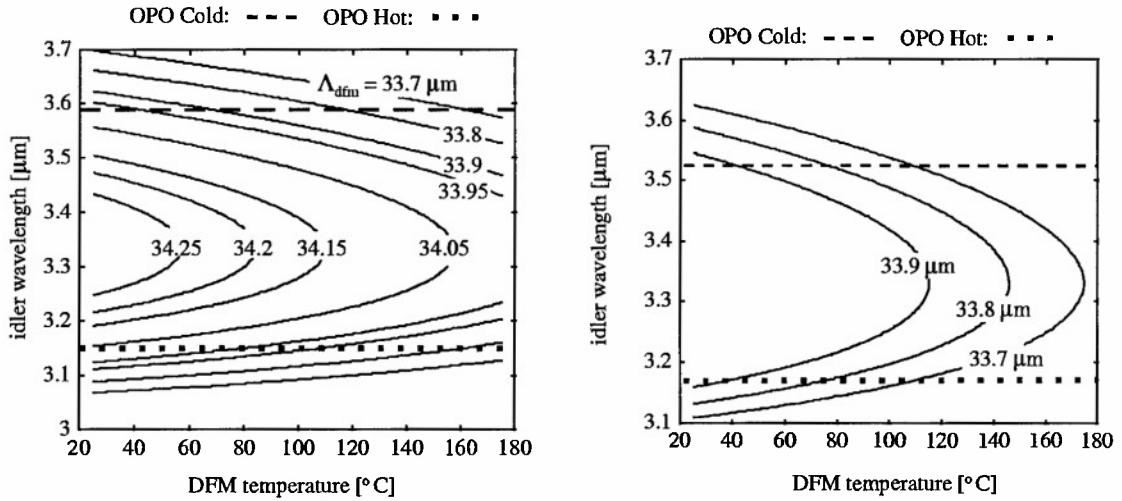


Figure 4.7: Room temperature grating period diagram for OPO and DFM interactions for an OPO-DFM device.

The grating period required for the DFM interaction is dictated by the signal and idler radiation that is generated in the DFM interaction. The signal and idler radiation interacts in the DFM interaction to create additional idler radiation and radiation at the difference-frequency given by $\omega_d = \omega_s - \omega_i$. Using Eq. (2.5), with $n = 1$ for first-order QPM, we can determine the grating period Λ_{dfm} required for phasematching the DFM interaction. At room temperature we find that $\lambda_d = 2.7 \mu\text{m}$ and $\Lambda_{\text{dfm}} = 33.95 \mu\text{m}$. Fig. 4.7 is a grating contour diagram showing the OPO and DFM interactions. In this diagram we see that the signal and idler generated in the OPO interaction are represented by lines that intersect the $33.95 \mu\text{m}$ DFM grating contour.

It is important to obtain a DFM PPLN crystal with several grating periods. The reason for this is that refractive index dependencies on temperature and wavelength in lithium niobate can change from boule to boule. In addition, historically Sellmeier relations have been less accurate at higher temperatures in providing calculated tuning curves that agree with experimental data. For example, see Fig. 3.2 in which there is a greater discrepancy at higher temperatures between the calculated curve (generated from Sellmeier and thermal expansion relations) and the experimental data for our OPO. Thus, it is prudent to bracket the predicted required room-temperature DFM grating periods with grating periods of greater and lesser period. Fig. 4.8(a) plots room-temperature DFM grating contours in the (DFM crystal temperature idler wavelength) plane. The Sellmeier relations used to generate these plots were taken from Edwards' [111]. Also shown are two horizontal lines indicating the operating idler wavelength for the device when the OPO crystal is at 25°C and 200°C . Any idler wavelength between these two lines can be generated by heating the OPO crystal to the appropriate temperature. The DFM grating periods used to generate the contours in these plots represent grating periods on the DFM crystal acquired from a commercial vendor. It is a eight-grating crystal with dimensions $10 \text{ mm} \times 15 \text{ mm} \times 0.5 \text{ mm}$. Each grating period had a width of $\sim 1.2 \text{ mm}$ and the grat-



(a) DFM room temperature grating contours using Edwards' [111] Sellmeier relations.

(b) DFM room temperature grating contours using Jundt's [65] Sellmeier relations.

Figure 4.8: DFM room temperature grating contours.

ings were separated from each other by ~ 0.6 mm. Figure 4.8(b) plots contours for the same DFM grating periods using more recent Sellmeier relations of Jundt that were published after the DFM crystal was purchased [65]. Notice that there is a shift of the grating contours to shorter idler wavelengths when they are generated using Jundt's Sellmeier relations as compared to Edwards' Sellmeier relations. Comparison of these two plots, with the shift in the grating contours, emphasizes the need to acquire a multi-grating DFM crystal. In this way uncertainty in the Sellmeiers can be accounted for.

As the OPO-DFM device is tuned by changing the OPO crystal temperature, different idler/signal wavelength pairs are generated requiring different DFM room temperature grating periods for phasematching this nonlinear interaction. It is possible to simultaneously tune the DFM interaction by independently controlling the temperature of the DFM crystal. In fact, usually some temperature tuning is required to be sure that the DFM phasematching is optimized. In this work we have kept the temperature of the PPLN crystals below 200°C . Heating of the crystals liberates oxy-

gen from the lithium niobate, creating an oxygen depleted niobium layer [114–116]. The oxygen depleted layer creates a surface which has been shown to reduce the crystal damage threshold.

Bandwidth characteristics of the DFM interaction are also important to analyze. Bandwidths are calculated using the analysis discussed in Chap. 2. The appropriate bandwidth values are shown in Table 4.1 for the DFM interaction. Also written in Table 4.1 for comparison are the various bandwidths previously given in Table 2.1 for the OPO interaction. Particular attention should be paid to the signal

	OPO	DFM
Temperature BW ($^{\circ}\text{C}$)	25	19
Signal Spectral BW (nm)	5	10
“Pump” Angle BW ($x - y$) (mrad)	83	69
“Pump” Angle BW ($x - z$) (mrad)	93	10
Pump BW (nm)	1	N/A

Table 4.1: Acceptance bandwidths for OPO and DFM interactions. “Pump” refers to the pump laser in the OPO interaction and the signal wave for the DFM interaction.

spectral bandwidth of the OPO and DFM interactions. The spectral bandwidth of the OPO interaction is smaller than the DFM interaction. This is preferred, since it prevents the OPO from oscillating at a signal frequency at which the loss represented by the DFM interaction is nonexistent or small. A similar concern is the amount of angle that the OPO and DFM devices can tolerate for the signal beam. If the DFM interaction has a smaller signal angle bandwidth than the OPO interaction it may be possible for the OPO-DFM device to operate in a noncollinear fashion such that the strength of DFM interaction is lessened.

As a visual aid we plot in Fig. 4.9 the signal wavelength versus the angle ρ that the signal propagation vector makes with respect to the pump propagation vector for

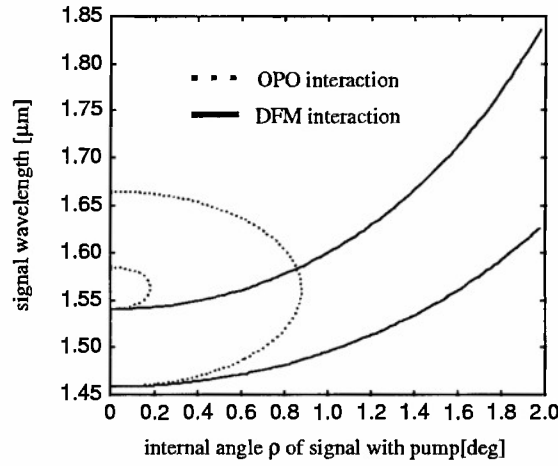


Figure 4.9: Signal wavelength versus noncollinear angle ρ for OPO and DFM interactions. The angle between the pump and grating vectors ϕ was taken to be zero. See Fig. 2.7(b) for wave vector diagram.

two sets of curves. The pump propagation vector and grating vector are parallel for generation of these curves ($\phi = 0$). It is clear that the OPO interaction is able to tolerate much greater noncollinear angles ρ than the DFM interaction for both sets of curves. The two sets of curves correspond to different signal wavelengths when the OPO-DFM device is collinearly aligned. The set of curves which gives a signal of $1.54 \mu\text{m}$ for collinear phasematching ($\rho = 0$) corresponds to the experimental conditions. The other set of curves indicates that the discrepancy between angular acceptance of the DFM and OPO interactions can be mitigated by going to shorter signal wavelengths and longer idler wavelengths. Of course a signal wavelength shorter than $1.35 \mu\text{m}$ implies an idler wavelength greater than $5.02 \mu\text{m}$ at which lithium niobate becomes strongly absorptive. We have found that the OPO-DFM device must be carefully aligned for collinearity to obtain optimum performance. Alignment is discussed in the next section.

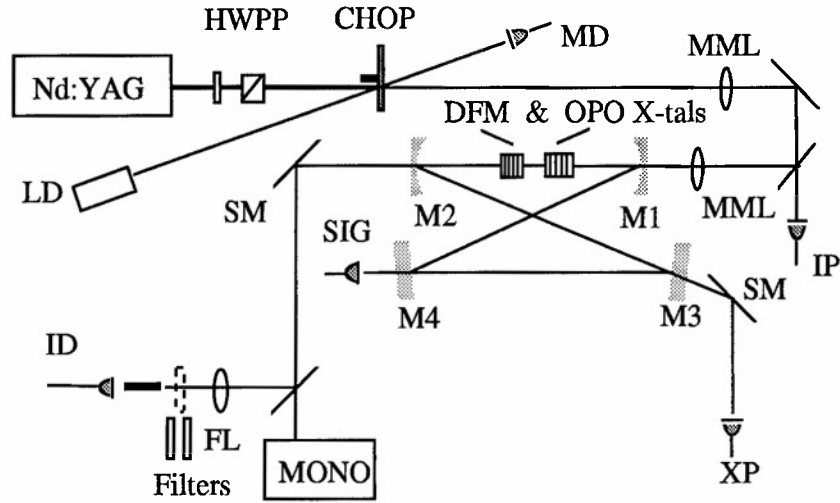


Figure 4.10: Schematic diagram of experimental setup. A half-wave plate and polarizer (HWPP) are used to adjust the power from the laser, MML is the mode matching optics, and MONO represents the diagnostics for the measurements. The two crystals are separated by ~ 1 mm at the beam waist of the pump and signal waves. The fold angle of the resonator is about 1.0° .

4.4 Experimental setup

Figure 4.10 is a sketch of the experimental set-up. It is very similar to the experimental set up for the OPO work done in Chap. 3. For both the OPO and DFM crystals we use PPLN. The OPO-DFM device is pumped by $1.064 \mu\text{m}$ radiation of a Nd:YAG laser, mode-locked at 76 MHz and producing up to 18 W of average power. The pulsewidth is 100 picoseconds. We can operate the device in both chopped and unchopped modes. The chopper (CHOP) runs at 160 Hz with a 24:1 duty cycle. The signal and idler wavelengths are near $1.5 \mu\text{m}$ and $3.5 \mu\text{m}$ respectively, while the difference wavelength is near $2.8 \mu\text{m}$. The QPM grating period of the 13-mm long OPO crystal is $29.75 \mu\text{m}$ and is the same one used for the OPO in Chap. 3. The length of the DFM crystal, 10-mm, was chosen such that the ratio of coupling parameters g_b to g_a for the DFM and OPO process is one half. For this ratio of coupling parameters, plane wave analysis predicts complete pump depletion states [7]. The DFM crystal has eight different QPM gratings ranging from 34.25 – $33.70 \mu\text{m}$ and is described in

detail in the previous section. The OPO crystal is anti-reflection (AR) coated for the pump and signal wavelengths, while the DFM crystal is AR coated for the idler and signal wavelengths. The OPO and DFM crystals are placed in separate copper ovens. Each oven is heated with two 1/8 inch diameter cartridge heaters and is independently controlled with a commercially available temperature controller. Control of the crystal temperatures allows temperature tuning of the device. Both the OPO and DFM crystals are held at elevated temperatures to real-time anneal photorefractive effects that have been observed in PPLN [29].

All four one-inch diameter mirrors are high reflectors at the signal wavelength. Mirror M1 is highly transmitting (HT) at the pump frequency and mirror M2 is HT at the idler, pump and difference frequencies. Each is concave with $R = 0.75$ m. Mirrors M3 and M4 are flat. Mirror M4 is on a translation stage. Since the idler and difference-frequency waves start from zero at the beginning of the OPO and DFM interactions respectively, the OPO is singly resonant and the DFM is not sensitive to the relative phase between the incident signal and idler waves. The pump waist was measured to be $90\text{ }\mu\text{m}$, while the cavity waist for the signal was calculated to be $110\text{ }\mu\text{m}$. Referring to Table 3.4, this is the tightest pump waist possible before the worst case ($b_p = b_s \neq b_i$) idler spot size will clip the exit face of the DFM crystal. Total round-trip loss of the signal is estimated to be $\sim 5\%$ from energy conservation considerations. This loss agrees well with the “internal” loss calculated for the OPO in Chap. 3. These should nominally be the same.

As mentioned in the previous section, cavity alignment for collinearity is critical for optimum OPO-DFM operation. In addition, we align the pump and signal beams for optimum spatial overlap. Alignment procedures are done near threshold to avoid any coupling effects between the OPO and DFM interactions. We performed alignment with the aid of an infrared camera. The infrared camera output is sent to a computer for digitization and real-time display. For spatial alignment we steer the signal and pump beams through M2 to the camera. We use the camera lens to image

the beams at the crystals. While the image from the camera is monitored, the cavity mirrors M1–M4 are adjusted so that the two beams overlap.

To align the signal and pump beam k -vectors for collinearity we removed the lens from the infrared camera. The two beams through M2 were focused onto the camera detection plane using an external focusing lens with a focal length of 10.0 cm. Thus, we could easily align for a collinearity angle of less than one degree, since the image beams displayed on the computer had a resolution of about 50 μm .

4.5 Results

We present experimental results in the following sections. Comparison of the simple OPO to the OPO-DFM device is made whenever appropriate. In this work the simple OPO is defined to be operation with both the OPO and DFM crystals in the cavity, but with the DFM interaction far from phasematching. This is accomplished by either by controlling the temperature of the DFM crystal or translating the DFM crystal from a phasematched grating to a grating far from phasematching. The following sections clearly show reduced back-conversion of the pump due to the DFM interaction, which effectively outcouples some of the resonant signal radiation.

4.5.1 General OPO-DFM characterization

In this section we present experimental results that show the general operating characteristics of the OPO-DFM device. More quantitative results and analysis is presented in the next section. For the data in this section the device is run in a chopped mode to reduce the average power. Cavity detuning results for the OPO-DFM device are similar to the simple OPO. Figure 4.11 is a plot of normalized signal efficiency as a function of cavity detuning for the simple OPO and for the OPO-DFM device. For the plots in this Section OPO-DFM operation is defined by setting the OPO crystal temperature at 72.5° C and the DFM crystal temperature at 125° C. We define OPO

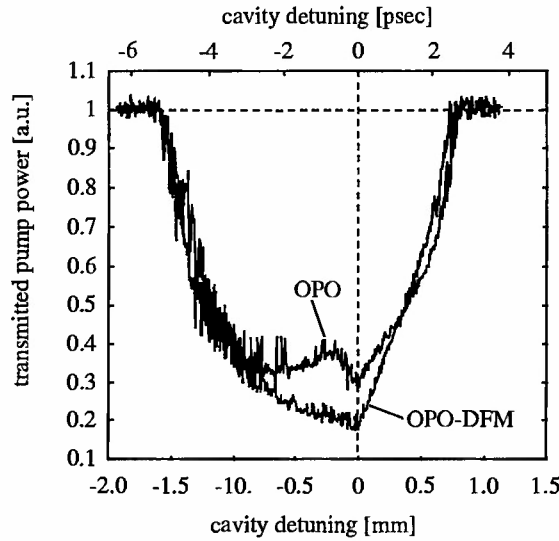
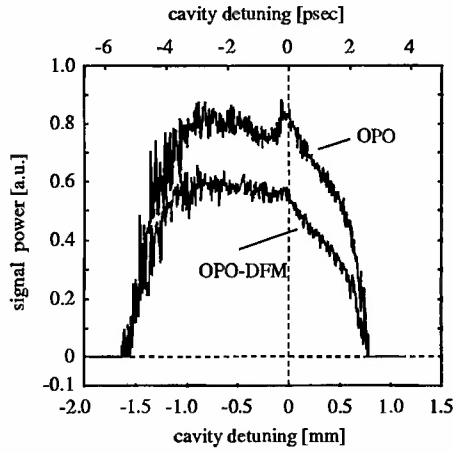


Figure 4.11: Transmitted pump power versus cavity detuning for OPO and OPO-DFM.

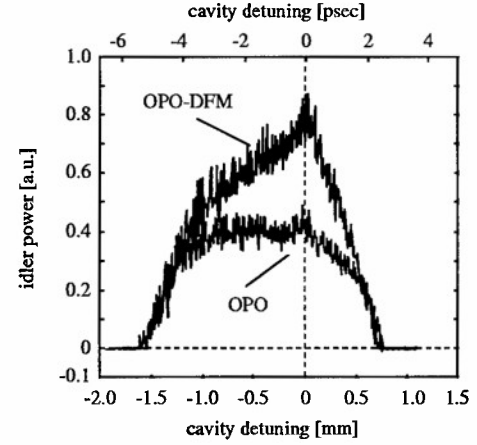
operation by heating the DFM crystal to 78°C , which as seen from Fig. 4.18 is far from the DFM crystal phasematching condition.

The waist of the pump located between the DFM and OPO crystals. The DFM grating period is $33.7\text{ }\mu\text{m}$. The pump depletion increases from 69% for the simple OPO to 79% for the OPO-DFM device. Although the pump depletion increases for the OPO-DFM device, we see in Fig. 4.12(a), which plots signal power versus cavity detuning, that the signal power decreases. This is due to some of the signal radiation being converted into idler and difference-frequency radiation in the DFM crystal. The increase in idler power as a function of cavity detuning is seen when comparing the two traces in Fig. 4.12(b) for the OPO and OPO-DFM.

The cavity detuning lengths seen here and longer than in Chap. 3 due to a smaller pump waist and hence higher nonlinear drive. The higher nonlinear drive is due to the tighter focusing of the pump beam. Also due to the higher nonlinear drive, there is greater back conversion of the pump, and hence less pump depletion at full power for the simple OPO, as compared to the results in Chap. 3.



(a) Signal power versus cavity detuning for the OPO-DFM and simple OPO.

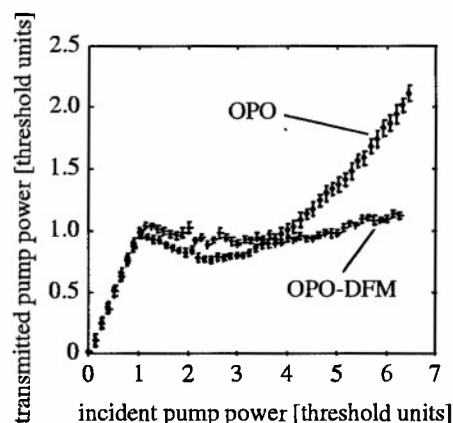


(b) Idler power versus cavity detuning for the OPO-DFM and simple OPO.

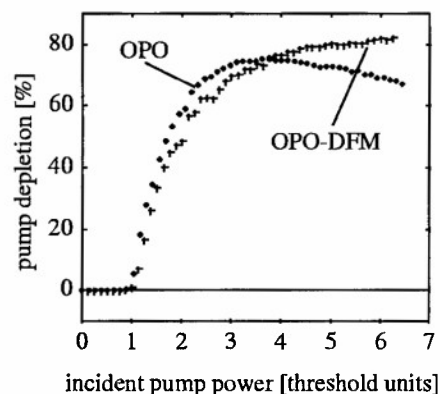
Figure 4.12: Experimental cavity detuning results for the simple OPO and OPO-DFM devices.

We also identify the strong asymmetry in the simple OPO transmitted pump trace as another effect due to back-conversion of the pump. The simple OPO transmitted pump power increases in the domain from -0.5 psec to -0.2 psec. This is an integrated effect and is attributed to backconversion as the signal becomes stronger near synchronization. This same effect was seen in Chap. 3 for the time and space resolved transmitted pump. It is now seen for the integrated transmitted pump due to the strong pumping achieved because of the tighter focusing of the pump and signal as compared to before.

Demonstration of the reduction of back-conversion of the pump is further seen when examining Figure 4.13. Here we plot (a) transmitted pump power and (b) pump depletion versus incident pump power for the OPO and OPO-DFM. For these plots the cavity length was set at synchronism as determined by cavity detuning scans (see Figure 4.11). There is remarkable similarity between the general shape of these plots and the theoretical plots given in Figs. 4.5(a) and (b). The main discrepancy between



(a) Transmitted pump power versus incident pump power for OPO-DFM and simple OPO.



(b) Pump depletion versus incident pump power for OPO-DFM and simple OPO.

Figure 4.13: Experimental results for OPO and OPO-DFM devices.

theory and experiment is that the theory predicts smaller overall pump depletions and the local minimum for the transmitted pump (local maximum for the pump depletion) occurs at an incident pump power of about 2 times above threshold as compared to 2.8 times threshold for the experimental data.

Figures 4.14(a) and (b) show the signal and idler powers versus incident power for the simple OPO and OPO-DFM devices with the operating parameters the same as those in Figures 4.11 and 4.13. Clearly the idler power increases and the signal power decreases for OPO-DFM operation as compared to the simple OPO. As mentioned before, the additional idler power comes at the expense of reduced signal radiation and increased pump depletion. We also see from these figures, as expected from theory, that the thresholds for the OPO and OPO-DFM are the same. [7]

4.5.2 Power studies

For the results presented in this section OPO-DFM operation is defined to be the OPO crystal at 72.5° C and the DFM crystal at 125° C as before. Also as before, the

DFM grating period is $33.7 \mu\text{m}$. OPO operation is defined to be with both crystals at the same temperature as in OPO-DFM operation, but the DFM crystal is translated horizontally to a grating period ($33.15 \mu\text{m}$) which is far from the phasematching condition. This eliminates differences between OPO and OPO-DFM operation due to unwanted temperature effects. These effects include misalignment and cavity de-synchronization. The data is taken in the unchopped mode.

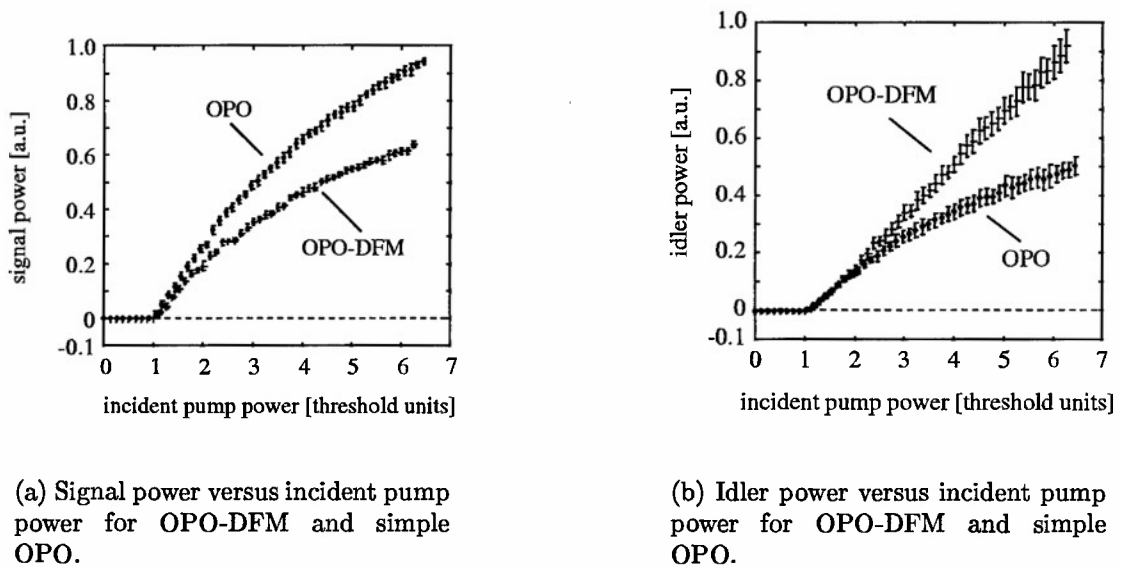
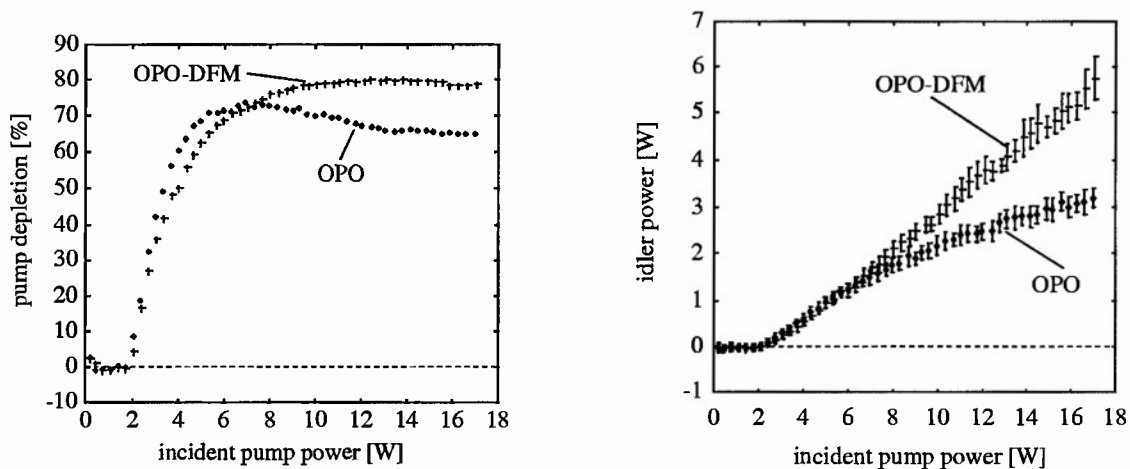


Figure 4.14: Experimental results for OPO and OPO-DFM devices.

Pump depletion and idler power as a function of incident pump power are plotted in Fig. 4.15. At full pump power, pump depletion for the OPO is 65%, which corresponds to 3.3 W of idler power, and the measured idler power is 3.2 W, after accounting for the transmission of the optics. The measured idler radiation from the OPO-DFM device is 5.7 W, 180% that of the OPO, and the idler power conversion efficiency of the OPO-DFM device is 35%. The pump depletion has increased to 79%.

For the OPO, pump depletion falls off at incident pump powers greater than 7.0 W because of back-conversion of the pump. In contrast, back-conversion of the pump in the OPO-DFM is mitigated. Pump depletion of the OPO-DFM device below



(a) Percent pump depletion for the simple OPO and OPO-DFM.

(b) Idler power for the simple OPO and OPO-DFM.

Figure 4.15: Percent pump depletion and idler power for the simple OPO and OPO-DFM as a function of incident pump power. The OPO crystal temperature is at 72.5° C and the DFM crystal is at 125° C.

an incident pump power of 7.0 W is less than or equal to the OPO, although the idler power conversion efficiency of the OPO-DFM is never lower than that for the OPO. There is more power in the OPO-DFM idler beam as compared to the OPO idler beam when the incident pump power is greater than 5.5 W. This increased idler power results from increased pump depletion, as well as reduced circulating signal power ($\sim 62\%$ at full pump power) in the OPO-DFM as compared to the OPO.

In Fig. 4.16 we plot photon-conversion efficiencies for the idler as a function of incident pump power for the two cases where the DFM interaction is and is not phasematched and the difference-frequency photon conversion efficiency when the DFM interaction is phasematched. The idler photon conversion efficiencies η_i are determined using two separate methods. First, the measured idler and incident-pump powers are used directly as

$$\eta_i = \frac{\text{idler power}}{\text{incident pump power}} \frac{\lambda_i}{\lambda_p}, \quad (4.20)$$

where λ_p and λ_i are the pump and idler wavelengths. Second, independent determi-

nations for idler photon-conversion efficiency η_i (and the only determination for the photon-conversion efficiency for the difference-frequency radiation η_d) are inferred from the Manley-Rowe and closure relations for the OPO,

$$\begin{aligned} p_1 + s_1 &= p_2 + s_2, \\ p_1 &= p_2 + i_2, \\ s_1 &= s_2 R_s, \end{aligned} \tag{4.21}$$

and the OPO-DFM,

$$\begin{aligned} P_1 + S_1 &= P_2 + S_2, \\ P_1 &= P_2 + I_2, \\ S_2 + T_i I_2 &= S_3 + I_3, \\ S_2 &= S_3 + D_3, \\ S_1 &= S_3 R_s. \end{aligned} \tag{4.22}$$

The subscripts 1, 2, and 3 in Eqs. (4.22,4.23) refer to spatial positions just inside the entrance face of the OPO crystal, just before the exit face of the OPO crystal, and just before the exit face of the DFM crystal, respectively. The letters p (P), s (S), and i (I) label photon numbers for the pump, signal and idler respectively for OPO (OPO-DFM) operation. R_s is the total round-trip reflectance of the resonated signal radiation and T_i is the transmittance of the idler between the two crystals due to air-crystal interfaces at the exit face of the OPO crystal and input face of the DFM crystal. In addition to these equations we use measured ratios of the transmitted pump $\alpha = p_2/P_2$ and signal $\gamma = S_3/s_2$ with and without DFM, as well as the fraction of transmitted pump $\beta = p_2/p_1$ for the OPO. Taking $p_1 = P_1$ and solving Eqs. (4.22,4.23) we find for the OPO,

$$\eta_i = \frac{i_2}{p_1} = 1 - \beta \tag{4.23}$$

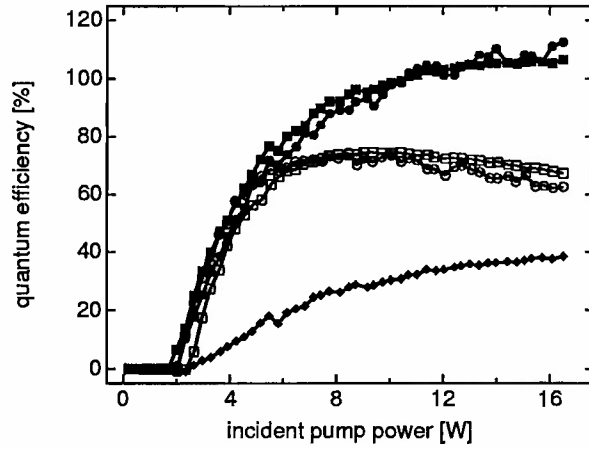


Figure 4.16: Measured idler (filled circles), inferred idler (filled squares), and inferred difference-frequency (filled diamonds) photon-conversion efficiencies for the OPO-DFM and measured (open circles) and inferred (open squares) idler photon-conversion efficiency for the OPO as a function of incident pump power. The OPO-DFM idler photon-conversion efficiency is greater than 100% for incident pump powers greater than 11.0 W.

and for the OPO-DFM,

$$\eta_i = \frac{I_3}{P_1} = (1 + T_i)(1 - \beta/\alpha) + \gamma(\beta - 1) \quad (4.24)$$

$$\eta_d = \frac{D_3}{P_1} = (1 - \beta/\alpha) + \gamma(\beta - 1). \quad (4.25)$$

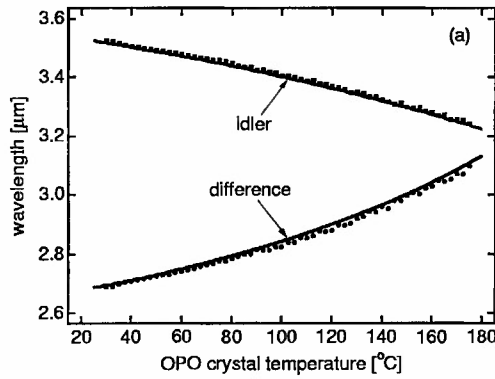
The outstanding feature in Fig. 4.16 is that the photon-conversion efficiency of the idler for the OPO-DFM is greater than 100% for incident pump powers greater than 11.0 W, reaching 110% and still increasing at the full pump power of 16.5 W. Plane-wave theory predicts an 8% improvement for the idler photon conversion efficiency for the OPO-DFM device when the idler transmission from the OPO crystal to the DFM crystal is increased from its present value of 86% to 100%. A nondegenerate idler photon-conversion efficiency greater than 100% for the OPO is physically impossible. The OPO idler photon-conversion efficiency reaches a maximum of 74% at a pump power of 7.0 W, and then begins to decrease due to back-conversion of the pump. Stronger pumping should also increase the DFM photon-conversion efficiency, which reaches 39% at full pump power and is still increasing. Higher nonlinear drive could be obtained with more pump power, tighter focusing in the crystals, or

increased crystal lengths. Much tighter focusing without clipping the beams at the crystal faces is not possible with the 0.5 mm thick crystals used in this system. Work has been done on poling thicker (1 mm) lithium niobate crystals [117] and on diffusion bonding several 0.5 mm thick pieces of PPLN together to form larger aperture crystals [118].

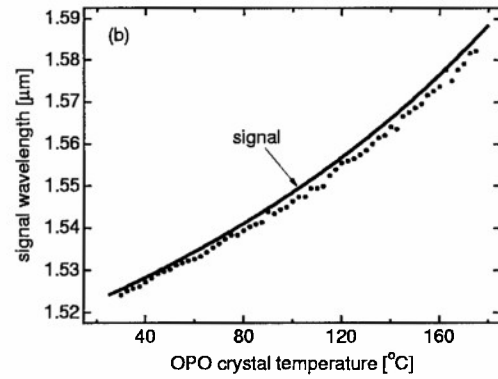
4.5.3 Temperature tuning and phasematching considerations

We have already mentioned that the OPO-DFM device is a frequency-agile source of radiation. Tuning can be accomplished by changing the the OPO grating period, and hence the DFM grating period as well. Tuning can also be accomplished by heating the OPO crystal. The device here did not have a multi-grating OPO crystal, and thus tuning of the device was done with temperature control of the OPO crystal. A plot of the signal, idler and difference wavelengths versus OPO crystal temperature is shown in Fig. 4.17. The solid lines are calculated using Jundt's Sellmeier relation [65] and a thermal expansion relation [67] for LiNbO_3 . In order for there to be good agreement between the calculated line and the experimental data it was necessary to introduce a small ($\sim 0.2^\circ$) internal angle between the pump and signal beams. The small internal angle does not affect the width of the calculated curve, but does shift the peak of the curve from 150° C to 125° C . Since we are able to align for collinearity with greater accuracy than this, it is believed that this small angle only plays the a role in modifying the Sellmeiers rather than truly representing noncollinear alignment in our system.

For any given OPO crystal temperature there is a particular set of signal and idler wavelengths. This set of wavelengths requires a specific DFM grating period, which can be calculated using Eq. (2.5). Since we have a limited number of DFM gratings, some temperature tuning of the DFM interaction is required. Figure 4.18 is a typical plot of the behavior of the difference-frequency and idler power as a function of DFM crystal temperature. The OPO-DFM device is aligned for beam overlap, cavity



(a) Idler and difference wavelengths versus OPO crystal temperature.



(b) Signal wavelength versus OPO crystal temperature.

Figure 4.17: Signal, idler and difference wavelength versus OPO crystal temperature.

synchronism and collinearity at low temperature. Data is taken by ramping the DFM crystal temperature from 65° C to 160° C at a rate of two degrees per minute. The non-phasematched idler power at high temperature, 155° C is not equal to the non-phasematched idler power at low temperature, 87° C due to device misalignment and cavity length detuning. The solid line in Fig. 4.18 is a phasematching curve calculate from Sellmeier [65] and thermal expansion relations [67] for lithium niobate. An interesting feature here is the dip in the powers seen at 112°C. This dip is due to third-order, quasi-phasematched generation of red light by the sum frequency process $\omega_p + \omega_s \rightarrow \omega_{red}$. An OPO with intracavity sum-frequency generation or OPO-SFG device has been previously studied both theoretically [39,40] and experimentally [27, 119]. One of the experimental devices [119] was based on PPLN and produced red light from a 12 W diode-pumped Nd:YAG laser with a record 21% power conversion efficiency. This power conversion efficiency should be greatly improved upon with a pulsed system, which can achieve much higher nonlinear drives.

Identification of higher-order quasi-phasematched processes is important and can be visualized with a grating-contour diagram. Figure 4.19 is a period plot in which we see phasematched third-order sum-frequency generation of red light and

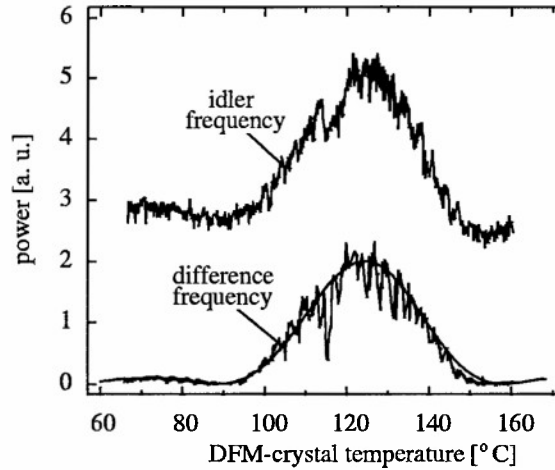


Figure 4.18: Difference-frequency and idler power versus DFM crystal temperature.

phasematched fifth-order second harmonic generation of green light. These higher order processes compete with the DFM interaction.

There is some flexibility in how the OPO-DFM device is phasematched when there is a multi-grating DFM crystal. In practice, it is possible to phasematch the DFM interaction with more than one DFM room-temperature grating period for a given set of signal and idler wavelengths. In Fig. 4.20 we plot calculated DFM grating contours. The contours were calculated with the same small internal angle ($\sim 0.2^\circ$) between the pump and signal k -vectors as mentioned above. By comparing these contours with the contours plotted in Fig. 4.8, where the internal angle was zero, we see that there is a shift to lower temperatures for the grating contours here. Also plotted are experimental data points indicating DFM phasematching temperatures for a given grating period and given idler wavelength (and hence corresponding signal wavelength dictated by energy conservation). In order to span the idler wavelength scale, the OPO crystal temperature was varied from 40°C , $\lambda_i = 3.54\text{ }\mu\text{m}$ to 180°C , $\lambda_i = 3.19\text{ }\mu\text{m}$. For each experimental point the DFM crystal temperature was scanned, producing a plot similar to Fig. 4.18, to identify the DFM phasematching

temperature.

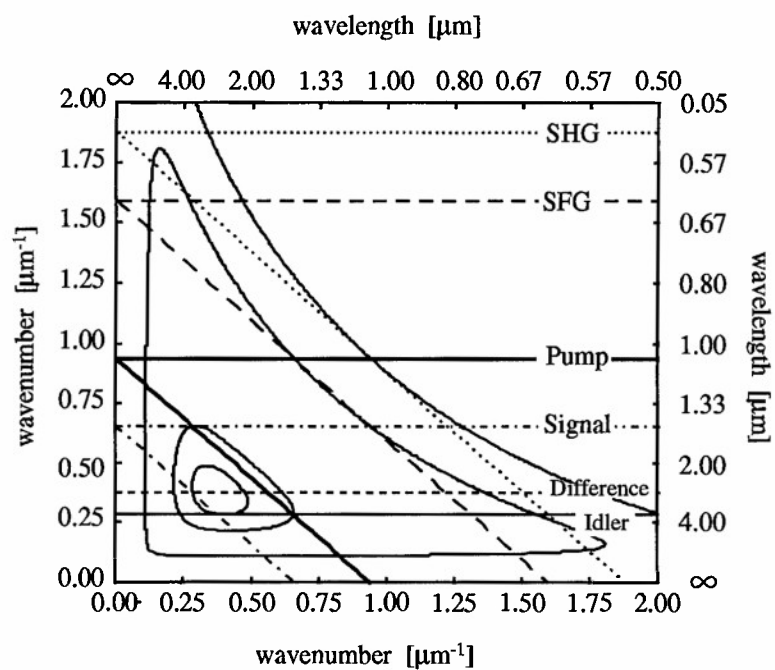


Figure 4.19: OPO-DFM grating contour diagram. Shown are first order QPM contours for the OPO and DFM processes as well as third and fifth order QPM contours for the DFM grating.

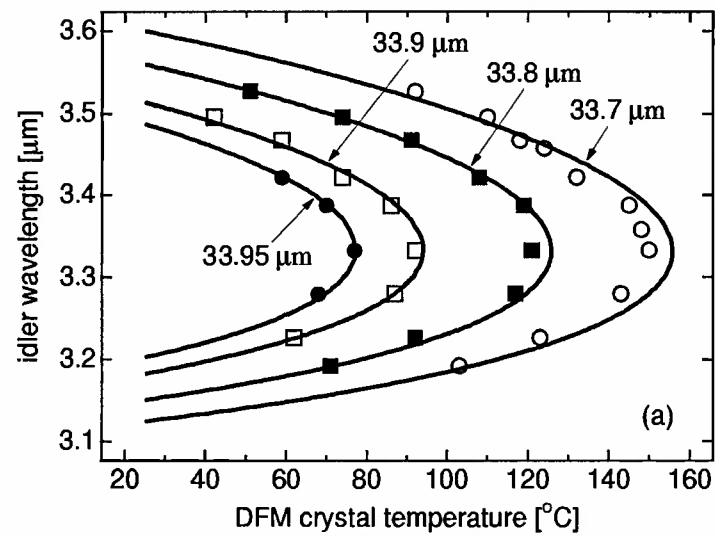


Figure 4.20: Experimental DFM grating contour plots.

Chapter 5

Conclusion and future work

5.1 Conclusion

In Chapters 3 and 4 we have presented theoretical, numerical and computational results of a synchronously pumped optical parametric oscillator (OPO) and a synchronously pumped optical parametric oscillator with intracavity difference frequency mixing of the signal and idler waves (OPO-DFM). The OPO-DFM device is designed to maximize the energy extracted at the idler wavelength near $3.5\text{ }\mu\text{m}$ and also produces radiation at the difference-wavelength of $2.7\text{ }\mu\text{m}$. The maximum idler power-conversion obtained for the OPO-DFM was 35% which is 80% greater than the simple OPO. This corresponds to an idler photon-conversion efficiency of 110% which is greater than the theoretical maximum of 100% for the simple OPO. Thus our OPO-DFM is a highly efficient source of mid infrared radiation. Comparison of OPO to OPO-DFM operation identified that the increase in idler power is due to the DFM interaction producing idler radiation and an increase in incident pump depletion. The increase in pump depletion was expected since the coupling parameters of the OPO and DFM interactions are chosen such that plane-wave analysis predicts complete pump depletion of a large dynamic range of incident pump intensities. In effect the strength of the DFM interaction is chosen to prevent back conversion of the

pump by limiting the amount of signal radiation incident upon the OPO crystal.

The OPO-DFM system we studied has several general characteristics which offer commercial possibilities. These include an all solid-state system, high efficiency, tunability, and engineerability. Some rather straightforward modification of the OPO-DFM device reported in this work should increase the efficiency further and make the device more user friendly. This will result in a system that is reliable, easily tuned, and robust.

5.2 OPO-DFM modifications

We first examine some general changes that can be made to the OPO-DFM device studied that should lead to more efficient operation. In the device studied the OPO and DFM crystals were physically different and thus there was an unavoidable loss in signal and idler radiation between the crystals. In fact, the DFM crystal was not AR coated for the signal wavelength and plane wave analysis has predicted an 8% increase in the idler photon-conversion efficiency if this loss was avoided. Thus, an AR coating on the DFM crystal at the signal wavelength should immediately improve efficiency. To eliminate any reflection losses the OPO and DFM gratings can be engineered onto the same lithium niobate crystal. Such PPLN crystals have been constructed and used in single-pass, back-to-back difference-frequency generation to produce radiation near $1.6\text{ }\mu\text{m}$ [120]. This device was operated at degeneracy, but because of the single pass geometry was not very efficient.

Another way to improve efficiency is to increase the nonlinear drive of the system. Since we want to reduce the requirements on the incident pump, we assume the nonlinear drive cannot be increased by increasing the average pump power. Thus, we must resort to longer crystals and tighter focusing geometries. Tighter focusing for the current system is not possible due to the limitations of the acceptance cross-section of the crystals. We have already referenced the work being done to increase

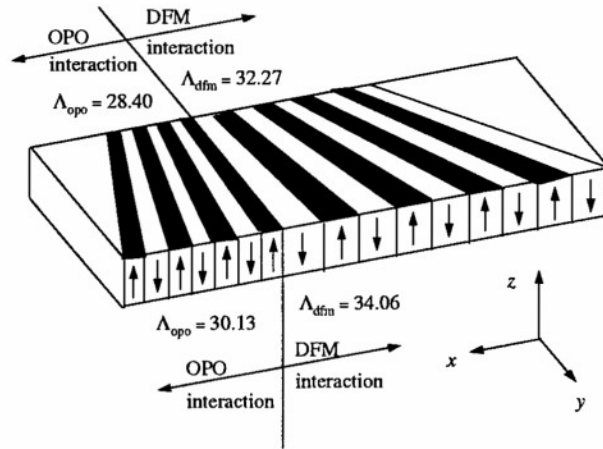


Figure 5.1: Fan-out grating OPO-DFM QPM crystal.

usable crystal thickness for PPLN [121].

In addition to higher efficiencies simplicity of design is always hoped for. Since PPLN technology allows the creation of multigrating crystals it should be possible to design a device that is tunable without using temperature control. This is possible by engineering for each OPO grating the appropriate DFM grating. Such a device would be tunable in discrete steps which is probably not adequate. A way to make a continuously tunable device (without temperature control) is the create fan-out gratings. Such gratings have been proposed [29] and demonstrated in a cw OPO [122]. A schematic of such a crystal is shown in Fig. 5.1. Such PPLN devices would still have to be operated at an elevated temperature in order to avoid photorefractive effects. Of course as other QPM materials become more readily available the photorefractive effect may no longer be of concern.

5.3 Future work

Past the modifications discussed in the previous section there is the question of the direction for future work. For pulsed systems there is always the push towards shorter pulse lengths. Femtosecond PPLN OPOs have been demonstrated [123,124] and there is no theoretical reason why a successful femtosecond OPO-DFM device cannot be realized. For example, if we are interested in generating $3.6\text{ }\mu\text{m}$ idler radiation (as in the system reported here) by pumping with a Ti:sapphire source the signal and difference-wavelengths are near 1.45 and $1.03\text{ }\mu\text{m}$ respectively. The walk-off between the signal (idler) and pump is 166 fsec/mm (158 fsec/mm) with the signal and idler leading the pump. Walk-off between the signal and idler is 9 fsec/mm (signal leading idler). Thus the interaction length in the OPO crystal is limited to $540\text{ }\mu\text{m}$. With confocal focusing into two crystal (OPO and DFM) which are a total of 3 mm long we get for g_a^2 a value which is larger than in the system we studied here. Since the walk-off between the signal and idler is small, there is good temporal overlap in the DFM interaction and efficient OPO-DFM operation should be achieved. Tuning of the idler between 3.4 and $4.8\text{ }\mu\text{m}$ can be accomplished with simultaneous pump wavelength and OPO and DFM temperature control while maintaining less than 50 fsec/mm walk-off between the signal and idler and less than 170 fsec/mm between the signal and/or idler and pump.

In building such a device it might be useful to employ a chirped grating to control for GVD as was investigated by Arbore [125] The idea for a chirped grating is that different parts of the chirped pump pulse phasematch at different sections of the chirped OPO grating. There would be some concern over the GVM effects since the signal and idler pulses out of the OPO crystal need to be time synchronized for efficient mixing in the DFM crystal.

Also possible is simultaneous parametric oscillation and down conversion. Devices that have exhibited simultaneous second harmonic and sum-frequency generation [126,127] and simultaneous sum-frequency and difference-frequency genera-

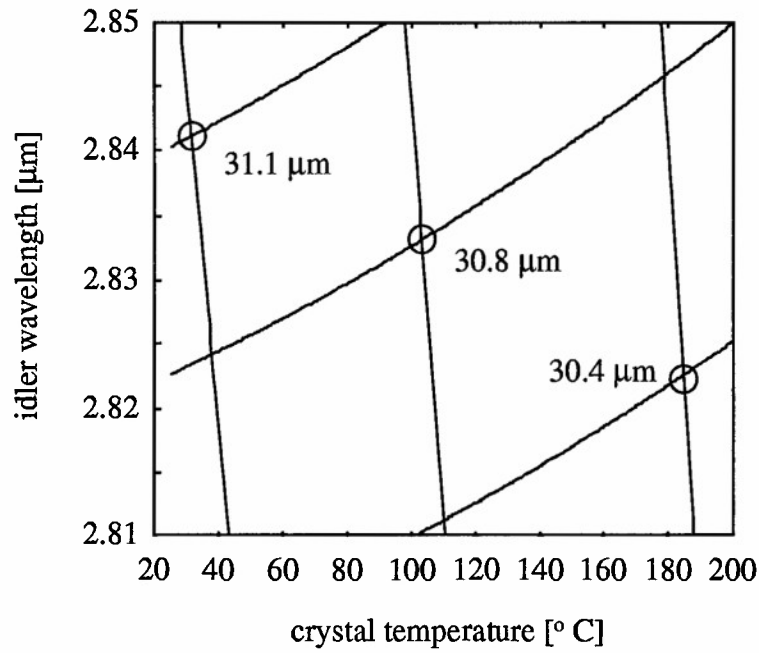


Figure 5.2: Simultaneous OPO-DFM QPM phasematching points.

tion [128] have been reported. Figure 5.2 is a plot of OPO and DFM grating contours for the idler wavelength versus crystal temperature and a $1.064 \mu\text{m}$ pump. Simultaneous OPO-DFM operation is possible at the temperatures where the same value OPO and DFM contours intersect. Tuning of a simultaneously phasematched OPO-DFM device can be accomplished with simultaneous crystal temperature control and pump wavelength control.

Appendix

Appendix A

Self-consistent OPO-DFM model

In this appendix we outline the derivation of the effective OPO-DFM gain term Eq. (4.11) and the various output powers Eqs. (4.13–4.18) given in Section 4.2.2 for the OPO-DFM device.

For the OPO interaction the plane wave equations which neglect GVD and GVM terms are given by Eqs. (2.21–2.22) with $1 \rightarrow s$, $2 \rightarrow i$, and $3 \rightarrow p$. The solution to these coupled equations are Jacobi-elliptic functions. We are interested in the solution for the signal and which is given by

$$\rho_s^2(z, t) = \rho_s^2(0, t) + \rho_p^2(0, t) \text{cn}^2(K_a - \sqrt{C_s} \kappa_a(z - z_1) | m_a) \quad (\text{A.1})$$

Here we have used the notation introduced in Section 3.2.3. Now at steady state the signal amplification per pass through the OPO crystal is assumed to be small and the solution for $\rho_s(L_a, t)$ is expanded about $L_a = 0$ and thus $\Gamma_a = 0$. Equation (A.1) then leads to

$$\rho_s(L_a, t) = \rho_s(0, t) \left[1 + a I_p(t) + \frac{2}{3} a^2 I_p^2(t) \right] \quad (\text{A.2})$$

as given in Cheung and Liu [41].

In the DFM interaction the plane wave equations are given by Eqs. (3.18–3.21)

with $1 \rightarrow d$, $2 \rightarrow i$, and $3 \rightarrow s$. The solution for the signal wave in this interaction is

$$\rho_s(z, t) = \rho_s(L_a, t) \text{sn}(K_b - \sqrt{D_i} \kappa_b(z - z_2) | m_b) \quad (\text{A.3})$$

$$\rho_s(z, t) = \rho_s(L_a, t) \text{cd}(\sqrt{D_i} \kappa_b(z - z_2) | m_b) \quad (\text{A.4})$$

Once again we assume that we can expand the solution for the signal to obtain

$$\rho_s(L_b, t) = \rho_s(L_a, t) \left[1 - b D_i (1 - m_b) \right] \quad (\text{A.5})$$

$$\rho_s(L_b, t) = \rho_s(L_a, t) \left[1 - b \rho_i^2(L_a, t) \right]. \quad (\text{A.6})$$

Now we know the solution for $\rho_i^2(L_a, t)$ and can finally write

$$\rho_s(L_b, t) = \rho_s(L_a, t) \left[1 - b a I_1(t) I_p(t) \right] \quad (\text{A.7})$$

Multiplying Eqs. (A.2) and (A.7) we find

$$\rho_s(L_b, t) = \rho_s(L_a, t) \left[1 + a I_p(t) + \frac{2}{3} a^2 I_p^2(t) - b a I_1(t) I_p(t) - a^2 I_p^2(t) b I_1(t) \right] \quad (\text{A.8})$$

which leads directly to the gain equations (Eq. (4.11,4.12)) given in Section 4.2.2.

Now we are left with the equations for the various powers of the OPO-DFM device given by Eqs. (4.13–4.17). The signal power out of the OPO crystal is given by Eq. (A.2) modified with the transformation $\rho_s(L_a, t) \rightarrow I_{sOPO}(t)$ and $\rho_s(0, t) \rightarrow I_1(t)$. The transmitted pump and idler power out of the OPO crystal are determined by the Manley-Rowe constants C_s and C_i respectively. The idler power generated in the DFM interaction is calculated with application of the Manley-Rowe constant D_i where $I_{sOPO}(t)$ is the signal power into, and $I_1(t)$ is the signal power out of, the DFM crystal. Finally $I_d(t)$ is found with the help of the Manley-Rowe constant D_d .

References

- [1] D. Andreou, "16 μm tunable source using parametric processes in nonlinear crystals," *Opt. Commun.*, vol. 1, no. 23, pp. 37–43, 1977.
- [2] P. Kupecek, H. Le Person, and M. Comte, "A multipurpose efficient tunable infrared coherent source with tuning range from 0.8 to 25 μm and peak powers in the range 50–200 kW," *Infrared Phys.*, vol. 19, no. 3/4, pp. 263–271, 1979.
- [3] P. Kupecek, J. M. Weulersse, P. Isnard, M. Alexandre, and M. Clerc, "An optimized device for UF_6 laser isotopic photochemistry using an optical parametric oscillator and a down converter," *J. Opt. (Paris)*, , no. 14, pp. 43–48, 1983.
- [4] J. D. Kafka, M. L. Watts, and J. W. Pieterse, "Subpicosecond infrared pulse generation using a synchronously pumped optical parametric oscillator," in *Conference on Lasers and Electro-Optics, Vol. 8, OSA Technical Digest Series*, Washington, D.C., 1994, p. 237, Optical Society of America.
- [5] J. D. Kafka, M. L. Watts, and J. W. Pieterse, "Infrared pulse generation using a subpicosecond optical oscillator," in *Ultrafast Phenomena, Vol. 7, OSA Technical Digest Series*, Washington, D.C., 1994, pp. 258–260, Optical Society of America.
- [6] A. Lohner, P. Kruck, and W. W. Rühle, "Generation of 200 femtosecond pulses tunable between 2.5 and 5.5 μm ," *Appl. Phys. B*, vol. 59, no. 2, pp. 211–213, 1994.

- [7] K. Koch, G. T. Moore, and E. C. Cheung, "Optical parametric oscillation with intracavity difference-frequency mixing," *J. Opt. Soc. Am. B*, vol. 12, no. 11, pp. 2268–2273, 1995.
- [8] D. S. Moore and S. C. Schmidt, "Tunable subpicosecond infrared pulse generation to 4 μm ," *Opt. Lett.*, vol. 7, no. 12, pp. 480–482, 1987.
- [9] M. Woerner, W. Frey, M. T. Portella, C. Ludwig, T. Elsaesser, and W. Kaiser, "Ultrafast thermalization of nonequilibrium holes in p-type germanium studied by femtosecond infrared-spectroscopy," *Phys. Rev. B*, vol. 49, no. 24, pp. 17007–17010, 1994.
- [10] W. C. Eckhoff, R. S. Putnam, S. Wang, R. F. Curl, and F. K. Tittel, "A continuously tunable long-wavelength cw IR source for high-resolution spectroscopy and trace-gas detection," *Appl. Phys. B*, vol. 63, no. 5, pp. 437–441, 1996.
- [11] T. Töpfer, K. P. Petrov, Y. Mine, L. E. Myers, and R. W. Wallace, "Room-temperature midinfrared laser sensor for trace gas detection," *Appl. Opt.*, vol. 36, no. 30, pp. 8042–8049, 1997.
- [12] G. M. Gibson, M. H. Dunn, and M. J. Padgett, "Application of a continuously tunable, cw optical parametric oscillator for high-resolution spectroscopy," *Opt. Lett.*, vol. 23, no. 1, pp. 40–42, 1998.
- [13] S. E. Moody, "Environmental awareness raises hopes for lidar systems," *Laser Focus World*, vol. 27, no. 3, pp. 117–127, 1991.
- [14] W. C. Schwartz, "Solid-state lasers point to the future in military applications," *Laser Focus World*, vol. 27, no. 7, pp. 75–96, 1991.
- [15] S. P. Velsko and W. F. Krupke, "Applications of high-average power nonlinear optics," in *Proceedings of SPIE, Vol. 2700*, M. C. Gupta, W. J. Kozlovsky,

and D. C. MacPherson, Eds., Bellingham, WA, 1996, pp. 6–17, Optical Society of America.

- [16] W. R. Bosenberg, J. I. Alexander A. Drobshoff, L. E. Myers, and R. L. Byer, “93-percent pump depletion, 3.5-W continuous-wave, singly resonant optical parametric oscillator,” *Opt. Lett.*, vol. 21, no. 17, pp. 1336–1338, 1996.
- [17] M. Cavallari, G. M. Gale, F. Hache, L. I. Pavlov, and E. Rousseau, “Mid infra-red femtosecond pulse generation by wave-mixing: numerical simulation and experiment,” *Opt. Commun.*, vol. 114, no. 3,4, pp. 329–332, 1995.
- [18] F. Seifert, V. Petrov, and M. Woerner, “Solid-state laser system for the generation of midinfrared femtosecond pulses tunable from 3.3 to 10 μm ,” *Opt. Lett.*, vol. 19, no. 23, pp. 2009–2011, 1994.
- [19] D. C. Edelstein, E. S. Wachman, and C. L. Tang, “Broadly tunable high repetition rate femtosecond optical parametric oscillator,” *App. Phys. Lett.*, vol. 54, no. 18, pp. 1728–1730, 1989.
- [20] P. E. Powers, R. J. Ellingson, and W. S. Pelouch, “Recent advances of the Ti:sapphire-pumped high-repetition-rate femtosecond optical parametric oscillator,” *J. Opt. Soc. Am. B*, vol. 10, no. 11, pp. 2162–2167, 1993.
- [21] S. E. Harris, “Tunable optical parametric oscillators,” *Proceedings of the IEEE*, vol. 57, no. 12, pp. 2096–2113, 1969.
- [22] S. T. Yang R. C. Eckardt and R. L. Byer, “Power and spectral characteristics of continuous-wave parametric oscillators: the doubly to singly resonant transition,” *J. of Opt. Soc. Am. B*, vol. 10, no. 9, pp. 1684–1695, 1993.
- [23] J. A. Giordmaine and R. C. Miller, “Tunable coherent parametric oscillation in LiNbO_3 at optical frequencies,” *Phys. Rev. Lett.*, vol. 14, no. 24, pp. 973–976, 1965.

- [24] R. Zernike and J. E. Midwinter, *Applied Nonlinear Optics*, John Wiley & Sons, New York, 1973.
- [25] C. Ludwig, W. Frey, M. Woerner, and T. Elsaesser, "Generation of synchronized femtosecond pulses independently tunable in the midinfrared," *Opt. Commun.*, vol. 102, no. 5,6, pp. 447–451, 1993.
- [26] S. D. Butterworth, V. Pruneri, and D. C. Hanna, "Optical parametric oscillation in periodically poled lithium niobate on continuous-wave synchronous pumping at 1.047 μm ," *Optics Lett.*, vol. 21, no. 17, pp. 1345–1347, 1996.
- [27] E. C. Cheung, K. Koch, and G. T. Moore, "Silver thiogallate, singly resonant optical parametric oscillator pumped by a continuous-wave mode-locked Nd:YAG laser," *Optics Lett.*, vol. 19, no. 23, pp. 1967–1969, 1994.
- [28] R. L. Byer, "Quasi-phasematched nonlinear interactions and devices," *J. of Nonlinear Optical Phys. and Materials*, vol. 6, no. 4, pp. 549–592, 1997.
- [29] L. E. Myers, R. C. Eckardt, M. M. Fejer, R. L. Byer, W. R. Bosenberg, and J. W. Pierce, "Quasi-phase-matched optical parametric oscillators in bulk periodically poled LiNbO_3 ," *J. Opt. Soc. Am. B*, vol. 12, no. 11, pp. 2102–2116, 1995.
- [30] V. Pruneri, J. Webjörn, P. St. J. Russell, and D. C. Hanna, "532 nm pumped optical parametric oscillator in bulk periodically poled lithium niobate," *App. Phys. Lett.*, vol. 67, no. 15, pp. 2126–2128, 1995.
- [31] D. J. Lovering, J. A. Levenson, P. Vidakovic, J. Webjörn, and P. St. J. Russell, "Noisless optical amplification in quasi-phase-matched bulk lithium niobate," *Opt. Lett.*, vol. 21, no. 18, pp. 1439–1441, 1995.
- [32] M. A. Arbore and M. M. Fejer, "Frequency doubling of femtosecond erbium-fiber soliton lasers in periodically poled lithium niobate," *Opt. Lett.*, vol. 22, no. 1, pp. 13–15, 1997.

- [33] J. A. Armstrong, N. Bloembergen, J. Ducuing, and P. S. Pershan, "Interactions between light waves in a nonlinear dielectric," *Phys. Rev.*, vol. 127, no. 6, pp. 1918–1939, 1962.
- [34] R. G. Smith, "Theory of intracavity optical second-harmonic generation," *IEEE J. of Quantum Electron.*, vol. QE-6, no. 4, pp. 215–223, 1970.
- [35] A. J. Campillo and C. L. Tang, "Extending the tuning range of tunable oscillators by upconversion," *App. Phys. Lett.*, vol. 19, no. 2, pp. 36–38, 1971.
- [36] A. J. Campillo, "Internal upconversion and doubling of an optical parametric oscillator to extent the tuning range," *IEEE J. of Quantum Electron.*, vol. 8, no. 12, pp. 914–916, 1972.
- [37] P. P. Bey and C. L. Tang, "Plane-wave theory of parametric oscillator and coupled oscillator-upconverter," *IEEE J. of Quantum Electron.*, vol. QE-8, no. 3, pp. 361–369, 1972.
- [38] R. J. Ellingson and C. L. Tang, "High-power, high-repetition-rate femtosecond pulses tunable in the visible," *Opt. Lett.*, vol. 18, no. 6, pp. 438–440, 1993.
- [39] G. T. Moore and K. Koch, "Optical parametric oscillation with intracavity sum-frequency generation," *IEEE J. of Quantum Electron.*, vol. 29, no. 3, pp. 961–969, 1993.
- [40] G. T. Moore and K. Koch, "Optical parametric oscillation with detuned intracavity sum-frequency generation," *IEEE J. of Quantum Electron.*, vol. 29, no. 8, pp. 2334–2341, 1993.
- [41] E. C. Cheung and J. M. Liu, "Theory of a synchronously pumped optical parametric oscillator in steady-state operation," *J. Opt. Soc. Am.*, vol. 7, no. 8, pp. 1385–1401, 1990.

- [42] E. C. Cheung and J. M. Liu, "Efficient generation of ultrashort, wavelength-tunable infrared pulses," *J. Opt. Soc. Am.*, vol. 8, no. 7, pp. 1491–1506, 1991.
- [43] E. C. Cheung, K. Koch, and G. T. Moore, "Frequency upconversion by phase-matched sum-frequency generation in an optical parametric oscillator," *Opt. Lett.*, vol. 19, no. 23, pp. 1967–1969, 1994.
- [44] G. T. Moore, K. Koch, and E. C. Cheung, "Optical parametric oscillation with intracavity second-harmonic generation," *Opt. Comm.*, vol. 113, no. 4,5,6, pp. 463–470, 1994.
- [45] M. E. Dearborn, K. Koch, G. T. Moore, and J. C. Diels, "Greater than 100% photon conversion efficiency in an optical parametric oscillator with intracavity difference frequency mixing," *Opt. Lett.*, vol. 10, no. 23, pp. 759–776, 1998.
- [46] J. E. Midwinter and J. Warner, "The effects of phase matching method and of uniaxial crystal symmetry on the polar distribution of second-order non-linear optical polarization," *Brit. J. of Appl. Phys.*, vol. 16, no. 8, pp. 1135–1142, 1964.
- [47] D. Eimerl, L. Davis, and S. Velsko, "Optical, mechanical, and thermal properties of barium grown lithium niobate," *J. Appl. Phys.*, vol. 62, no. 5, pp. 1968–1983, 1987.
- [48] J. P. Fève, B. Boulanger, and G. Marnier, "Calculation and classification of the direction loci for collinear types I, II and III phase-matching of three-wave non-linear optical parametric interactions in uniaxial and biaxial acentric crystals," *Opt. Commun.*, vol. 99, no. 3,4, pp. 284–302, 1993.
- [49] A. Harada, Y. Nihei, Y. Okazaki, and Y. Hyuga, "Intracavity frequency-doubling of a diode-pumped 946-nm Nd-YAG laser with bulk periodically poled MgO-LiNbO₃," *Opt. Lett.*, vol. 22, no. 11, pp. 805–807, 1997.

- [50] D. H. Jundt, G. A. Magel, M. M. Fejer, and R. L. Byer, "Periodically poled LiNbO₃ for high-efficiency second-harmonic generation," *Opt. Lett.*, vol. 22, no. 20, pp. 1553–1555, 1997.
- [51] K. Mizuuchi and K. Yamamoto, "Generation of 340-nm light by frequency-doubling of a laser-diode in bulk periodically poled LiTaO₃," *Opt. Lett.*, vol. 21, no. 2, pp. 107–109, 1996.
- [52] M. Oron, M. Katz, D. Eger, G. Rosenman, and A. Skliar, "Highly efficient blue-light generation in flux-grown KTiOPO₄ periodically poled by an electric-field," *Electron. Lett.*, vol. 33, no. 9, pp. 807–809, 1997.
- [53] M. A. Mortazavi and G. Khanarian, "Quasi-phase-matched frequency doubling in bulk periodic polymeric structures," *Opt. Lett.*, vol. 19, no. 17, pp. 1290–1292, 1994.
- [54] M. Jäger, G. I. Stegeman, W. Brinker, S. Yilmaz, S. Bauer, W. H. G. Horsthuis, and G. R. Möhlmann, "Comparison of quasi-phase-matching geometries for second-harmonic generation in poled polymer channel waveguides at 1.5 μm ," *Appl. Phys. Lett.*, vol. 68, no. 9, pp. 1183–1185, 1996.
- [55] Y. Shuto, T. Watanabe, S. Tomaru, I. Yokohama, M. Hikita, and M. Amano, "Quasi-phase-matched second-harmonic generation in diazo-dye-substituted polymer channel waveguides," *IEEE J. of Quant. Electron.*, vol. 33, no. 3, pp. 349–357, 1997.
- [56] A. Szilagyi, A. Hordvik, and H. Schlossberg, "A quasi-phase-matching technique for efficient optical mixing and frequency doubling," *J. Appl. Phys.*, vol. 47, no. 5, pp. 2025–2032, 1976.
- [57] M. Okada, K. Takizawa, and S. Ieiri, "Second harmonic generation by periodic laminar structure of a nonlinear optical crystal," *Opt. Commun.*, vol. 18, no. 3, pp. 331–334, 1976.

- [58] G. A. Magel, M. M. Fejer, and R. L. Byer, "Quasi-phase-matched second-harmonic generation of blue light in periodically poled LiNbO_3 ," *Appl. Phys. Lett.*, vol. 56, no. 2, pp. 108–110, 1990.
- [59] S. Miyazawa, "Ferroelectric domain inversion in Ti-diffused LiNbO_3 optical waveguide," *J. Appl. Phys.*, vol. 50, no. 7, pp. 4599–4603, 1979.
- [60] L. Ya-lin, L. Mao, and N. Ming, "Blue-light generation by frequency doubling of an 810-nm cw GaAlAs diode laser in a quasi-phase-matched LiNbO_3 crystal," *Opt. Lett.*, vol. 19, no. 14, pp. 1037–1039, 1994.
- [61] S. Somekh and A. Yariv, "Phase-matchable nonlinear optical interactions in periodic thin films," *Appl. Phys. Lett.*, vol. 21, no. 4, pp. 140–141, 1972.
- [62] J. D. Bierlein, D. B. Laubacher, J. B. Brown, and C. J. van der Poel, "Balanced phase matching in segmented KTiOPO_4 wave-guides," *App. Phys. Lett.*, vol. 56, no. 18, pp. 1725–1727, 1990.
- [63] T. P. Grayson, L. E. Myers, M. D. Nelson, and V. Dominic, "Synchronous pumping of a periodically poled LiNbO_3 optical parametric oscillator," *OSA TOPS on ASSL*, vol. 1, pp. 46–50, 1996.
- [64] L. Goldberg, W. K. Burns, and R. W. McElhanon, "Difference-frequency-generation of tunable midinfrared radiation in buld periodically poled LiNbO_3 ," *Opt. Lett.*, vol. 20, no. 11, pp. 1280–1282, 1995.
- [65] D. H. Jundt, "Temperature-dependent Sellmeier equation for the index of refraction, $n(e)$, in congruent lithium-niobate," *Opt. Lett.*, vol. 22, no. 20, pp. 1553–1555, 1997.
- [66] G. T. Moore and K. Koch, "The tandem optical parametric oscillator," *IEEE J. of Quantum Electron.*, vol. 32, no. 12, pp. 2085–2094, 1996.

- [67] Y. S. Kim and R. T. Smith, "Thermal expansion of lithium tantalate and lithium niobate single crystals," *J. Appl. Phys.*, vol. 40, no. 11, pp. 4637–4641, 1969.
- [68] G. D. Miller, R. G. Batchko, M. M. Fejer, and R. L. Byer, "Visible quasi-phases-matched harmonic generation by electric-field-poled lithium niobate," in *Proceeding of SPIE*, Washington D. C., 1996, pp. 34–45, Optical Society of America.
- [69] F. S. Chen, "Optically induced change of refractive indices in LiNbO_3 and LiTaO_3 ," *J. App. Phys.*, vol. 40, no. 8, pp. 3389–3396, 1969.
- [70] D. Redfield and W. J. Burke, "Optical absorption edge of LiNbO_3 ," *J. of App. Phys.*, vol. 45, no. 10, pp. 4566–4571, 1974.
- [71] V. Pruneri, P. G. Kazansky, J. Webjörn, P. St. J. Russell, and D. C. Hanna, "Self-organized light-induced scattering in periodically poled lithium niobate," *App. Phys. Lett.*, vol. 67, no. 14, pp. 1957–1959, 1995.
- [72] B. Sturman, María Aguilar, R. Agulló-López, V. Pruneri, P. G. Kazansky, and D. C. Hanna, "Mechanism of self-organized light-induced scattering in periodically poled lithium niobate," *App. Phys. Lett.*, vol. 69, no. 10, pp. 1349–1351, 1996.
- [73] G. Zhong, J. Jian, and Z. Wu, "Measurements of optically induced refractive-index damage of lithium niobate doped with different concentrations of MgO ," in *11th International Quantum Electronics Conference, IEEE Cat. No. 80*, Bellingham, WA, 1980, p. 631, Optical Society of America.
- [74] M. M. Fejer, G. A. Magel, D. H. Jundt, and R. L. Byer, "Quasi-phase-matched second harmonic generation: Tuning and tolerances," *IEEE J. of Quantum Electronics*, vol. 28, no. 11, pp. 2631–2654, 1992.

- [75] S. J. Brosnan and R. L. Byer, "Optical parametric oscillator threshold and linewidth studies," *IEEE J. of Quantum Electron.*, vol. QE-15, no. 6, pp. 415–431, 1979.
- [76] J. M. Thomas and J. P. Taran, "Pulse distortions in mismatched second harmonic generation," *Opt. Commun.*, vol. 4, no. 5, pp. 329–334, 1972.
- [77] R. DeSalvo, D. J. Hagan, M. Sheik-Hahae, G. Stegeman, and E. W. Van Stryland, "Self-focusing and self-defocusing by cascaded second-order effects in KTP," *Opt. Lett.*, vol. 17, no. 1, pp. 28–30, 1992.
- [78] P. Vidaković, D. J. Lovering, J. A. Levenson, J. Webjörn, and P. St. J. Russell, "Large nonlinear phase shift owing to cascaded $\chi^{(2)}$ in quasi-phase-matched bulk LiNbO₃," *Opt. Lett.*, vol. 22, no. 5, pp. 277–279, 1997.
- [79] H. Li, F. Zhou, X. Zhang, and W. Ji, "Bound electronic Kerr effect and self-focusing induced damage in second-harmonic-generation crystals," *Opt. Commun.*, vol. 144, no. 1,2,3, pp. 75–81, 1997.
- [80] D. A. Bryan, R. Gerson, and H. E. Tomaschke, "Increased optical damage resistance in lithium niobate," *Appl. Phys. Lett.*, vol. 44, no. 9, pp. 847–849, 1984.
- [81] R. W. Boyd, *Nonlinear Optics*, Academic Press, San Diego, 1991.
- [82] A. M. Glass, D. von der Linde, and T. J. Negran, "High-voltage bulk photovoltaic effect and the photorefractive process in LiNbO₃," *Appl. Phys. Lett.*, vol. 25, no. 4, pp. 233–235, 1975.
- [83] M. Taya, M. C. Bashaw, and M. M. Fejer, "Photorefractive effects in periodically poled ferroelectrics," *Opt. Lett.*, vol. 21, no. 12, pp. 857–859, 1996.

- [84] N. V. Kukhtarev, V. B. Markov, S. G. Odulov, M. S. Soskin, and V. L. Vinetskii, "Holographic storage in electrooptic crystals. I. steady state," *Ferroelectrics*, vol. 22, no. 3/4, pp. 949–960, 1979.
- [85] D. T. Reid, Z. Penman, M. Ebrahimzadeh, W. Sibbett, H. Karlsson, and F. Laurell, "Broadly tunable infrared femtosecond optical parametric oscillator based on periodically poled RbTiOAsO₄," *Opt. Lett.*, vol. 22, no. 18, pp. 1397–1399, 1997.
- [86] D. Zheng, L. A. Gordon, Y. S. Wu, R. K. Route, R. S. Feigelson, M. M. Fejer, R. L. Byer, M. S. Bowers, A. Drobshoff, and D. Smith, "12-micron infrared generation by difference frequency mixing in diffusion bonded stacked GaAs," in *Advanced Solid-State Lasers Technical Digest*, Washington, D.C., 1998, pp. 108–110, Optical Society of America.
- [87] R. L. Sutherland, *Handbook of Nonlinear Optics, Optical Engineering Series, Vol. 52*, Marcel Dekker, New York, 1996.
- [88] V. G. Dmitriev, G. G. Gurzadyan, and D. N. Nikogosyan, *Handbook of Nonlinear Optical Crystals*, Springer-Verlag, 1997.
- [89] D. A. Kleinman, "Nonlinear dielectric polarization in optical media," *Phys. Rev.*, vol. 126, no. 6, pp. 1977–1979, 1962.
- [90] J. C. Diels and W. Rudolph, *Ultrashort Laser Pulse Phenomena*, Academic Press, San Diego, 1997.
- [91] R. A. Baumgartner and R. L. Byer, "Optical parametric amplification," *IEEE J. of Quantum Electron.*, vol. 15, no. 6, pp. 432–444, 1979.
- [92] M. Abramowitz and I. A. Stegun, *Handbook of Mathematical Functions*, pp. 567–585, Dover Press, New York, 1965.

- [93] W. H. Louisell, A. Yariv, and A. E. Siegman, "Quantum fluctuations and noise in parametric processes. I.," *Phys. Rev.*, vol. 124, no. 6, pp. 1646–1654, 1961.
- [94] H. A. Haus, "Theory of mode locking with a fast saturable absorber," *J. Appl. Phys.*, vol. 46, no. 7, pp. 3049–3058, 1975.
- [95] H. A. Haus, "Theory of mode locking with a slow saturable absorber," *IEEE J. of Quantum Electron.*, vol. QE-11, no. 9, pp. 736–747, 1975.
- [96] H. A. Haus, "A theory of forced mode locking," *IEEE J. of Quantum Electron.*, vol. QE-11, no. 7, pp. 323–330, 1975.
- [97] J. Falk, "Instabilities in the doubly resonant parametric oscillator: a theoretical analysis," *IEEE J. of Quantum Electron.*, vol. QE-7, no. 6, pp. 230–235, 1971.
- [98] J. E. Bjorkholm, "Efficient optical parametric oscillation using doubly and singly resonant cavities," *App. Phys. Lett.*, vol. 13, no. 2, pp. 53–56, 1968.
- [99] G. D. Boyd, A. Ashkin, J. M. Dziedzic, and D. A. Kleinman, "Second-harmonic generation of light with double refraction," *Phys. Rev.*, vol. 137, no. 4a, pp. A1305–A1320, 1965.
- [100] D. A. Kleinman, A. Ashkin, and G. D. Boyd, "Second harmonic generation of light by focused laser beams," *Phys. Rev.*, vol. 145, no. 1, pp. 338–379, 1966.
- [101] G. D. Boyd and A. Ashkin, "Theory of parametric oscillator threshold with single-mode optical masers and observation of amplification in LiNbO_3 ," *Phys. Rev.*, vol. 146, no. 1, pp. 187–198, 1966.
- [102] G. D. Boyd and D. A. Kleinman, "Parametric interaction of focused gaussian light beams," *J. of App. Phys.*, vol. 39, no. 8, pp. 3597–3639, 1968.
- [103] S. Guha, F. Wu, and J. Falk, "The effects of focusing on parametric oscillation," *IEEE J. of Quant. Electron.*, vol. QE-18, no. 5, pp. 907–912, 1935.

- [104] E. L. Kerr, "Filamentary tracks formed in transparent optical glass by laser beam self-focusing. II, theoretical analysis," *Phys. Rev. A*, vol. 4, no. 3, pp. 1195-1218, 1971.
- [105] B. R. Suydam, "Self focusing of very powerful laser beams," in *Laser induced damage in optical materials: 1973*, A. J. Glass and A. H. uenther, Eds., Washington, D. C., 1973, pp. 42-48, National Bureau of Standards Special Publication 387.
- [106] B. R. Suydam, "Self-focusing of very powerful laser beams, II," *IEEE J. of Quantum Electron.*, vol. QE-10, no. 11, pp. 837-843, 1974.
- [107] F. A. Hopf, P. Meystre, M. O. Scully, and J. F. Seely, "Coherence brightening and laser lethargy in X-ray laser amplifiers," *Phys. Rev. Lett.*, vol. 35, no. 8, pp. 511-513, 1975.
- [108] F. A. Hopf and P. Meystre, "Quantum theory of a swept-gain laser amplifier," *Phys. Rev. A*, vol. 12, no. 6, pp. 2534-2548, 1975.
- [109] F. A. Hopf, P. Meystre, and D. W. McLaughlin, "Quantum theory of a swept-gain amplifier. II," *Phys. Rev. A*, vol. 13, no. 2, pp. 777-783, 1976.
- [110] G. T. Moore and M. O. Scully, "Pulse propagation and laser lethargy in the free-electron laser," in *Free Electron Lasers*, S. Martellucci and A. N. Chester, Eds., New York, 1983, pp. 175-187, Plenum Pub. Corp.
- [111] G. J. Edwards and M. Lawrence, "A temperature-dependent despersion equation for congruently grown lithium niobate," *Opt. Quantum Electron.*, vol. 16, no. 4, pp. 373-375, 1984.
- [112] R. C. Miller, "Optical second harmonic generation in piezoelectric crystals," *Appl. Phys. Lett.*, vol. 5, no. 1, pp. 17-19, 1964.

- [113] C. G. B. Garrett and F. N. H. Miller, "Miller's phenomenological rule for computing nonlinear susceptibilities," *IEEE J. of Quantum Electronics*, vol. QE-2, no. 8, pp. 328-329, 1966.
- [114] G. M. Zverev, E. A. Levchuk, V. A. Pashkov, and Yu. P. Poryadin, "Laser-radiation-induced damage to the surface of lithium niobate and tantalate," *Sov. J. of Quantum Electron.*, vol. 2, no. 8, pp. 167-169, 1972.
- [115] G. M. Zverev, E. A. Levchuk, V. A. Pashkov, and Yu. P. Poryadin, "Damage to the surface of lithium niobate by light," *Sov. Phys. JETP*, vol. 35, no. 1, pp. 165-167, 1972.
- [116] G. M. Zverev, S. A. Kolyadin, E. A. Levchuk, and L. A. Skvortsov, "Influence of the surface layer on the optical strength of lithium niobate," *Sov. J. of Quantum Electron.*, vol. 7, no. 9, pp. 1071-1075, 1977.
- [117] W. R. Bosenberg, A. Drobshoff, D. C. Gerstemberger, L. E. Myers, R. C. Eckardt, M. M. Fejer, and R. L. Byer, "Long pulse optical parametric oscillator based on periodically-poled LiNbO₃," in *Proc. on CLEO*, Washington, D.C., 1996, pp. 42-44, Optical Society of America.
- [118] Missey and L. Myers, "Diffusion-bonded stacks of periodically poled lithium-niobate," *Opt. Lett.*, vol. 23, no. 9, pp. 664-666, 1998.
- [119] W. R. Bosenberg, J. I. Alexander, L. E. Myers, and R. W. Wallace, "2.5 W continuous-wave, solid-state laser source at 629 nm," *Opt. Lett.*, vol. 23, no. 3, pp. 20-22, 1998.
- [120] P. T. Nee and N. C. Wong, "Optical frequency division by 3 of 532 nm in periodically poled lithium niobate with a double grating," *Opt. Lett.*, vol. 23, no. 1, pp. 46-48, 1998.

- [121] W. R. Bosenberg, A. Drobshoff, D. C. Gerstemberger, L. E. Myers, R. C. Eckardt, M. M. Fejer, and R. L. Byer, "Long pulse optical parametric oscillator based on periodically-poled LiNbO₃," in *Proc. on CLEO*, Washington, D.C., 1995, pp. 42–44, Optical Society of America.
- [122] P. E. Powers, T. J. Kulp, and S. E. Bisson, "Continuous tuning of a continuous-wave periodically poled parametric oscillator by use of a fan-out grating design," *Opt. Lett.*, vol. 23, no. 3, pp. 159–161, 1998.
- [123] K. C. Burr, C. L. Tang, M. A. Arbore, and M. M. Fejer, "Broadly tunable mid-infrared femtosecond optical parametric oscillator using all-solid-state-pumped periodically poled lithium niobate," *Opt. Lett.*, vol. 22, no. 19, pp. 1458–1460, 1997.
- [124] C. McGowan, D. T. Reid, Z. E. Penman, M. Ebrahimzadeh, W. Sibbett, and D. H. Jundt, "Femtosecond optical parametric oscillator based on periodically poled lithium-niobate," *J. of the Optical Soc. of Amer. B*, vol. 15, no. 2, pp. 694–701, 1998.
- [125] M. A. Arbore, A. Galvanauskas, D. Harter, M. H. Chou, and M. M. Fejer, "Engineerable compression of ultrashort pulses by use of 2nd-harmonic generation in chirped-period-poled lithium-niobate," *Opt. Lett.*, vol. 22, no. 7, pp. 1341–1343, 1997.
- [126] O. Pfister, J. S. Wells, L. Hollberg, L. Zink, D. A. Van Baak, M. D. Levenson, and W. R. Bosenberg, "Continuous-wave frequency tripling and quadrupling by simultaneous three-wave mixings in periodically poled crystals: application to a two-step 1.19–10.71- μ m frequency bridge," *Opt. Lett.*, vol. 22, no. 16, pp. 1211–1213, 1997.
- [127] D. Taverner, P. Britton, P. G. R. Smith, D. J. Richardson, G. W. Ross, and D. C. Hanna, "Highly efficient second-harmonic and sum-frequency generation of

nanosecond pulses in a cascaded erbium-doped fiber: periodically poled lithium niobate source," *Opt. Lett.*, vol. 23, no. 3, pp. 162–164, 1998.

- [128] M. Asobe, I. Yokohama, H. Itoh, and T. Kaino, "All-optical switching by use of cascading of phase-matched sum-frequency-generation and difference-frequency-generation processes in periodically poled LiNbO₃," *Opt. Lett.*, vol. 22, no. 5, pp. 274–276, 1997.